Search for Very High Energy Gamma-ray from Galactic Sources & Development of Calibration System for future imaging telescope

By

Anshu Chatterjee

PHYS05201204010

Saha Institute of Nuclear Physics

Kolkata

A thesis submitted to the

Board of Studies in Physical Sciences

In partial fulfillment of requirements

For the Degree of

DOCTOR OF PHILOSOPHY

of

HOMI BHABHA NATIONAL INSTITUTE

July, 2019

Homi Bhabha National Institute

Recommendations of the Viva Voce Board

As members of the Viva Voce Board, we certify that we have read the dissertation prepared by **ANSHU CHATTERJEE** entitled **Search for Very High Energy Gamma-ray from Galactic Sources & Development of Calibration System for future imaging telescope** and recommend that it maybe accepted as fulfilling the dissertation requirement for the Degree of Doctor of Philosophy.

Debades Bandyopadhyay 24.10.2019

Chair - Prof. Debades Bandyopadhyay

Pratik Majumdar 24/10/19

Guide/Convener - Prof. Pratik Majumdar

Nayantara Gupta 24/10/19

Examiner - Prof. Nayantara Gupta

P Bhattacharjee 24/10/2019

Member 1 - Prof. Pijushpani Bhattacharjee

S Saha 24/10/2019

Member 2 - Prof. Satyajit Saha

Final approval and acceptance of this thesis is contingent upon the candidate's submission of the final copies of the thesis to HBNI.

I hereby certify that I have read this thesis prepared under my direction and recommend that it may be accepted as fulfilling the thesis requirement.

Date: 24/10/19

Place: KOLKATA

Guide: Pratik Majumdar

Prof. Pratik Majumdar

STATEMENT BY AUTHOR

This dissertation has been submitted in partial fulfillment of requirements for an advanced degree at Homi Bhabha National Institute (HBNI) and is deposited in the Library to be made available to borrowers under rules of the HBNI.

Brief quotations from this dissertation are allowable without special permission, provided that accurate acknowledgement of source is made. Requests for permission for extended quotation from or reproduction of this manuscript in whole or in part may be granted by the Competent Authority of HBNI when in his or her judgment the proposed use of the material is in the interests of scholarship. In all other instances, however, permission must be obtained from the author.

Anshu Chatterjee

Anshu Chatterjee

DECLARATION

I, hereby declare that the investigation presented in the thesis has been carried out by me. The work is original and has not been submitted earlier as a whole or in part for a degree / diploma at this or any other Institution / University.

Anshu Chatterjee

Anshu Chatterjee

List of Publications arising from the thesis

Journal

1. "RECOMBINING PLASMA IN THE GAMMA-RAY-EMITTING MIXED MORPHOLOGY SUPERNOVA REMNANT 3C 391",

   T. Ergin, A. Sezer, L. Saha, P. Majumdar, **A. Chatterjee**, A. Bayirli, E. N. Ercan

   The Astrophysical Journal, **2014**, vol. **790**, 065-074, [arXiv:1406.2179v1 [astro-ph.HE].

2. "MAGIC and *Fermi*-LAT gamma-ray results on unassociated HAWC sources",

   M. L. Ahnen, S. Ansoldi, L. A. Antonelli, C. Arcaro, D. Baack, A. Babić, B. Banerjee, P. Bangale, U. Barres de Almeida, J. A. Barrio, J. Becerra González, W. Bednarek, E. Bernardini, R. Ch. Berse, A. Berti, W. Bhattacharyya, A. Biland, O. Blanch, G. Bonnoli, R. Carosi, A. Carosi, G. Ceribella,**A. Chatterjee**, et. al. (MAGIC collaboration)

   Monthly Notices of the Royal Astronomical Society, **2019**, vol. **485**, 356-366, [arXiv:1901.03982 [astro-ph.HE].

Conferences

1. "Time Dependent Model of Young Pulsar Wind Nebulae",

   A. Chatterjee, L. Saha, P. Majumdar,

   ASI Conference Series, 2015, Vol. **12**, pp 145-146

   `http://astron-soc.in/bulletin/asics_vol012`.

2. "Design of a prototype device to calibrate the Large Size Telescope camera of the Cherenkov Telescope Array",

   M. Iori, P. Majumdar, F. De Persio, **A. Chatterjee**, F. Ferrarotto, B. K. Nagesh, L. Saha, B. B. Singh,

   Proceedings of Science, (ICRC2015) 954

   [arXiv:1508.06752 [astro-ph.IM].

3. "MAGIC observations on Pulsar Wind Nebulae around high spin-down power *Fermi*-LAT pulsars",
   A. Fernández-Barral, O. Blanch, **A. Chatterjee**, E. de Oña Wilhelmi, D. Fidalgo, for the MAGIC Collaboration,
   Proceedings of Science, (ICRC2017) 733
   [arXiv:1709.01754 [astro-ph.HE].

4. "Test results of a prototype device to calibrate the Large Size Telescope camera proposed for the Cherenkov Telescope Array",
   M. Palatiello, D. Cauz, F. De Persio, F. Ferrarotto, G. Paoletta, M. Iori, P. Majumdar, **A. Chatterjee**, V. Chitnis, B. B. Singh, K. Gothe, M. Manoranjan,
   Proceedings of Science, (ICRC2017) 857
   [arXiv:1708.09289 [astro-ph.IM].

Anshu Chatterjee.

Anshu Chatterjee

DEDICATIONS

Dedicated to my Parents.

ACKNOWLEDGEMENTS

First of all, I would like to express my deep gratitude to my supervisor Prof. Pratik Majumdar who has introduced me to the field of Observational Gamma-ray Astronomy and guided me throughout the whole PhD tenure in academic as well as non-academic purpose. I am grateful to my senior and collaborator Lab Saha who always has tried to give me a hand whenever needed. Special acknowledgement goes to Prof. Varsha R. Chitnis who has helped me academically as well as non-academically during my TIFR visit. I am also grateful to my other collaborators: Alba Fernńdez Barral, David Carreto Fidalgo, B. B. Singh, B. K. Nagesh, Manoranjan shahil, Kiran Gothe and Tulun Ergin.

Special acknowledgement goes to our divisional head Prof. Debadesh Bhattacharyya and HBNI academic dean (physical sciences) Prof. Prakash Mathews for non-academic supports during my stay in SINP.

I want to specially thank Biswajit Banerjee who as a junior and amazing lab mate was always willing to help and give his best suggestions. The academic and non academic discussion with him helps me a lot through out the PhD tenure. I also want to thank Naosad Alam and Satyajit Chowdhury. Their supports and countless helps was the strong backup for me in every difficult situation. The precious time spend with all of them was a memorable part of my PhD tenure.

The time at SINP could not be more lively and lovely without my dear colleagues and thanks to them : Biswajit Banerjee, Prasanta Char, Khamakhya Prasad Modak, Susnata Seth, Anirban Biswas, Amit Dutta Banik, Arindam Majumdar, Chowdhury Aminul Islam, Anisur Rahaman, Abhijit Ghosh, Sourav dey, Rome Samanta, Mainak Chakraborty, Roopam Sinha, Madhurima Pandey, Sajad Ahmad Bhat, Avik Paul, Sunita Sahoo, Upala Mukhopadhyay, Satyabrata Datta and Suroj.

It is my pleasure to thank my Post M.Sc. batch mates at SINP, Aritra, Ashim, Achyut, Amrita, Arpan, Chiranjib, Tapas, Naosad, Sabuj, Sukanto, Gouranga, Kuntal(Nayek), Kuntal (Mondal), Tirthankar, Sanjukta, Binita, Sanjib, Pankaj, Debajyoti, Suvankar, Kamalendu, Mily, Sourav, Tapas (Paul), Kumar, Sudip, Hena, Chitralekhha, Barnamala.

The financial supports from DAE are gratefully acknowledged.

Last but not least, I am indebted to the countless supports and encouragement from my parents and family over the long journey of PhD and special thank to Koyel Ghosh who has always been by my side for last one year and encouraging me. At the end, I want to express deepest gratitude to my departed father, who has always encouraged me for pursue my dream of higher studies.

Contents

Synopsis

In recent years substantial experimental and theoretical efforts have been done to investigate the physics issues involved in most energetic phenomenas of our galaxy and beyond it. These events emit significant fraction of their energy in the form of non-thermal electromagnetic radiation. The branch of astronomy which involves the observation and analysis of these energetic gamma photons is known as High Energy Gamma-ray astronomy. The main goal behind the study of the high energy events is to explore the fundamental physical processes responsible for the acceleration of particles upto the knee of cosmic ray energy spectrum ($\sim 10^{15}$ eV).

The theoretical development and observations both have an equal importance in the progress of High Energy Gamma-ray astronomy. The incoming photon flux and interaction probability with ambient medium depend on primary photon energy. No one detection method is sufficient to cover the whole energy range of High Energy Gamma-ray astronomy. Based on detection efficiency, different techniques are used for different energy ranges. The direct detection method is most efficient for low energy gamma photons (from tens of MeV to hundreds of GeV). This method involves on board satellite based detection technique. Fermi Large Area Telescope (Fermi-LAT) [1, 2] is the most important detector which covers an energy range from $20 MeV$ to $300 GeV$. An anti-coincidence circuit and shield are used to identify cosmic charge particles. The gamma photons undergoes pair production and the trajectory of electron-positron pairs are reconstructed by the tracker. Finally

LAT measures the energy of subsequent electromagnetic shower that develops in telescope's calorimeter. The large field of view (2.4 sr) allows LAT to scan the whole sky in every 3 hours. For very high energy gamma photons ($>$ 100 GeV), indirect detection methods are more efficient than direct method. The interaction of gamma photons with earth's atmosphere produces cascades of subatomic particles, known as Extensive Air Showers (EAS). When pass through air medium, these ultra relativistic particles emit Cherenkov radiation and produce a uniform light pool of $250m$ diameter on sea level. These Cherenkov photons at ground are collected by large reflectors and form image of the cascades with high speed camera. This indirect method of imaging EAS is known as Imaging Atmospheric Cherenkov (IAC) technique. The IACT camera is made of high speed photomultiplier tubes (PMT) which convert photons into amplified electrical signal and then transmitted via independent optical fibers. The camera trigger mechanism allow to record events only with certain minimum threshold amplitude. Major Atmospheric Gamma Imaging Cherenkove (MAGIC) telescope [3, 4] is a stereoscopic system of two 17 m diameter Imaging Atmospheric Cherenkove Telescopes (IACT) situated in the Canary Island of La Palma, Spain. The present MAGIC telescope system achieves an integral sensitivity of $0.66 \pm 0.03\%$ of the Crab Nebula flux in $50hrs$ of observation above $220GeV$ [5]. Other indirect methods are also used to detect ultra-high energy gamma photons. The High Altitude Water Cherenkov (HAWC) Observatory [6, 7] is second generation of ground-based gamma-ray extensive air shower array, located in Sierra Negra, Mexico and successor to the Milagro gamma-ray Observatory [8]. HAWC is sensitive to gamma rays in the energy range of $100GeV - 100TeV$. HAWC observatory consists of 300 water Cherenkov detectors (WCDs) over an area of 22000m^2. Each WCD is 7.3m in diameter, 4.5m in depth, and filled with $\sim 200,000$ L of purified water. Four upward-facing photomultiplier tubes (PMTs) are attached to the bottom of each WCD to detect the Cherenkov radiation produced by the secondary particles in an air shower. HAWC operates with $> 95\%$ duty cycle with a large field of view (FoV) of 15% of the sky, which allows it to scan two-thirds of sky every 24 hours.

The main source of galactic high energy events are Supernova explosion and Nebula related to high spin down pulsar (known as Pulsar Wind nebula). The Pulsar Wind Nebulae (PWNe) with Supernova remnants (SNRs) represent the most numerous population of TeV sources in our galaxy [9,10] and are widely believed to be responsible for the acceleration of galactic cosmic rays. One of most energetic phenomenons in galactic scenario are Supernova explosions and corresponding rapidly expanding shell of ejected materials are called supernova remnants (SNRs). When the expanding shell of supernova explosion interacts with molecular cloud (MC) of nearby star forming region, it gives a strong possibility of producing gamma ray from hadronic origin. The energy released in supernova explosion provides strong evidence that these SNRs are sites of protons acceleration. The hadronic mechanism is the production of two gamma photons from the decay of a neutral pion created in a proton-proton interaction during the passage of SNR shocks through the dense molecular material. In this work, a middle aged SNR 3C 391, interacting with dense MC, is chosen which has been observed in $0.3 - 10$ KeV and GeV band by Suzaku and Fermi-LAT satellites respectively. We investigate the origin of gamma ray emission which would be either hadronic or leptonic in nature by studying the morphology and detailed spectral modeling. The five years Fermi-LAT data of 3C 391 (between $20008 - 08 - 04$ to $2013 - 08 - 18$) are analyzed as galactic pointlike source using Fermi Science Tool (FST) software. The standard binned likelihood analysis shows 13σ detection significance. The spectral properties were studied by comparing the observation with models of possible sources in the region of interest (ROI). The model of the analysis region contains the diffuse sources and all point-like sources from the 2nd Fermi-LAT catalog. To study spectral nature of 3C 391, both broken power law and log parabola model are used to find the best fit parameters. The long and short time flux variability are also studied. To check the hadronic and leptonic scenario from energy point of view, the converted energy of SN explosion into particle acceleration is considered. By considering luminosity and average cooling time of accelerated particles, the estimated energy is sufficient to accelerate protons. The Fermi data points are fitted with spectrum resulting from decay of neutral pions. The best fitted parameters do not change significantly for different forms of the input proton spectrum. The interacting SNR 3C 391 is concluded as the site of hadronic gamma ray origin.

In the group of galactic high energy sources, one of the interesting candidates are dark sources which are only detected in high energy (HE) or VHE regime but have no counter part in other wavelengths. The HAWC observatory has published a galactic survey catalog with 39 TeV sources, from which 19 of them have no association with known TeV sources. In 2006, H.E.S.S. collaboration had also performed a survey of galactic plane with a sensitivity of 2% of the Crab nebula flux above 200 GeV. It discovered 14 new sources, about half of them were unidentified sources and the other half in part pulsar-wind nebulae and SNR with $\geq 4\sigma$ significance after all trials [9]. HAWC catalog represents the spectral behavier of these sources in the energy range of $10 - 100 TeV$. To identify the nature of these new sources, observations at other energy ranges should be carried out. The MAGIC and Fermi-LAT provides excellent sensitivity to cover the high to very high energy range ($100GeV$ to $10TeV$). The combination of different mechanisms for separate energy ranges offers an opportunity to observe the universe over an wide energy band from $100MeV$ to $100TeV$. The HAWC catalog motivated the follow-up observation with Fermi-LAT and MAGIC which provides a multi-wavelength view of the interesting candidates. The extrapolation of HAWC spectrum over MAGIC sensitivity range provides strong evidence to chose three sources (out of 39 in HAWC catalog) as most promising candidates for MAGIC. These candidates are 2HAWC $J2006 + 341$, 2HAWC $J1907 + 084$ and 2HAWC $J1852 + 013$ which are situated within the field of view of previous MAGIC observations and therefore no dedicated observation have been performed. MAGIC observations are done in wobble mode in which telescopes are pointed slightly away from the source position(0.4 deg). This method allows simultaneous determination of background with source. The dedicated analysis have been performed for each sources which includes both pointlike and extended source assumptions. No significant detection was found from any of these sources under both pointlike and extended assumptions. The flux Upper Limits (UL) are estimated by assuming power law spectrum with index given in the second HAWC catalog. This non-detection in low energy range makes more difficult to predict the nature of these sources. The possibility of correlation with nearby pulsars are also denied by observational facts. The conclusion is that the sources are either more extended than our assumption or non emissive in the energy range > 100 GeV.

The sensitivity of present generation IACTs slowly start to saturate but the IACT technique can be still used to build better telescopes. In order to obtain better sensitivity, new generation IACTs are necessary which will be able to achieve order of magnitude better sensitivity with the help of proper distribution of different sized telescope in a telescopic array. Cherenkov Telescope Array (CTA) [11] is an international collaboration to build next generation IACT which is expected to provide 10 times better sensitivity than the present IACTs over a wide energy range from $20 GeV$ to $300 TeV$. To cover the entire sky, two observatories are proposed to be built, one in each hemisphere. The sites for northern and southern hemisphere array are respectively at La Palma, Spain and at Chile. The southern hemisphere array will host four Large-Sized Telescopes (LST), twenty Medium-Sized Telescopes (MST) and seventy Small-Sized Telescopes (SST) to cover full CTA energy range. The northern hemisphere array will consist of four LST and fifteen MST to cover low and mid energy range from $20 GeV$ to $20 TeV$ respectively (with best sensitivity). The 23 m diameter reflector of LST will be used to collect Cherenkov light from air shower initiated by incident gamma-ray and direct it onto the camera comprising of many photomultiplier tubes (PMT) read out by flash analog to digital converter

(ADC). The optical calibration of the camera is required to equalize the gain of each pixels by controlling the high voltage supply and calculate the conversion factor from ADC counts to number of photo-electrons. In this regard, a calibration system for a prototype LST of the northern hemisphere array has been built by India through a collaboration of SINP & TIFR. The main components of this system are a stable monochromatic light source (i.e. laser), optical filters, light diffuser, a microcontroller named Raspberry Pi (Credit card sized PC) and supporting electronics. A water tight metal enclosure with temperature control system is used for housing of all these elements. The communication with the calibration system will be controlled by OPC Unified Architecture (OPC UA) [12] communication protocol. The geometrical simulation has been done to estimate the optimal cavity size which maximizes the diffuser output. The characterization of calibration system includes the precise estimation of all of it's properties. The photon numbers are estimated for all possible filter combinations over a vertical plane at a distance of 28m and measure the linearity of this number with filter's optical density (OD). The uniformity of diffuse light beam has been studied over the whole camera plane at 28m distance. The stability of temperature and humidity over time and it's effect on light output are also observed. The final system meets almost all requirements given by CTA collaboration. This system will be installed on the first prototype LST at northern hemisphere array of CTA in first half of 2019.

List of Figures

List of Tables

CHAPTER 1

Basics of Gamma-ray Astronomy

Introduction

The trend of modern physics is to explore fundamental interactions from microscopic level. Smaller dimension can only be revealed with help of higher and higher energies. This requirement makes 'high energy physics' is an important part of 'fundamental physics' in the twenty first century. The attainable energy range of present generation accelerators is quite well to describe three of four fundamental interactions (electromagnetic, weak and strong interaction). The signature of unification between these forces and the forth, gravity, might manifest themselves at extreme energies. The physical requirements to reach this extreme energy is still unknown and cannot be produced in earth-based laboratory. Astronomy can be described as the science that allows us to understand the physics of the phenomenas that occur outside earth's atmosphere. The observation of violent astrophysical phenomena like supernova remnant, active galactic nuclei and detection of cosmic particles of energy upto 10^{20} eV give clear hints that one can use natural events as in-build laboratory to study high physics era.

In recent years substantial experimental efforts have been done to investigate the physics issues involved in most energetic phenomena of our galaxy and beyond it. The only probes to study these events are the cosmic messengers reaching earth from outer universe. The cosmic ray (CR), most dominant and easily detectable cosmic messengers, mainly consist of high energy nuclear particles (predominantly protons, but also nuclei of higher elements) with a small admixture of electron and γ-photons. This was first discovered by Viktor Hess in 1912 [29] with a series of balloons experiment. At the beginning, it was considered as a new energetic radiation which misguides the nomenclature. The corpuscular nature of CR was discovered by Bothe & Kolhorster [30] in 1929. The measured CR spectrum extends beyond 10^{20} eV, far above the present accessible range of earth-based accelerator. In spite of being easily detectable, CR is not a potential probes to explore high energy universe because

1. The charged CR are deflected in galactic and extra-galactic magnetic field and therefore they can not be used to trace back to their sources. Only extreme energy CR could point to their sources. But decaying nature of CR power law spectrum provides very low flux at this extreme energy and requires huge collection area to collect statistically reliable data.

The neutral messengers, like γ photon, neutrino and neutron, are more efficient than their charge counter part. The free neutron are unstable with a decay time of 886 s and therefore long distance neutron are not detectable. The very low interaction cross section makes neutrino highly penetrating particle. The huge detectors are needed to detect them and directional accuracy is limited at present. Thus γ-rays are the most preferred messengers. The violent events of outer universe emit significant fraction of their energy in form of gamma photons ($\sim$MeV to tens of TeV). The branch of astronomy which involves the observation and analysis of these gamma photons is known as Gamma-ray astronomy. This wide energy range of gamma photon is divided in several sub domains for practical purposes and all of

Name	Abbreviation	Energy Range
Low Energy	LE	1 MeV - 30 MeV
High Energy	HE	30 MeV - 50 GeV
Very High Energy	VHE	50 GeV - 100 TeV
Ultra High Energy	UHE	100 TeV - 100 PeV
Extremely High Energy	EHE	above 100 PeV

Table 1.1: The different sub domains of gamma-ray astronomy and their abbreviation with corresponding energy range are presented

them are shown in table [1.1].

This thesis work is mainly focused in HE & VHE regime of gamma-ray astophysics.

Why Gamma-ray Astronomy?

- One of the major motivations behind the study of gamma-ray astrophysics is to explore the physics of CRs. The measured CR spectrum extends from 10^6 eV to 10^{20} eV [1.1]. The spectrum follows a power law distribution of form $\frac{dF}{dE} \propto E^{-\alpha}$. The spectral index ($\alpha$) bears a value of 2.7 upto 10^{15} eV where spectrum becomes more steeper. This energies is known as 'Knee'. After 'Knee', spectral index becomes 3.0. At extreme energies (10^{18} eV), the spectrum becomes flatter and the value of α becomes $\sim$ 2.7. The second feature is called 'Ankle' as shown in figure [1.1]. It is mostly believed that CRs upto Knee are of galactic origin. But there is still a scope of speculation about the upper boundary of galactic CR. Despite extensive efforts on both theoretical and experimental field, the origin of CRs have still remained unresolved after their discovery in 1912. The physical processes i.e. mechanisms which can acceleration particles upto 10^{18} eV and beyond that, are still not known. There is a close connection between the production of cosmic ray and γ photons. The CR sources mainly accelerates protons and part of these particles interact with interstellar medium to produce γ photons as a decay product of neutral

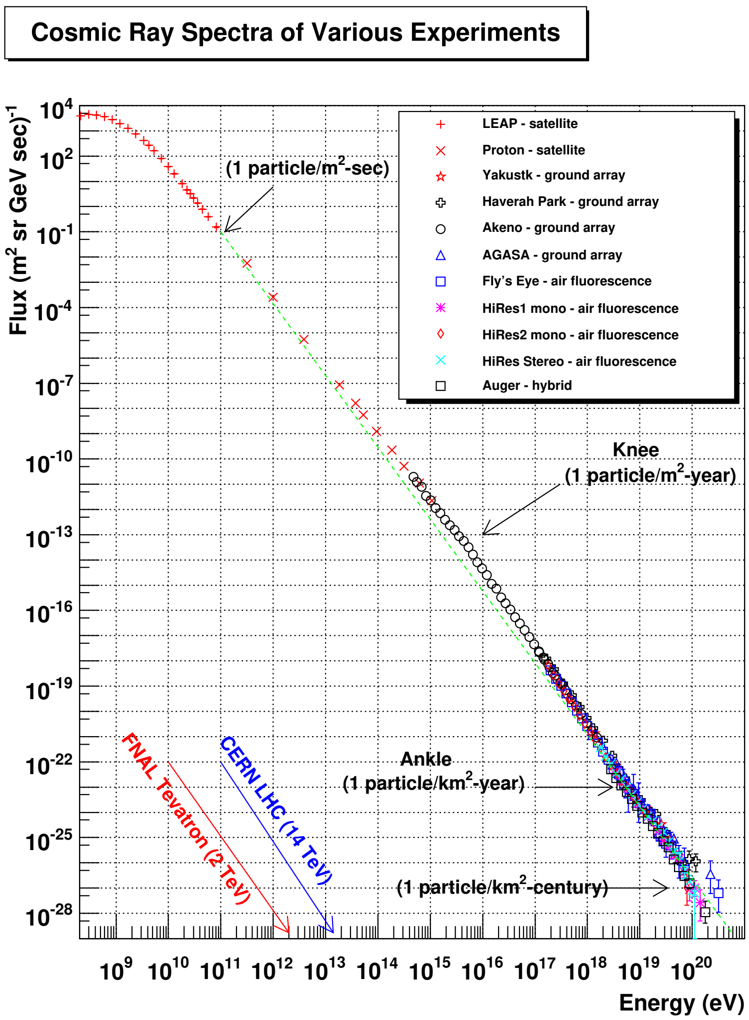

Figure 1.1: Observed Cosmic ray flux spectrum above 10^8 eV. The spectrum follows the power law spectrum of index 2.7 upto 10^{15} eV and becomes more steeper with index 3.0. Around 10^{18} eV, spectrum index returns to original value of 2.7. These energies, where spectrum bends abruptly, are mentioned as ' Knee' and ' Ankle' respectively. The data are taken from different satellite and ground based experiments. The highest attainable energy in man made accelerator are also depicted. This figure is taken from: [http://www.physics.utah.edu/~whanlon/spectrum.html]

Pi mesons. The characteristics of this gamma spectrum will be different from other production mechanisms. The study of observed gamma spectrum from sources can reveal the sources of cosmic rays.

- Another motivation behind the study of gamma-ray astronomy is to estimate the density of intergalactic radiation field. This radiation field is mainly dominated by far and near infrared radiation (FIR and NIR). The VHE γ-photons from distant sources has a finite probability to interact with NIR and FIR photon field ($\gamma\gamma \rightarrow e^{+}e^{-}$). Therefore the observed spectrum of distant object would be different from original spectrum. If the intrinsic spectrum can be obtained from other observations, the radiation density can be estimated from spectral measurements of extra galactic sources.

- Presently search for dark matter is one of the biggest challenges of experimental physics. The gamma-ray astronomy opens an indirect way to detect the signature of dark matter. The annihilation of dark matter could produce γ-photons upto the energy of few TeV. The study of excess gamma radiation from the direction of galactic center which is not associated with any known sources may reveal the existence of dark matter.

History and Development of Gamma-ray astronomy

In 1958, Philip Morrison [31] wrote a seminal paper on the future perspectives of studying Cosmic rays. He realized that the presence of high energy electrons and strong magnetic field in energetic radio sources, could produce gamma photons and proposed to observe radio loud sources in $0.4 - 400$ MeV energy band. This was the first published document in Gamma-ray astronomy. In 1959, Cocconi [32] published a theoretical model which predicts TeV γ-photons from Crab Nebula. Though the model was oversimplified, the dawn of gamma-ray astronomy was about to break.

The detection of cosmic gamma photon was started in 1953 with an excellent initiative to detect air Cherenkov radiation by Bill Galbraith and John Jelley [33]. They were guided by a previous observation made by P. M. S. Blackett (1948) [34] who had noticed the presence of small fraction of Cherenkov photons in lower atmosphere. Blackett proposed the presence of Cherenkov photons as the secondary products of atmospheric interaction of cosmic particles. Galbraith and Jelly used a simple arrangement, 25 cm parabolic mirror with a photomultiplier tube (PMT) at its focus, to detect the Cherenkov photons from extensive air shower. This was the beginning of a new era in experimental gamma-ray astrophysics. The first successful gamma-ray detection experiment was started from space because earth atmosphere is completely opaque to low energy gamma-photons. Explorer XI [35, 36] in 1962 and it's successor OSO-3 [37] in 1968 were first two dedicated gamma-ray detector satellites. The first signal of an astrophysical object in gamma photons was the galactic plane. The OSO-3 observed galactic plane and produced first gamma-ray map in the energy range from 30 to 50 MeV. In 1972, NASA planed a mission SAS-2 [38], unfortunately, which had a very short life time. In short lifespan, SAS-2 discovered the presence of diffuse $\gamma-$ray background. The COS-B [39] satellite, launched in 1975, was produced first sky map of galactic continuum emission and point sources with 7 years data [40]. These point sources includes pulsars in Crab and Vela supernova remnants and quasar 3C 273. The next big achievement of low energy gamma-ray detection was the launching of Energetic Gamma-ray Experiment Telescope (EGRET) as a part of Compton Gamma-ray Observatory (CGRO) [41] in 1991. The EGRET [42], containing wire spark chamber, observed entire sky for 9 years in energy range $>$ 30 MeV. The integrated mission CGRO also contained gamma spectrometer COMPTEL [43] for continuum emission and BATSE [44] for burst and transient detection. The first detailed GeV sky map revealed a large number of GeV sources which had no previous counterparts. The next milestone in the timeline of space based $\gamma-$experiment was launching of INTErnational Gamma-Ray Astrophysics Laboratory (INTEGRAL) [45] in 2002 for detecting low energy gamma photon in the range from 15 KeV to 10 MeV. The primary gamma spectrometer aboard INTEGRAL is SPI [46]. The all-sky coverage and sensitivity make it a natural gamma-ray burst detector. The Gamma Large Area Space Telescope (GLAST), currently called Fermi Observatory, is the most sensitive operational $\gamma-$ray satellite detector which was launched by NASA in 2008. This mission contained two instruments Fermi Large Area Telescope (Fermi-LAT) and Gamma Burst Monitor (GRB). The Fermi-LAT is the primary gamma detector of Fermi Observatory and GBM is specially designed for gamma burst detection. This mission extended the search over wide energy range from 30 MeV to 300 of GeV and discovered hundreds of new sources. The hardware part and detection mechanism of Fermi Large Area Telescope [1] (Fermi-LAT) are described in *Chapter 2*.

In contrast, the development of the field of high energy gamma-ray astronomy ($>$ 100 GeV) has been a more haphazard and painstaking process [16]. The primary particle initiates an electromagnetic shower high in the earths atmosphere and the charged component in the ensuing cascade speeds to earth faster than the phase velocity of light in the transparent atmosphere, radiating Cerenkov light in flight. The ground based detector are constructed to form an image of shower by collecting the Cherenkov photons. Unfortunately, this gamma-ray signal has to be picked out against a generally overwhelming background of hadronic cascades induced by cosmic particles. It was a big technological challenge that how to reject this unwanted hadronic background at some remarkably high level of efficiency. In 1968, a 10m optical reflector with tessellated mirrors was implemented at the Whipple Observatory [47] in southern Arizona, USA. This was the first attempt to detect high energy gamma photon ($>$ 100 GeV) using Imaging Atmospheric Cherenkov (IAC) technique. In 1972, they reported their first detection of excess events from the Crab Nebula at a significance level of 3.1σ [48]. Using sophisticated analysis method, Crab nebula was first detected in 1989 with 9σ confidence after 50h observation [49]. The next big technical achievement was the implementation of multi telescope array for stereoscopic observation. The stereoscopic method provides better angular resolution by 3D reconstruction of atmospheric air shower. The High Energy Gamma Ray Astronomy (HEGRA) [50, 51] telescope array on La Palma, Spain in 1991 was pioneered to use this idea. This array uses five 3.5m IACT reflectors to achieve better sensitivity and angular resolution for next 7 years. Present generation IAC telescopes like MAGIC [3, 4], H.E.S.S. [52] and VERITAS [53] use large mirror and fine camera pixelation to achieve better sensitivity. The detailed descriptions of MAGIC hardware and analysis method are given in *Chapter 2*

Production mechanisms of VHE Gamma-ray

Before the discovery of CR, astronomy mainly deals with thermal radiations that can be described by Planck's formula of blackbody radiation. This process translates heat energy to photons in the range from infrared to X-ray. The hottest objects in the universe can emit X-rays in the energy of few KeV. Higher γ-ray energizes can only be reached in non-thermal processes. The emission of γ-rays is always associated with accelerated charge particles in VHE regime. For this reason, identification of γ-ray sources is strictly related to cosmic regions where ultra relativistic leptons or protons are present.

There are several non thermal processes that involve the production of VHE gamma photons. The astrophysical gamma-rays can be produced from both hadronic and leptonic origins. Normally, several of these mechanisms combine to shape the γrays outflow from a given source. In hadronic origin, interaction of high energy protons with interstellar medium and decay of secondary products produce gamma photons.

Figure 1.2: World map of presently working Imaging Atmospheric Cherenkov telescopes.

This is called neutral pion decay. On the other hand, the combination of radiative processes based on interaction of electrons is defined as leptonic origin. This involves inverse Compton, synchrotron and bremsstrahlung processes. The hadronic process of neutral pion decay and IC scattering are the most important sources of VHE γrays. We will briefly describe them in the following. For more information refer to [54, 55].

Photons produced by High Energy Protons

Neutral Pion Decay

Relativistic protons and nuclei interact with interstellar medium (ISM) through inelastic collisions and produce basically mesons, kaons and hyperons via strong interactions. The pseudoscalar π-mesons are produced in equal amounts of positive, negetive, and nuetral charged and one third of total pions are neutral. While charged pions decay predominantly in muons and neutrions via weak interaction, the neutral ones decay electromagnetically in gamma photons with a short life time of 8.6×10^{-17} s

$$\pi^0 \to \gamma + \gamma \qquad \text{(B.R. 98.2\%)} \; ,$$
$$\pi^0 \to \gamma + e^+ + e^- \quad \text{(B.R. 1.8\%)} \; .$$

The minimum kinetic energy of proton to produce a π^0 is

$$E_{th} = \frac{2m_{\pi^0}c^2(1 + m_{\pi^0})}{4m_p} \simeq 280 \text{ MeV}$$

The energy of photons emitted by a π^0 at rest is peaked at $E_\gamma = m_{\pi^0}c^2/2 \simeq 67.5$ MeV, whereas in laboratory frame it depends on emission angel and on the initial energy of meson.

This process is called hadronic origin of γ-photon. They are distinguishable from those of electromagnetic origin because of their spectra, lack of correlation with X-rays, and presence of molecular clouds, and they occur together with a flux of neutrinos coming from the charged pion decays, whose spectrum is similar to that of γrays from π_0 decay. This mechanism can produce highest energy γ-photons upto tens of TeV.

Photons produced by High Energy Electrons

Synchrotron radiation

If a charged particle is forced by magnetic field to follow a curved trajectory they emit synchrotron radiation. The radiated synchrotron power P is [56]

$$P = \frac{1}{6\pi\varepsilon_0}\frac{e^2a^2}{c^3}\gamma^4$$

where e is the charge of the particle and a is the centripetal acceleration. Since P is strongly dependent on the mass of the particle, synchrotron radiation is only relevant for electron/positron. In case of proton, this process is considered as insufficient process to produce VHE $\gamma-$photon.

When particles are relativistic, the entire radiation is beamed in a cone centered on the particle and with an angular spread $\alpha \simeq mc^2/E$. The spectrum of synchrotron radiation of mono-energetic electrons is a continuum that peaks at

$$E_\gamma = 1.5 \cdot 10^{-5}(\frac{E_e}{[TeV]})^2 \cdot (\frac{B}{[G]}) \text{ GeV}$$

where E_e is the energy of the electron and B is the magnetic field component perpendicular to the plane of the particle trajectory. Synchrotron radiation of accelerated electrons is one of the most important process in the non-thermal Universe. In the context of VHE $\gamma-$rays, synchrotron radiation is the usual process for the generation of seed photons for Inverse Compton scattering. However, UHE CRs (electrons and/or protons) can emit synchrotron radiation directly in the VHE domain.

Inverse Compton scattering

In the Inverse Compton Process a relativistic particle (specially electron) interacts with a low energy photon and transfer a considerable fraction of it's kinetic energy to upscatter photon in high energy regime. Most of the VHE -ray photons we detect are produced by Inverse Compton (IC). One can distinguish two different regimes, the Thomson limit ($\gamma\varepsilon \ll m_e c^2$) and and the Klein-Nishina limit ($\gamma\varepsilon \gg m_e c^2$), where ε is the photon energy before the scattering process and γ is the Lorentz factor of the relativistic electron. The average energy of the photon after the scattering is

$$\langle E_\gamma \rangle \simeq \frac{4}{3}\langle\varepsilon\rangle\gamma^2 \quad \text{Thomson limit },$$
$$\langle E_\gamma \rangle \simeq \frac{1}{2}\langle E_e\rangle \quad \text{Klein-Nishina limit }.$$

where E_e is the energy of the electron. The Cosmic Microwave Background (CMB), NIR and FIR photon field are generally used as the low energy seed photons. The emitted spectrum depends on the spectrum and density of the target photons and on the velocity distribution of the involved electrons. In particular, the IC process is important in the production of high energy γ rays in the jets of Pulsar wind nebulae and Active Galactic Nuclei.

Bremsstrahlung

Bremsstrahlung occurs when charge particles are accelerated in an electric field. Since acceleration is inversely proportional to the rest mass of particle, the lighter particles like electron/positron are more favourable for this process. When electron passes through a medium, it deflects in the presence of electric field of the atomic nucleus. This instantaneous acceleration converts a fraction of particle's kinetic energy into radiation. The photons are emitted in the forward direction of the particle, within an angle $\theta \approx 1/\gamma$ with a continuous spectrum which approximately flats up to an energy of the electron kinetic energy. Bremsstrahlung occurs when charge particle's energy crosses a threshold value, below which ionization is dominant energy loss mechanism. This process mainly observed in astrophysical regions that contain ionized gas molecules, such as gaseous nebula. These photons are mainly served as the seed photons in IC process. This process also plays an important role in development of atmospheric air shower.

Astrophysical Sources of VHE $\gamma-$rays

Presently, different types of gamma-ray sources are discovered both inside and outside of our MilkyWay galaxy. The sky map of gamma-ray sources above 1 GeV are shown in fig.1.3. The notable fact is that galactic plane contains most of the galactic $\gamma-$ray sources including diffuse gamma-ray background. The supernova remnants are the most promising galactic gamma-ray source. The other galactic sources are high spin down pulsars and it's nebulae and X-ray binaries. For extra galactic counterpart, active galactic nuclei are the most prominent source of VHE gamma-ray. The brief description of all these sources are given below.

Galactic Sources

Galactic sources are of various importance in studying origin of cosmic ray. These sources can be observed in great details due to short distance compared to extra galactic sources. This provides an unique opportunity to observe and study the morphology of extended sources. Moreover, these gamma emission does not suffer absorption of cosmological background light.

- **Supernova Remnants**

  A supernova remnant (SNR) is the ejecta of supernova explosion of massive

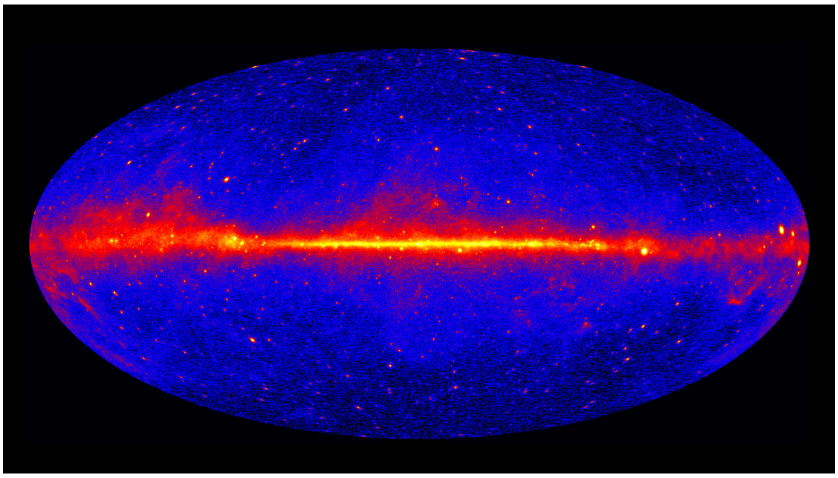

Figure 1.3: The Fermi LAT 60-month image, constructed from front-converting gamma rays with energies greater than 1 GeV. The most prominent feature is the bright band of diffuse glow along the map's center, which marks the central plane of our Milky Way galaxy. This figure is taken from: [https://fermi.gsfc.nasa.gov/ssc/]

star ($\sim 5M_{\odot}$). When a massive star run out of it's fuel for nuclear fusion reaction, self gravitational force starts to squeeze materials in a more denser state. This results a huge explosion which blows out a substantial fraction of material into surrounding interstellar medium (ISM). The remaining part of the star turns into a neutron star or a black hole depending on the mass of leftover part. The ejecting materials produce a supersonic shock wave when traverse through the surrounding low density ISM. The shock wave magnetic field irregularities scatter charged particles back and forth across the shock front and this diffusion of charge particle leads to a net gain of energy after many such scatterings. This process of accelerating charge particles through shock wave is called Fermi acceleration mechanism [57]. Thus supernova remnants are believed to be a potential source of galactic cosmic ray up to 10^{15} eV [58,59]. SNRs interacting with dense molecular cloud are also important as the possible site of hadronic origin of VHE $\gamma-$radiation. In case of hadronic origin, the emitted spectrum of SNRs is thought to be the combination of radio synchrotron radiation and VHE $\gamma-$ray peak from neutral pion decay.

The best known object of this kind is Crab nebula. This is the remnant of a supernova explosion on 1054 AD, documented by Chinese astronomers. This is one of the brightest sources in hard X-ray and $\gamma-$ray sky and extremely steady in terms of flux consistency. These characteristics led to consider Crab as a standard candle in $\gamma-$ray astronomy [60]. But the detail study of recent GeV Crab data revealed evidences in support of short-term flux variation. The discovery of short term flares from Crab was first reported by Fermi-LAT [61] and AGILE [62], gamma-ray detector satellite of Italian Space Agency, in 2011. The most violent flare of Crab to date was observed on April 2011 [63]. The inconspicuous nature of flares on the other parts of electromagnetic spectrum makes difficult to understand the flaring mechanism. The short duration of flares indicates synchrotron loss of high energy electrons as the possible mechanism of flare [61].

- **Pulsars and it's surrounding Nebula**

A pulsar is a extremely magnetized rotating neutron star which is created in the aftermath of supernova explosion and characterized by precisely maintained rotational period. The strong rotating magnetic field of a pulsar produces an ultra relativistic particle jet from magnetic poles. This flow of particles is considered to be of leptonic nature. This wind of particles flows out freely until it's pressure is balanced by that of the surrounding medium, at which point the wind decelerates and a standing termination shock forms, resulting in acceleration of the particles via second order Fermi acceleration [57,64,65]. This termination shock produce a luminous nebula around the pulsar, called pulsar wind nebula (PWN). Thus pulsar polar wind continuously energies the nebula at the expense of pulsar rotational kinetic energy [66].

The PWNe consists of two types of electron populations, one is generated from pulsar's own magnetic field called radio electrons and other is accelerated in termination shock called wind electrons [67]. The radio electrons produce synchrotron radiation from radio to soft$-\gamma$ range and wind electrons are mainly participating in IC process to generate VHE $\gamma-$photons. The CMB and synchrotron photons, generated by radio electrons, are used as seed photon field in IC process. The PWNe are known to be the most populous galactic VHE gamma emitters [68].

- **High mass X-ray Binaries**

  Apart from SNRs and PWNe, there are some other class of galactic VHE gamma emitter called High mass X-ray binaries (HMXB). These objects are most luminous in X-rays and that justifies it's nomenclature. The HMXBs consist of two objects rotating around each other and one of them is a compact object like neutron star or Black hole and the other one is a massive star. The compact object, due to it's strong gravity, starts to extract materials from the massive star. The small surface area of compact object decreases the accumulation rate of falling materials. Thus the extracted materials try to rotate with the compact object in an orbital plane and forms the accretion disk. The released gravitational potential energy of infalling matter produces thermal radiation upto X-rays (small fraction in visible light) and strong particle jets. The particle jets are considered as the source of VHE $\gamma-$radiation [69]. The HMXB objects are classified in two categories based on the nature of companion massive star: binary pulsar and microquasars. Five such objects are known to emit VHE gamma rays to date: LSI+61 303 [70], HESS J0632+057 [71], HESS J1018-589 [72], PSR B1259-63 [73] and LS 5039 [74].

- **Galactic Center**

  The center of Milky Way galaxy is crowded with many astrophysical sources that can not be identified separately. The evolution of these sources plays an crucial role in producing and determining the spectrum of galactic $\gamma-$ray emission. The galactic center (GC) has been discovered as a strong and steady source of VHE $\gamma-$ray by H.E.S.S [75] and MAGIC collaboration [76]. The observations confirm a quite hard gamma emission with spectral index ~ 2.2 and a light curve which does not show any variability on time-scales from hours to years. The exact description of emission mechanism is still not known because of dense accumulation of different potential sources in a small region and the angular resolution of present generation telescopes is not sufficient to identify exact location of $\gamma-$ray emission. The next generation observatoty, like Cherenkov Telescope Array (CTA), with improved sensitivity might be able to explore these region in great detail. It is assumed that most important GC $\gamma-$emitter is a supermassive black hole SgrA* [77, 78]. The presence of dense molecular cloud around GC can act as a soft target for shock wave interaction and enhances the possibility of hadronic gamma emission. The recent scenarios includes Dark matter particles (WIMPs) annihilation mechanism as a potential component of galactic gamma emission.

Extra galactic Sources

The universe is not completely transparent to VHE $\gamma-$rays. The interaction of $\gamma-$photons with Extragalactic Background Light (EBL) [79–81]produce electron-positron pair which cease the VHE $\gamma-$photons from high red shift objects. In spite of this constraint, a number of extra galactic objects have been discovered. The description is given below

- **Active Galactic Nuclei**

  Active galactic nuclei (AGNs) [82] are the most prominent extra galactic TeV gamma ray sources. An AGN is a compact region at the center of the galaxy that has much higher than normal luminosity in some part of electromagnetic spectrum, with characteristics indicating that the excess luminosity is not produced by stars. The galaxy hosting AGN is called active galaxy. According to the standard model of AGNs [83,84], it is believed that AGN is powered by accretion energy of a supermassive black hole. Supermassive black holes (10^6 to 10^{10} solar mass) [85] are now believed to exist in the center of most of the massive galaxies. When the supermassive black hole starts to accumulate cold materials, the surrounding masses form an accretion disc. The frictional energy released in accretion disc produces thermal radiation upto X-ray regime and the gravitational energy loss of infalling masses powered an ultra relativistic particle jet [86]. Particle acceleration takes place throughout the entire jet. These particles interact with ambient photon and magnetic fields, thereby giving rise to non-thermal emission. The radiation from AGN covers a wide range of electromagnetic spectrum from radio to VHE gamma-ray. The energy emitted by the AGN is greater than the total energy released by stars. Blazars are a special type of AGNs with their relativistic jets pointing towards the earth.

- **Gamma Ray Burst**

  Gamma Ray Bursts (GRBs) are the most violent and short term phenomena observed in universe. The highly luminous photon flux exist for fraction of seconds to several minutes. This short term behavior of this object is very mysterious. The complete theoretical explanation of this event is still not known. But it is believed that most possible source of transient event is asymmetric supernova explosion. The BATSE [44] of Compton Gamma observatory was the first dedicated detector for the observation of GRBs. Presently Fermi-LAT and other ground based detector are suitable to observe these events.

CHAPTER 2

Detection Techniques of VHE Gamma Photons

In this chapter, we describe the various detection techniques of present day gamma-ray astronomy which involves most sophisticated and advanced technology of the twenty first century. This chapter is mainly focused on the technical parts of observational gamma-ray astronomy. First we discuss the classification and basic theory of different detection procedures with their natural difficulties in implementation. In the subsequent section, we explain the utilization of advanced technology to overcome these barriers as the part of detailed technical description of different telescopes. The data from all the listed telescopes are used extensively in this thesis.

Introduction

The present day gamma ray astronomy covers a wide range of electromagnetic (EM) spectrum from few tens of MeV to few tens of TeV. The incoming photon flux, strength and type of interaction with ambient medium depend on primary photon energy. Thus detection of photon over this wide energy range requires a combination of different detection techniques. Based on detection efficiency, different methods are used in different energy range and sufficiently overlap between observable energy ranges of different techniques make its a continuous energy band.

Method of direct detection of gamma photons

The appellation of the technique implies direct encounter of primary particle i.e. gamma photon with detector without producing any kind of secondary components. The earth atmosphere stops most types of the electromagnetic (EM) radiation from space from hitting earth's surface. The observation can only be done in radio, optical and part of ulta violet radiation from sea level as shown in fig. [2.1]. The direct detection of photons with ground based detector is only possible for optical and radio part of EM spectrum. To overcome the difficulty in detecting radiation from rest of EM spectrum, we have to place our detectors above atmosphere. This idea was first implemented in the γ-ray detection from astrophysical sources in 1960s (see in *chapter 1*)and opened the era of satellite based astronomy.

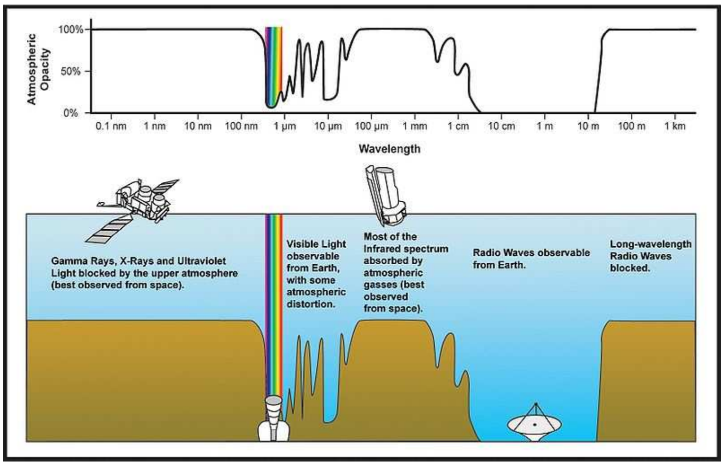

Figure 2.1: Rough plot of Earth's atmospheric transmittance (or opacity) to various wavelengths of electromagnetic radiation, including radio waves. This plot has been taken from: [http://en.wikipedia.org/wiki/Image:Atmospheric_electromagnetic_transmittance_or_opacity.jpg]

The direct detection method is mainly applicable for photons of energy from hundreds of MeV to tens of GeV i.e. HE regime of gamma-ray astronomy (see Table [1.1]). Beyond this range, detection is possible but statistics will be very low. Implementation of direct detection method requires details knowledge of photon interaction with material particles. The photon-material particle interaction strongly depends on the energy of the incident photons. The photoelectric effect is dominant for photon energy $<$ 100 KeV. For photon energy between 100 KeV to 10 MeV, the most important process is Compton scattering and electron-positron pair production is dominant for energy above 10 MeV [36]. The low interaction cross-section of photoelectric effect in gamma energy regime makes it inappropriate for direct detection. The Compton scattering and pair production both processes are used to cover the LE & HE range of γ-ray astronomy. For more details refer to [54, 55].

Basic principles

The goal of astronomical observation is to extract the maximum possible informations from incoming photons like arrival direction, energy and arrival time i.e. time of detection. In the HE regime of gamma-ray astronomy, the widely used detection mechanism is $e^{\pm}$ pair production. The violation of conservation of momentum ceases the process of pair production to occur in free space and requires the presence of heavy nuclei as converter which can absorb a part of momentum. The heavy mass of converter compared to that of $e^{\pm}$ pair also ensures almost zero energy loss to converter.

The first essential component for direct detection γ detector is to choose a converter material. The material with high atomic number, like lead, are generally chosen because high Z materials have shorter radiation length. The short radiation length minimizes the mass of converter material which is required to achieve a reasonable probability to detect gamma photons.

The estimation of incoming direction and energy are the most important part of astrophysical observation. The arrival time information is generally obtained by registering the first interaction moment of primary photon with the converter material. Since e^+ and e^- carry almost all of the energy of incoming photon (at least for energy much greater than total rest mass energy of electron and positron), arrival direction can only be inferred by tracing back the trajectory of secondary charged particles after the point of pair production. The higher interaction probability of charged components makes it much easier to detect and trace out than neutral particles. So the second essential component is a charge particle tracker which is same as used in nuclear and particle physics experiments but with much higher positional accuracy. The separation angle ($\theta_{separation}$), in radians, between electron and positron trajectory is related to incoming photon energy via [13, 87]

$$\theta_{separation} = \frac{0.8}{E_\gamma}$$

where E_γ is the energy of primary photon in MeV. The separation angle decreases with increasing energy of photon and become very small for E_γ greater than 100 MeV. So in that limit, the charge particle trajectory can directly be used to estimate the arrival photon direction.

The previous description of converter and tracker is from theoretical point of view. In case of application field, situation is little bit complicated. The charged particles like $e^\pm$, while passing through converter and tracker material, interact via multiple Coulomb scattering. This process slowly degrades the incoming direction information of photon. In Gaussian approximation, for $e^\pm$ pair, the root mean square scattering angle θ_0 in radians is given by [88]

$$\theta_0 = \frac{13.6 \text{ MeV}}{\beta c p}\sqrt{\chi/X_0}[1 + 0.038ln(\chi/X_0)]$$

where βc and p are respectively the velocity and momentum of the corresponding particle, χ is the thickness of the material and X_0 denotes the one radiation length. Thus for constant thickness, material with shorter radiation length produce more deviation and quickly erases most of the information about arrival direction of incoming photon. This is a big disadvantage to use a thick layer of high Z material (i.e. short radiation length) which is previously chosen as an efficient converter material. Since θ_0 depends only on the ratio (χ/X_0), the use of multiple thin layers instead of a thick one minimizes the value of θ_0. The general idea is to divide the converter into multiple thin layers which are interleaved by tracker material. This idea is depicted in fig. [2.2].

The another bit of essential information is the incoming photon energy. This can be approximated by measuring separately the energy of each secondary charge particles. In case of γ-photon pair production with high Z converter, this approximation is perfectly applicable because energy loss in converter is almost zero. The energy estimation requires a calorimeter which can measure the total energy deposited due to the electromagnetic particle shower that results from the e^+ e^- pair production. The measured energy value should be corrected for the energy losses in tracker and other mediums which they pass through before calorimeter. for more details refer to [55].

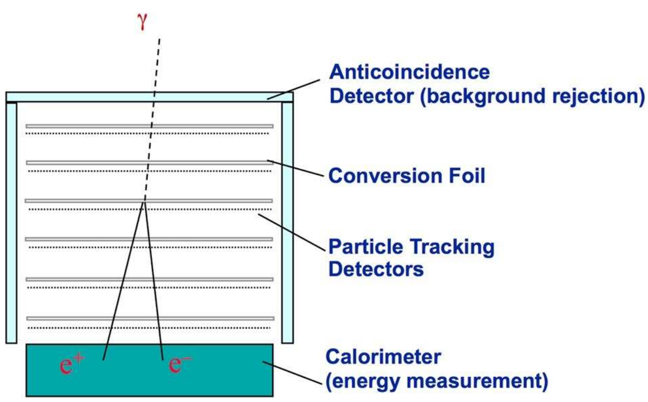

Figure 2.2: Basic structure of satellite based gamma detector. The picture is taken from [13].

Natural difficulties in implementation

After Viktor Hess discovered cosmic rays in 1912 [29], different experiments revealed the existence of charge particle in earth's atmosphere and beyond it. Solar and earth's magnetic fields are not sufficient to stop charge particles penetration in upper atmosphere having energy beyond ~ 1 GeV/particle [54]. This incoming charge particle flux is mainly filled with hardonic and leptonic components of cosmic ray and creates a constant charge particle background whose flux is order of magnitude higher than gamma photon flux. Background particles can hit detector from any direction. The detection of gamma photons against this overwhelming charge background is the biggest challenge of satellite based gamma detector. This charge background can also be harmful for electronics and hardware part of detector itself.

The basic idea to identify the charge particle background is to wrap the active detector with a shield which is only sensitive to charge particle interaction. The charge particle penetration can be confirmed by two consecutive signals, one from outer shield and other from tracker, which are in coincidence within a predefined short time window. In other words, the absence of outer shield signal within the coincidence time period of each tracker signal ensures the gamma photon detection. This shield is known as anti-coincidence detector (ACD) [fig. 2.2]. The plastic scintillator is generally chosen for anti-coincidence detector because of it's high efficiency in charge particle detection and low probability in absorbing gamma photons. The coincidence of ACD and tracker signal is feeded to trigger system which in turn reject the corresponding event. The ACD shield can never be used to cover the bottom part of calorimeter because, for high energy photons, some shower components may penetrate through calorimeter. In practical cases, there is always some probability of leakage through ACD detector which are considered in systematic errors of detector. For more details, refer to [13, 54, 55].

Description of Fermi Gamma-ray Space Telescope

After the success of Compton Gamma-Ray Observatory (CGRO) [41] mission, the launch of Fermi Gamma-ray Space Telescope (Fermi), formerly the Gamma-ray Large Area Space Telescope (GLAST) [89] mission, was a revolution in satellite based gamma-ray astronomy. Fermi observatory, built by an international collaboration of 10 countries, had been launched by NASA on June 11, 2008 on a Delta II Heavy launch vehicle. In the next 10 years upto now, this offered an enormous opportunity to explore high energy universe in the GeV range.

Fermi observatory encompasses two instruments in low earth orbit. The primary one is Large Area Telescope (LAT) [2] and the other one is Gamma-ray Burst Monitor (GBM) [90]. The LAT is a pair conversion gamma telescope capable of detecting and measuring the properties of individual gamma photons in GeV range. The GBM is a dedicated instrument to extensively study the gamma-ray burst phenomena. The primary goal of GBM is to extend the spectral range of burst observation downward to hard X-ray from lower energy threshold of LAT ($\sim$8 KeV to $\sim$40 MeV), so that LAT-GBM combination provides observation over broad energy band. The other important task of GBM is to search and locate gamma burst event over the entire unocculted sky and inform LAT. For strong bursts, it can re-orient the spacecraft to allow delayed burst observation with both onboard instruments (nominally for $\sim$5 hrs). The GBM detector consists of two types of detectors, thallium activated sodium iodide (NaI(Tl)) and bismuth germanate (BGO) scintillation detector. Twelve NaI(Tl) detectors are distributed all over the spacecraft, so that their relative photon detection rates provide the burst location. Two BGO detectors have been used to detect burst from the horizon of occulted sky region. The onboard trigger threshold for transient event detection is $\sim$0.7 ph cm^{-2} s^{-1} ($50 - 300$ KeV). In recent years, LAT-GBM combination detected several gamma burst events.

The LAT [fig. 2.3] is an imaging, wide field of view, direct detection gamma-ray telescope, capable of detecting photons in the energy range of 20 MeV to 300 GeV. LAT rotates around the earth in a low earth orbit at ∼565 km with 25.5^0 inclination. Fermi satellite normally operates in an all-sky survey mode. For nearly uniform exposure over all sky, the normal to the front of the instrument (z-axis) is pointed to $+35^0$ from the zenith towards the north orbital pole in one orbit and then towards -35^0 of the south orbital pole in subsequent orbit. In this way, Fermi takes nearly 3 hours to complete one full sky survey.

Fermi-LAT consists of a precision converter-tracker with anti-coincidence shield (ACD), a calorimeter and data acquisition system (DAQ) with corresponding electronics. The self triggering capability is the new feature of Fermi-LAT design. The DAQ system with help of a programmable trigger software utilizes strong signals from ACD, tracker and calorimeter to form a trigger which in turn is fed back to DAQ and initiates the read out of different subsystems. Another feature is that all LAT detectors are made of non consumable materials.

The tracker system is modular, with 16 towers distributed in a 4×4 array. Each module has 18 tracking planes with two layers (x and y) of single-sided silicon strip detector. The first 16 tracker planes are interleaved with high Z converter foil (tungsten) as discussed previously. The first 12 converter foils are of less thickness ($0.03X_0$) which minimizes the Coulomb scattering for low energy photons. The rest of the converter layers are of higher thickness ($0.18X_0$) which provide more conversion probability for high energy photons. The arrangement of placing tracking detector very close to thin converter foil increases the LAT point spread function at low energy range. The optimized value of height-width ratio (0.4) of LAT tracker provides large field of view (FoV) of 2.4 sr and ensures almost all detected charge particles of tracker passes through the calorimeter. The detailed description is found in [91]

The ACD shield of LAT consists of 89 individual scintillator tiles and 8 scintillator fibers to cover the gap between tiles. The segmented ACD highly reduces the chance of producing false rejection signal due to recoiling electrons from calorimeter (self-veto effect). For charge particle detection, only tiles in the direction of incoming photon need to be examined. The scintillation light from each tiles is collected through photomultiplier tubes (PMTs) and fed into self triggering system. For detailed description, please refers to [92]

The LAT calorimeter serves two purposes i.e. measure the total energy deposited due to the electromagnetic particle shower initiated by incoming γ-photon and reconstruct shower development profile which helps in background rejection. The calorimeter modules are also arranged in 4×4 array as tracker. Each calorimeter module uses CsI (T1) crystals which are arranged in 8 horizontal layers, having total depth of 8.6 radiation lengths. The crystals in consecutive layers are perpendicularly (90^0) aligned to form a hodoscopic array. This structure allows to measure the shower development profile. The hodoscopic structure of calorimeter helps to enhance LAT upper energy threshold upto hundreds of GeV. For further details refer to [93, 94]

The special design of Fermi LAT provides a large effective area of 9500 cm^2 with better than 15% energy resolution over its full energy spectrum. The single photon angular resolution along the Z axis is less than 0.15^0. The fast electronics helps LAT to achieve fine time accuracy of < 10 μs and a short event dead time of 26.5 μs. The scanning operation mode with combination of large effective area and a huge field of view has allowed LAT to produce a detailed catalog of galactic and extra-galactic sources. The third Fermi source catalog (3FGL [95]) describes the spectral characteristics of more than 3000 sources with $> 4\sigma$ confidence. Out of these sources, at least 1000 sources are explored for the first time ever and have no counter parts in other wavelengths.

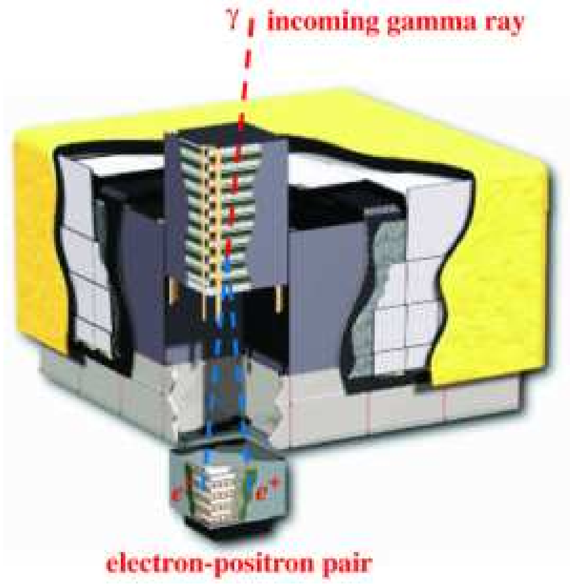

Figure 2.3: Basic structural diagram of Fermi Gamma-ray Space Telescope. This picture is taken from: [https://www-glast.stanford.edu]

Limitation of direct detection method

The design of any satellite detector, like Fermi-LAT, must follow the realities of rocket launching and operating in space. The weight and size of payload (i.e. space detector) are constrained by the capability of launching vehicle. Thus effective collection area and height-width ratio of tracker-calorimeter of space based satellite can not be enhanced after a certain limit. The sharply falling nature of cosmic gamma spectrum requires larger collection area at higher energy regime. On the other hand, a precise energy measurement of high energy photon is constrained by the size of the calorimeter. In direct detection technique, a very low detection probability beyond a certain energy limit ($\sim$ 100 GeV) produces statistically unreliable results. This causes direct detection method ineffective for energies above hundreds of GeV and some indirect methods play an crucial role in that regime.

Detection of VHE γ-photons with Imaging Air Cherenkov method

For the detection of VHE γ-photon, Imaging Air Cherenkov (IAC) technique has been established to be the most successful indirect method. In IAC technique, earth's atmosphere is itself treated as a giant calorimeter which, after incoming photon interaction, produces secondary charged particles and photons. Large optical mirrors with suitable focusing arrangement are deployed to image the Cherenkov emission of ultra relativistic charged particles and subsequently some sophisticated analysis methods are used to extract physical informations.

Development of extensive air showers (EASs)

The EAS is a cascade of particles which is initiated by the interaction of a single primary particle (either photon or cosmic charged particle) with atmospheric nucleus at the upper atmosphere level ($>$ 15 km). This interaction produces a number of secondary particles which again interact with atmospheric nucleus and generate a shower of particles. This is known as extensive air shower (EAS). At initial stage, the rate of particle production will be much more compared to decay rate. With increasing number of shower particles, energy per particle decreases which slows down particle production rate compared to decay rate and shower starts to die out. The development of γ-ray and hadron induced showers are briefly described below.

Gamma-ray initiated EAS

The γ-initiated EAS is started when an energetic photon enters into atmosphere and produce electron-positron pair in the presence of Coulomb field of an atmospheric nucleus ($\gamma \rightarrow e^+ + e^-$). The heavy mass of muon drastically lowered $\mu^\pm$ production cross section compared to $e^{\pm}$ production. These particles with sufficient energy again interact with nucleus and generate photons in bremsstrahlung process [see in *chapter 1*] ($e^{\pm} \rightarrow e^{\pm} + \gamma$). These processes repeat and increase the number of $e^{\pm}$s and γ-photons [fig. 2.4]. Thus the shower develops longitudinally along the trajectory of primary particle (i.e shower axis). The multiple scatterings between $e^{+} - e^{-}$ force particles to move away from shower axis and produces the lateral development of the shower. The production of secondary particles continues until the average energy of individual product particles falls below the threshold energy ($E_c \approx 83$ MeV) of bremsstrahlung process in air. At this stage, ionization losses become the dominant interaction process and the shower starts to gradually die out. So shower develops to it's maximum when average energy per particle is nearly $\sim E_c$. Since electromagnetic interactions are the only interaction responsible for development of γ-induced EAS, this is also known as electromagnetic (EM) shower.

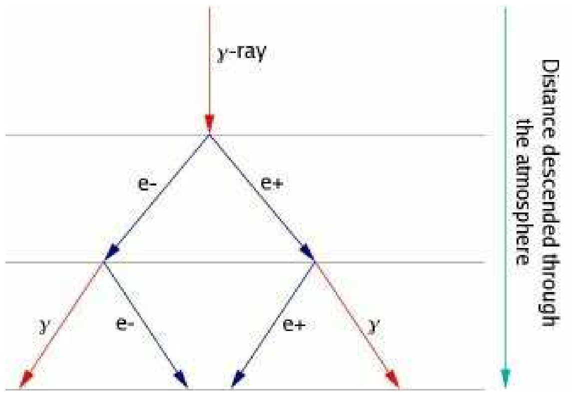

Figure 2.4: Air shower initiated by gamma photon. This picture has been taken from: [https://www.dur.ac.uk/cfai]

Hadron initiated EAS

The hadron initiated EAS is triggered by the interaction of energetic cosmic particles (mainly protons) with atmospheric nucleus. This interaction produce mainly pions, kaons and nucleons. The secondary hadrons, with sufficient energy, continue nuclear interaction to multiply the number of product particles until average energy per particle goes below a minimum value for nuclear interaction (i.e. ~ 1 GeV). In the later stage, ionization losses become dominant over particle production rate and the shower starts decaying. In hadronic interaction, almost 90% of all secondary particles are pions and one third of these are neutral pions (π^0) which almost decay into two identical photons (with branching ratio of 99%) [see in *chapter 1*]. Other secondary particles charged pions and kaons are generally decayed into muons and neutrinos. The decay channels are

$$\begin{aligned} \pi^{\pm} &\rightarrow \mu^{\pm} + \nu_{\mu}(\bar{\nu}_{\mu}) & & (\tau = 2.6 \times 10^{-8}\ \mathrm{s})\ , \\ K^{\pm} &\rightarrow \mu^{\pm} + \nu_{\mu}(\bar{\nu}_{\mu}) \quad & (\mathrm{B.R.}\ 63.4\%) \quad & (\tau = 1.2 \times 10^{-8}\ \mathrm{s})\ , \\ &\rightarrow \pi^{\pm} + \pi^{0} & (\mathrm{B.R.}\ 21.1\%) & \end{aligned}$$

The helicity conservation does not allow $e^{\pm}$ and ν_e production from the decay of charged kaons and pions.

Each energetic gamma photon from π^0 decay produces gamma induced EAS as a part of a hadron shower. Thus hadron induced shower, at it's most developed stage, contains mostly $e^{\pm}$, $\mu^{\pm}$, neutrinos and γ-photons. The nuclear interaction length for hadrons in air medium are sufficiently large compared pair production and bremsstrahlung process and this implies large longitudinal development scale of hadron shower. Large transverse momentum transfers in hadronic interaction spread secondary particles over a large area perpendicular to shower axis. Thus transverse development is more chaotic and irregular than EM shower. The main three parts of a hadron shower: the core of hadron interaction, electromagnetic sub shower and less interacting muonic part, are shown in fig. [2.5].

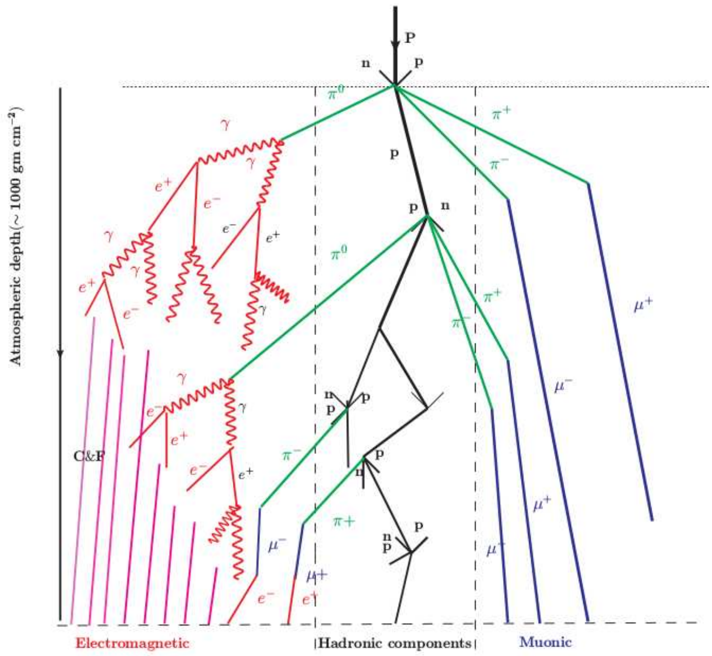

Figure 2.5: Air shower initiated by a cosmic particle

Cherenkov radiation by extensive air showers

When a charged particle travels inside a dielectric medium with a velocity greater than the velocity of light in that medium, the dielectric molecules emit photons of special characteristics which is known as Cherenkov radiation. This phenomena was first observed by Marie Curie in the year 1910 as a bluish light when she worked with radium salt but wrongly identified as luminescence. In years from 1934 to 1937, Cherenkov and Vavilov performed a series of experiments to study the nature and origin of this radiation. P. A. Cherenkov first discovered the anisotropic nature of this radiation and showed that photons are only emitted in a certain angular region around the particle trajectory [96]. The theoretical explanation was later given by I. E. Tamm and I. M. Frank in 1937 [97]. This emission can be understood as a combined effect of polarized medium. When a charged particle moves inside a dielectric medium, it polarizes nearby molecules around it's instantaneous position which results an induced dipole moment to each molecules. For particle velocity

$v < c_0$, velocity of light in that medium, the distribution of these tiny dipoles with respect to particle position are symmetric[fig. 2.6(a)]. Thus the net induced dipole moment at a large distance should be zero (no radiation is observed). But for superluminal particle velocity ($v > c_0$), the distributions of tiny induced dipoles in any plane, containing particle trajectory, are no longer symmetric which results in a non zero fluctuation in induced electric field at large distance[fig. 2.6(b)]. This is observed as pulse of Cherenkov radiation. The distribution of induced dipoles forms a conical shape around the particle trajectory which reinforces electric field to interfere constructively only at a particular angle. This implies the anisotropic nature of Cherenkov radiation. Huygens principle shows that the constructed wavefront can only propagate within a fixed angle θ_0 with respect to the velocity vector[fig. 2.6(c)] and this is given by

$$\cos\theta = \frac{1}{(\beta n)} \tag{2.1}$$

where $\beta = v/c$ and n is the refractive index of that medium. The equation [2.1]

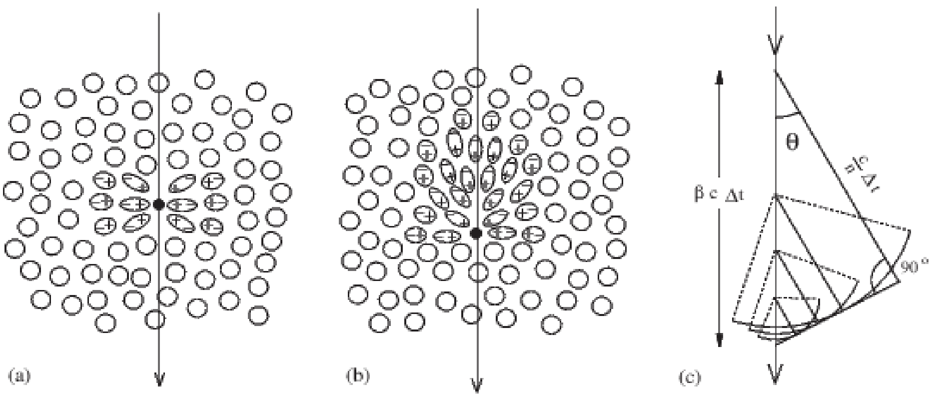

Figure 2.6: Polarization produced by charged particle in an dielectric medium: a) for low velocity ($v < c_0$) b) for superluminal velocity ($v > c_0$) c) The constructive interference of induced electric field at a particular direction

provides two conditions about Cherenkov radiation. Firstly, it gives a minimum value of β for producing Cherenkov radiation i.e. $\beta_{min} = 1/n$. This implies that no Cherenkov radiation will be observed for particle velocity less than $\beta_{min}c$. Thus minimum threshold energy for Cherenkov radiation is given by

$$E_{min} = \frac{m_0 c^2}{\sqrt{1 - {\beta_{min}}^2}} \tag{2.2}$$

where m_0 is the rest mass of the particle. Secondly for ultrarelativistic particle ($\beta \sim 1$), the maximum Cherenkov emission angle is given by

$$\cos\theta_{max} \simeq 1/n \tag{2.3}$$

Calculation of threshold Cherenkov energy and maximum emission angle at different height above sea level requires suitable model for atmospheric refractive index and a commonly used model is given by [98]

$$n = 1 + \eta_h = 1 + \eta_0 . exp(-\frac{h}{h_0}) \tag{2.4}$$

where $\eta_0 = 2.9 \times 10^{-4}$ and h_0 is 7.1 km. This simplified model does not include the frequency dependence of air refractive index which is very small. Beside that, a decreasing trend of air temperature with height is also neglected in this model which minutely affects atmospheric refractive index. Finally here we only consider showers of vertically downward particles. For large zenith angle, the effect of elongated atmospheric depth should be considered.

Assuming $\eta_h \ll 1$ and using equ. [2.2], [2.3] and [2.4], the minimum threshold energy and maximum emission angle as a function of altitude is given as

$$E_{min}(h) \simeq \frac{m_0 c^2}{\sqrt{2\eta_h}} \qquad \text{and} \quad \theta_{max}(h) \simeq \sqrt{2\eta_h} \text{ in radian} \tag{2.5}$$

It is important to notice that with increasing emission height h, E_{min} for Cherenkov emission increases. This is depicted in fig. [2.7(a)]. On the other hand, exponential nature of η_h with h implies small emission angle at higher altitude. The value of

$\theta_{max}(h)$ helps to calculate the distance of emitted Cherenkov photons from charge particle trajectory at a particular observation height h_{obs} and given by

$$R_c(h) = (h - h_{obs}) \tan \theta_{max}(h) \tag{2.6}$$

The fig. [2.7(b)(c)] represent the variation of R_c as a function of h for two different observation heights; one is for $h_{obs} = 2200$ m (height at which MAGIC telescopes are located) and other for sea level (i.e $h_{obs} = 0$ m). The plot shows that initially R_c increases linearly with h. The effect of θ_{max} starts to be dominating above 15 km and produce a steady decrease in R_c. The most interesting point is that a combined effect of h and θ_{max} reinforces all emitted Cherenkov photons between 20 to 10 km altitude to gather over a annular region of width $\sim$ 20 m (i.e within $R_c = 90$ m and $R_c = 110$ m) for $h_{obs} = 2200$ m. The fig.[2.8] shows schematically how Cherenkov photons, emitted at different height, reaches at almost same position on ground. This is the main reason to produce a clear peak in radial Cherenkov light density distribution and form a narrow bright Cherenkov enhancement ring around the primary photon trajectory at $R_c \sim 100$ m. The Coulomb scattering in EM shower which disperse electrons from shower axis and presence of earth's magnetic field produce some distortion in above mentioned ring pattern. The distortion is comparatively small for showers produced high in the atmosphere.

Figure [2.9] shows radial Cherenkov light density distribution of two simulated showers; one for γ-photon of energy 100 GeV and other for proton of 400 GeV. The characteristic hump structure (around $\sim$ 100 m) in lateral Cherenkov photon distribution is clearly evident in γ-initiated shower. The high transverse momentum transfer in hadronic interactions increases the dispersion of $e^{\pm}$ which completely erases the hump pattern in hadron initiated shower.

Impact parameter is an important quantity for description of EAS and defined as the perpendicular distance of shower axis from telescope location. The wide spread

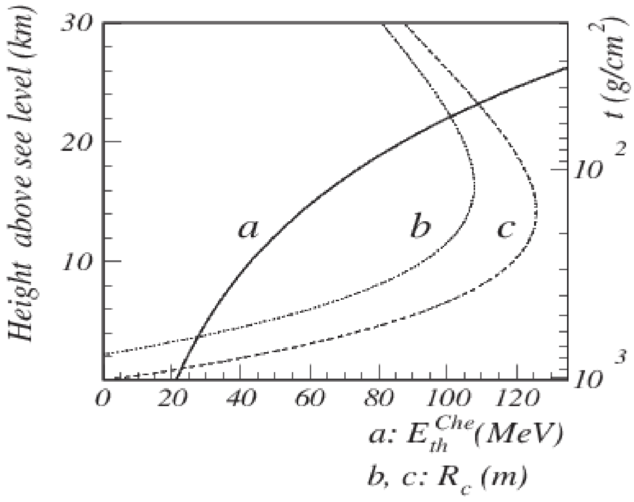

Figure 2.7: a) Plot of E_{min} with h; Plot of R_c as a function of h: b) for $h_{obs} = 2200$ m, c) for $h_{obs} = 0$ m; The figure is taken from [14].

of Cherenkov light pool allows us to detect EAS over a large extent of the impact parameters and this increases the effective collection area of IAC technique.

In atmospheric Cherenkov radiation, the radiated energy per atmospheric depth ($\chi = \int \rho_{air}(h)dh$) by an ultra relativistic electron ($\beta = 1$) in a wavelength interval between λ_1 and λ_2 is given by [99]

$$\frac{dE}{d\chi} = 4\pi^2 e^2 \ \frac{\eta_h}{\rho_{air}(h)}(\frac{1}{{\lambda_1}^2} - \frac{1}{{\lambda_2}^2}) \tag{2.7}$$

where $\rho_{air}(h)$ is the air density profile and considered as

$$\rho_{air}(h) = \rho_0 \ exp(-\frac{h}{h_0}) \quad \rho_0 = 0.0013 \text{ g/cm}^3 \text{ at see level} \tag{2.8}$$

Using equation [2.4] and [2.8], it can be shown that $\frac{dE}{d\chi}$ is independent of atmospheric height h i.e. constant through out the trajectory of charge particle. The wavelength band of observed Cherenkov emission is constrained by the atmospheric absorption and scattering phenomenas. The ozone layer absorbs all radiations of wavelength below 290 nm which fix the lower wavelength λ_1. The upper wavelength λ_2 is

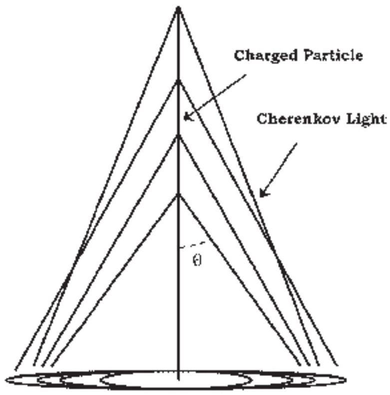

Figure 2.8: Pictoral presentation of Cherenkov ring formation. Figure is taken from [14]

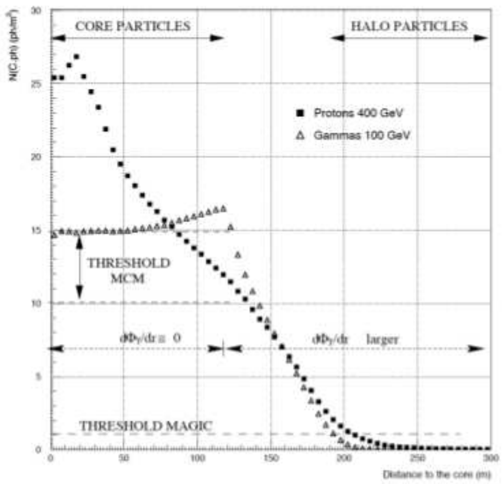

Figure 2.9: Lateral distribution of Cherenkov photon density for a shower produced by a gamma ray of 100 GeV and a proton of 400 GeV. The plot is taken from [15]

chosen 600 nm based on detector efficiency. The radiated Cherenkov energy per unit length in $\lambda_1 - \lambda_2$ band is $dE/d\chi = 1.1\ KeV.(g/cm^2)^{-1}$. The energy loss rate due to ionization in air is almost independent of altitude and given by $dE_{ion}/d\chi \sim 2.0\ MeV.(g/cm^2)^{-1}$ [54]. Thus the ratio of Cherenkov and ionization energy loss rate is constant ($\sim 5.10^{-4}$) upto first order approximation. This correlation gives a good estimation of total ionization energy loss, and consequently the energy of primary particle, in terms of observed Cherenkov photons energy.

It is convenient to express equ.[2.7] in terms to photon number and that gives

$$\frac{dN}{d\chi} = 4\pi\alpha \; \frac{\eta_h}{\rho_{air}(h)}(\frac{1}{\lambda_1} - \frac{1}{\lambda_2}) \tag{2.9}$$

where $\alpha = 1/137$ is the fine structure constant. In wavelength range $290 - 600$ nm, the radiated photon number per atmospheric depth is $360.(g/cm^2)^{-1}$. The important fact is that the number of radiated photons per atmospheric depth per wavelength i.e. $d^2N/d\chi d\lambda$ is proportional to $1/\lambda^2$. Thus most of the radiated energy is emitted in short wavelength range i.e in bluish ultra-violet range.

The observed spectrum of Cherenkov radiation is not same as the emitted one due to Cherenkov photon interaction with air molecules. A brief description of different interactions are given below:

1. The absorption of ultraviolet radiation by ozone (O_3) layer. This creates a sharp lower cut off wavelength at $290nm$. This has been mentioned previously.

2. The Rayleigh scattering of Cherenkov photons by atmospheric molecules. The photons, having wavelength large compared to the dimension of polarizable air molecule, are attenuated by this process. The scattering cross section is proportional to λ^{-4}.

3. Mie scattering due to the presence of aerosol particles. When photon wavelength is comparable to the diameter of atmospheric particles, Mie scattering plays a important role. The spectral dependence of cross section is given by λ^{-a} where $1 \gtrsim a \gtrsim 1.5$.

The photon loss due to first two processes are well predictable and included in Monte-Carlo simulation of EAS. For clear sky condition Rayleigh scattering is dominant process. But in bad weather condition (i.e. in presence of dust particle, high humidity), Mie scattering is more effective. This effect is very much unpredictable due to highly fluctuating nature of the aerosol particle density over time. To account for the effect of Mie scattering, a separate instrument has been used which can measure the opacity of atmosphere as a function of time.

Basic Principle of imaging atmospheric technique

The main elements of an Imaging Atmospheric Cherenkov (IAC) telescope are straight forward and very much similar to other ground based telescopes like optical and radio. It consists of a large reflector which is deployed to collect photons over a wide region and focus onto the focal plane of the reflector. At the focal plane, one puts a camera which converts photons into electrical signal. The whole reflector-camera system is placed on a platform, which can rotate simultaneously about two perpendicular axes (i.e. alt-azimuth mount), to counter balance the diurnal rotational motion of earth. An IAC telescope collects the Cherenkov photons from ultra relativistic $e^{\pm}$ pairs which are the product of atmospheric EM shower initiated by primary γ-photons from potential sources. A single primary photon produces a bunch of $e^{\pm}$ pairs and this ensemble of $e^{\pm}$ pairs produces an uniform light illumination over an circular region of radius$\sim$ 120 m at observational level, 2 km above see level. This is called the Cherenkov light pool. The IAC telescope collects photons from a small part of this light pool and reconstructs complex image of EAS.

The huge energy loss rate of ionization compared to Cherenkov process ($dE_{ion}/d\chi \sim 2 \times 10^3(dE_{Chen}/d\chi)$) shortens Cherenkov photon emission time to ns scale. Thus EAS produces Cherenkov pulse of ns duration. This requirement of short duration pulse detection requires the IAC camera to have a very short time response ($\sim ns$) criteria. At present, almost all IAC telescopes (except FACT [100]) use Photo Multiplier Tube (PMT) as the detector of Cherenkov photon.

In a γ-initiated shower, the Cherenkov photon emission angle depends on the height of emission above sea level [2.5]. On the other hand, the multiple Coulomb scattering diverges $e^{\pm}$'s path away from shower axis. The combination of these effects produce a correlation between Cherenkov photon incidence angle on camera and emission height (h), accurate upto first order of h. Consequently a one to one correspondence between image position in pixelized camera and Cherekov emission region is established. For utrarelativistic electrons ($\beta \sim 1$), electron velocity is comparable to the Cherenkov photon velocity in air ($n \sim 1$). Thus photons emitted at higher altitude hit camera plane before ones emitted from lower altitude.

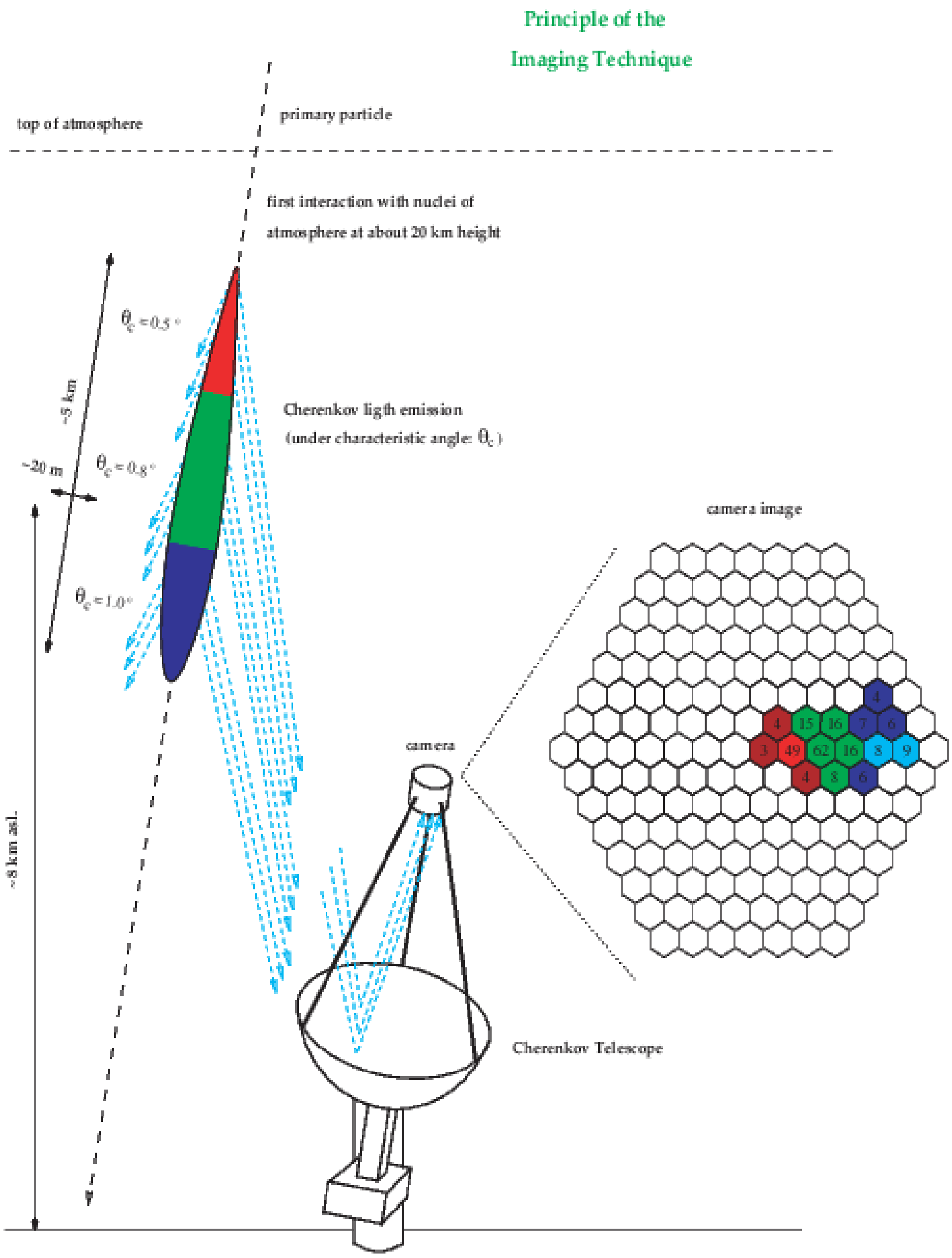

Figure 2.10: Graphical representation of EAS detection with a IAC telescope. This shower dimension is drawn for typically 1 TeV γ-photon. The number and color of each pixel represent detected Cherenkov photon number in that pixel and emission region of those photons in shower profile respectively. This picture is taken from [14]

The figure [2.10] schematically shows the formation of shower image which contains encrypted information of spatial and temporal evolution of the shower. This image can be used to infer shower informations like energy, direction etc. The total amount of light flux, i.e. size of the image, is used to estimate the energy of primary particle. The image shape and orientation in camera plane provide informations about incoming direction and types of primary particle.

Hillas parametrization

The imaging technique started with the parametrization of shower image. The technique forms a set of parameters which are specifically defined to describe the shape, size and orientation of a pixelized shower image. The noble idea of image parametrization was first introduced by A. M. Hillas in 1985 [101]. The parametrization process provides IAC technique an efficient tool to reconstruct EAS by characterizing shower image in terms of Hillas parameters. The energy, direction and other informations can be estimated from the measured values of Hillas parameters. Hillas algorithm also radically improved the γ-hadron separation capability of IAC technique (described in sec. *γ/hadron separation*).Using this technique, the Whipple telescope, first ever in history of TeV astronomy, was successfully able to detect TeV γ-rays from the Crab Nebula in 1989 [49].

The Hillas parametrization basically represents a weighted analysis of the recorded pixel signal amplitudes, where weights are defined as the strength of recorded signal in each pixel. The definition and interpretation of some useful parameters are given below and shown in figure [2.11]:

1. **Size**: The total amount of photons in the image. The total photon number is proportional to the energy of the primary particle.

2. **Length**: The rms spread of light along the major axis of the image. This a

measure of the vertical development of the cascade.

3. **Width**: The rms spread of light along the minor axis of the image. This represents the projection of lateral development of shower.

4. **Conc(N)**: Fraction of the image charge contained in the N brightest pixels. It gives the compactness of the image, which for EM shower is larger than for hadronic showers.

5. **Distance**: The distance from the centroid of the image to the center of the field of view of the camera. This is related to the impact parameter of the shower.

6. **Miss**: The perpendicular distance between the major axis of the image and the center of the field of view of the camera. This gives the estimation of the shower orientation.

7. **Alpha**: The angle between the major axis of the image and the line drawn from the center of the camera to the centroid of the image.

8. **Time RMS**: RMS of the arrival time of the surviving pixels, which is smaller for γ-induce cascades.

9. **Time gradient**: Slope of the linear fit applied to the arrival time projection along the major axis, which gives the direction of the shower development. γ showers are expected to have positive development.

10. **Disp**: The distance of reconstructed source position along major axis from the image centroid.

Data analysis of present generation IAC telescope involves some other sophisticated Hillas parameters which can be derived from these basic ones (described later in MAGIC data analysis section). For more detailed derivation and calculation of Hillas parameter, refer to [16]

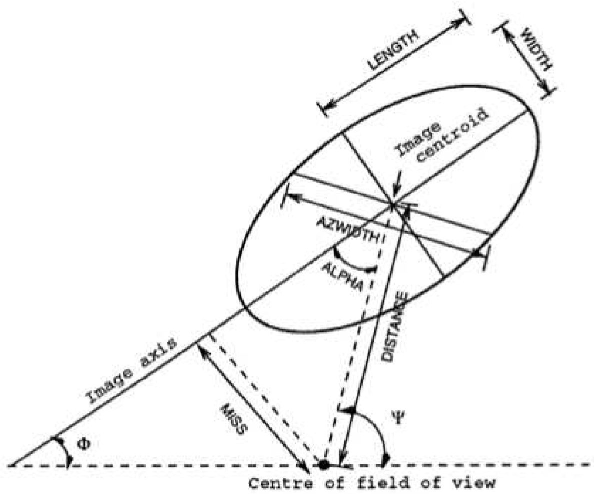

Figure 2.11: Characterization of shower image by Hillas parametrization. This figure is taken from [16]

Stereoscopic observation

In mid-90's, the imaging technique became more sophisticated with the use of multi telescope system for stereoscopic observation. In this mode, images from a single EAS are simultaneously recorded by multiple IAC telescopes. The proposal for stereoscopic observation was first suggested by Weekes and Turver in 1977 [102]. The use of stereoscopic observation allows a 3D shower reconstruction, including the development of the shower maximum (discussed in sec. *Magic data analysis*). Compared to single telescope observation, stereoscopic mode improves sensitivity, both energy and angular resolution of IAC telescope to a great extent. The coincidence trigger system of stereo observation is highly efficient to remove the muon background. Now a days, all the current generation IAC telescope system uses stereo observation mode.

Collection area and threshold energy

It is already mentioned that Cherenkov radiation from a single primary photon produces a circular light pool of radius $\sim 100\ m$ at observation level. This situation has two outcomes, described below.

The large spread of Cherenkov light pool provides an opportunity to detect showers over wide range of impact parameter which, in turn, results in an enormous collection area ($\sim 10^5\ m^2$) for IAC telescope. This increases the sensitivity of imaging technique over space based detector in VHE regime. The small collection area ($\sim 1\ m^2$) was the main constraint of satellite detector in detecting photons above $100\ GeV$. The 5 order of magnitude larger collection area offers IAC technique an opportunity to detect photons upto $\sim 50\ TeV$. It should be mentioned that collection area actually depends on energy and zenith angle i.e. incoming direction of primary photon.

The Cherenkov photon density, at a particular observation height, depends on type and energy of primary particle. The figure [2.12] shows variation of average photon density at observation height $h_{obs} = 2\ km$. For effective image parametrization, a minimum number of photons (i.e minimum value of size parameter) should be detected. Thus based on reflector size and detector sensitivity, there should be a minimum number of photons for a particular energy, below which no detection is possible. This gives the minimum detectable energy of IAC telescope.

For γ-photon of VHE regime, the average photon number in camera is proportional to the energy of primary particle. So the increase in light collection area (A_{ref}) and detector sensitivity decreases the threshold energy

$$E_{th} \propto \frac{1}{A_{ref}.LDE} \tag{2.10}$$

here LDE is the light detection efficiency which is determined by several factors

$$LDE = R \times LG_{eff} \times QE \times CE \tag{2.11}$$

where R is the reflectivity of mirror, LG_{eff} is light guide efficiency, QE is the quantum efficiency of photo cathode and CE is the collection efficiency of first dynodes of PMT.

The E_{th} does not give a sharp boundary due to photon number fluctuation in shower. So the community chose a definition and threshold energy is defined as the energy for which differential trigger rate is maximum. This definition requires a standard source spectrum for reference purpose. For northern hemisphere, The Crab nebula spectrum above 300 GeV is chosen as reference spectrum (discussed later in sec. *Energy resolution and threshold energy*).

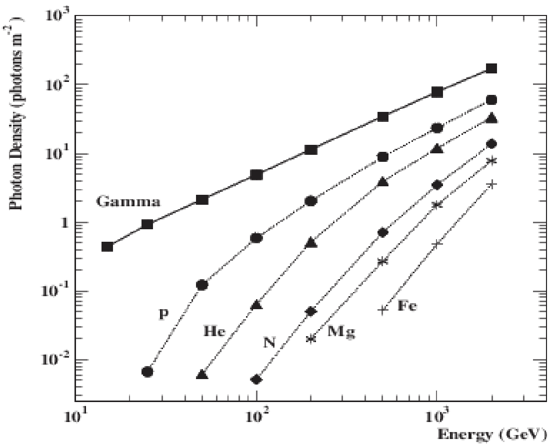

Figure 2.12: Variation of average photon density with type and energy of primary particle at an observational height of 2 km above sea level. The energy range of photon corresponds to $300 - 600$ nm. The photon density is averaged over an area of 50000 m^2. This figure is taken from [17]

Background in IAC technique and its rejection

It is previously shown that cosmic particles also induced EAS and almost one-third of it's energy is released in form of EM shower which is similar to γ induced shower. Thus the distinction between γ and cosmic induced shower is one of the main challenges of IAC technique. The cosmic particles that can mimic γ induced shower are hadrons, electrons and muons. In hadrons, proton and α-particle are the most abundant particle in cosmic flux. Less abundance [103] and lower amount of Cherenkov photon production compared to proton and α-particle shower make other heavier nuclei insignificant in background calculation [fig. 2.12]. Experiments shows that cosmic proton flux is 5 order of magnitude higher than γ flux (galactic and extra galactic) for energy above 30 GeV [104, 105].

Hadron background

Since longitudinal and lateral distribution of hadron showers are longer and wider than γ induced shower of same energy, the image of a hadron induced shower is more irregular and chaotic in nature, whereas the image of γ initiated shower is more compact and regular in shape. The figure [2.13] shows the development of gamma and hadron induced shower and real images of gamma and hadron event in IAC telescope camera. Thus compactness and regular shape of the shower image produce a clear distinction between gamma and hadron initiated shower which is implemented analytically via Hillas parametrization. Detailed Monte Carlo simulations are used to distinguish between the images that result from gamma-ray and cosmic ray initiated showers. Length and Width parameters of hadron initiated shower are larger than those produced by γ shower. Figure [2.14] shows the distributions of different Hillas parameters for gamma-ray and cosmic ray showers, and these indicate that the discrimination of cosmic ray events is possible on the basis of Hillas parameters [16].

An extra distinction criteria can be introduced by exploiting the fact that all γ events from a fixed source will have the same incident angle whereas the distribution of hadron events is isotropic in camera plane. Consequently all γ events have always same orientation (i.e. major axes will pass through source position on camera plane) whereas hadron events will be randomly distributed.

Due to the decay of neutral pion into two identical γ photons, hadron initiated shower always contains an electromagnetic sub shower at its most developed stage. These sub showers can mimic the EM shower, initiated by primary γ-photon, upto a high level of accuracy. Thus, in reality, complete γ/hadron separation never be possible and these hadron events form the irreducible background of IAC technique.

Muon background

The muons are mainly produced in hadronic showers as the decay products of charged pions and kions. Cosmic muons never reach lower atmosphere due to their short life time ($\tau = 2.2 \times 10^{-6}\ s$). The secondary muons, having sufficient energy to generate Cherenkov radiation, are produced in upper atmosphere. Due to very penetrating nature, some muons can reach up to detector level and contribute significantly to the background of IAC telescope. Muons with small impact factor will produce a characteristic ring in camera plane due to the short height of Cherenkov emission (fig. [2.15]). These are easily distinguishable from γ events. But the image of Cherenkov photons from muons of large impact parameter ($\gtrsim 60\ m$) can mimic γ event which are difficult to reject (fig. [2.16]). The analysis based on Hillas parameter can partly remove muon events [16,106]. But stereoscopic observation mode can suppress greatly muon background with the use of stereo trigger system [107].

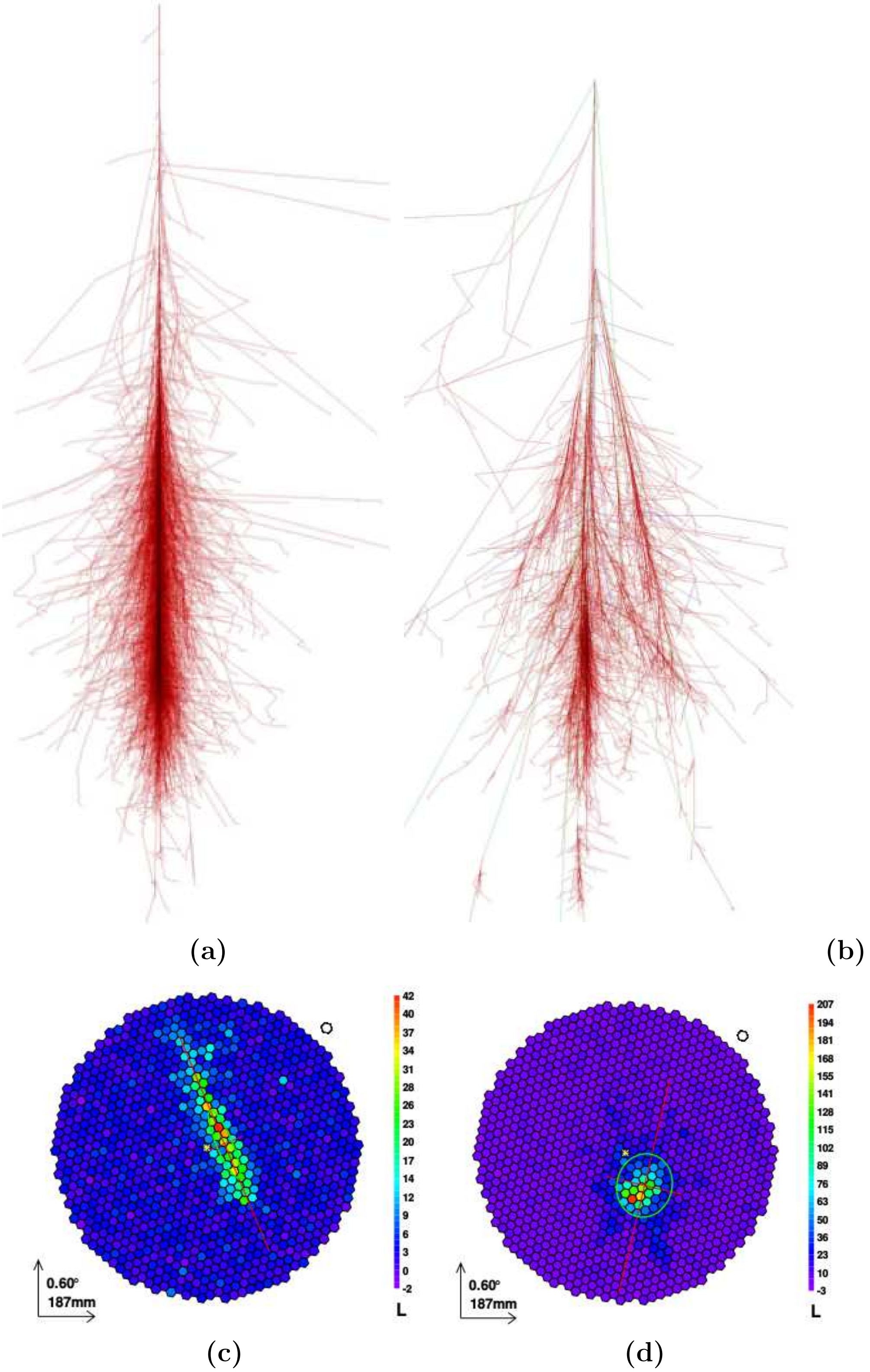

Figure 2.13: xz projections of simulated EAS induced by **(a)** a 100 GeV gamma-ray and **(b)** a 100 GeV proton, when projected along y axis. These shower images have been produced by F. Schmidt and J. Knapp at University of Leeds (2005); Images of air showers as recorded by a IACT camera (the examples are taken from real MAGIC-II data): **(c)** γ-ray candidate, **(d)** proton candidate event. The figures are taken from [18].

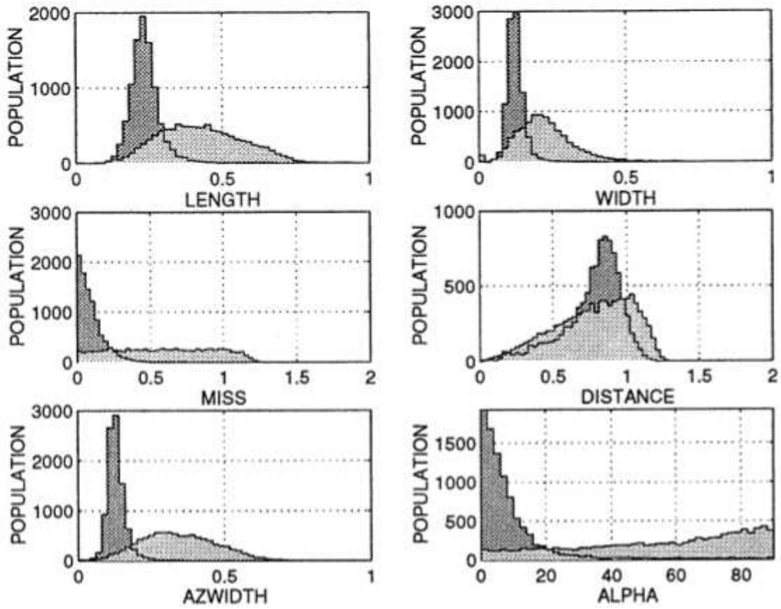

Figure 2.14: Typical parameter distributions for simulated γ-rays (dark) and real hadronic background (light) using the Whipple 10 m reflector. This figure is taken from [19]

Electron background

High energy cosmic electrons ($\gtrsim 5\ GeV$) interacting with atmosphere produce EAS which is completely similar to the γ events of same energy. This makes electron events very difficult to remove completely. The only parameter in single telescope observation, which can be used to reject electron events, is the incident direction or orientation of shower image. The electron events are isotropically distributed in focal plane whereas major axes of γ-events are always pointed towards the source position. This feature allows one to decrease electron background by a factor of ~ 10 for point-like source observation. In stereoscopic observation, the height of shower maximum is extensively used to remove the cosmic electron background.

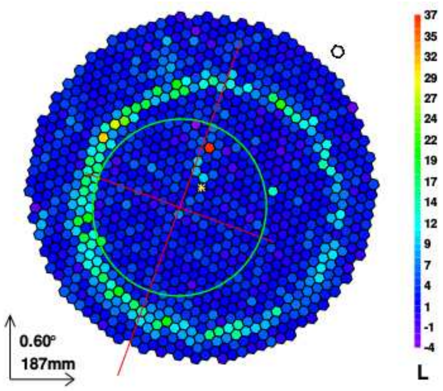

Figure 2.15: Images of air showers as recorded by a IACT camera (the examples are taken from real MAGIC-II data). This figure is taken from [18].

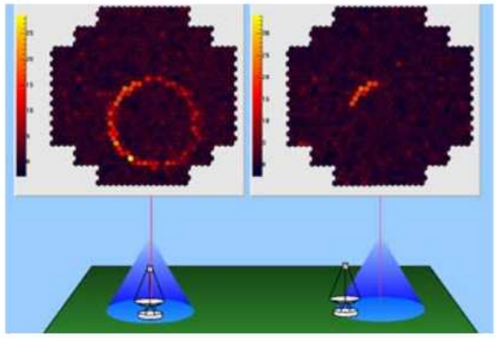

Figure 2.16: Local muons hitting telescopes in the center and close to the periphery. The figure is taken from [20]

Night sky background (NSB)

Most of Cherenkov energy is emitted in short wavelength range which overlaps with the blue end of visible spectrum. This can distort the image formation [108] and can produce artificial triggers. Thus Light Of Night Sky (LONS) forms a constant background for IAC technique. This has mainly two components; one is diffuse and other is non diffuse component. Diffuse component mainly comes from scattered sunlight of interplanetary dust and deexcitation of atoms in upper atmosphere. The scattered star light in interplanetary dust also plays a role in LONS. This creates an isotropic background. The non diffuse component of LONS primarily comes from the presence of bright star within the field of view of particular source. The presence of strong moon light can also affect non diffuse component of LONS. The presence of LONS significantly affects low energy shower detection near threshold energy (E_{th}). The effect of diffuse component can be reduced partially in two steps; firstly by raising the threshold energy followed by requiring a multi-fold next neighbour coincidence of nearby pixels within a short coincidence time. The effect of a bright star within field of view is controlled by replacing the count of illuminated pixels (i.e. average DC current) with the normal one.

MAGIC telescope system

The Florian Goebel Major Atmospheric Gamma-ray Imaging Cherenkov (MAGIC) telescopes, named after Florian Goebel (1972 – 2008), are a stereoscopic IAC system of two 17 m diameter mirrors situated at La Palma of Canary island, Spain (2225 m a.s.l.). This is specially designed to achieve the lowest possible threshold energy. MAGIC I and MAGIC II started their operation from 2004 and 2009 respectively. Between summer 2011 and 2012 both telescopes underwent a major upgrade that involved the digital trigger, readout systems and the MAGIC I camera [109]. After this upgrade, the system achieves an integral sensitivity of $0.66 \pm 0.03\%$ of the Crab Nebula flux in 50 hours above 220 GeV [5]. The data presented in this thesis was taken only in stereoscopic mode.

Figure 2.17: Picture of MAGIC stereoscopic system at La Palma, Spain. The Gran Telescopio Canarias (GranTeCan) is seen in the background. This image is taken from [https://magicold.mpp.mpg.de]

Hardware description

The main components of MAGIC hardware system are briefly described below:

Structure and Drive system: The telescope mount is alt-azimuthal. The dish structure, supporting the mirrors, can move in zenith direction over a range from -70^0 to 105^0 [22]. The dish frame is made of rigid and light weight carbon fibre-epoxy tube. The lower structure, made of steel, is placed over a rail and can rotate in azimuth angle from -90^0 to 318^0. The deformation of dish structure, due to self weight, is less than 3.5 mm for any orientation [110]. The effect of deformation in focusing is minimized by Active Mirror Control (AMC) technique. For GRB observation, telescope can rotate 180^0 in $\sim$ 20 s. The telescope can track sources with an accuracy of 0.02^0.

Reflector and mirrors: The MAGIC mirrors are parabolic reflectors of diameter 17 m. The focal length is same as diameter ($f/D \sim 1$). The mirrors are isochronous which minimizes the broadening of ns Cherenkov pulse and reduces the noise integration. The mirror point spread function (PSF) is defined as the diameter of circular region on camera which contains 39% of total light from a point-like source; which is $\sim$ 10 mm region over on-axis camera plane. The total light collecting surface of both telescopes is $\sim$ 236 m^2. This surface is tessellated with 247 square shaped facets ($1m \times 1m$) and the orientation of each of these facets are controlled by AMC software. The AMC, as a part of hardware, is responsible for correcting mirror focusing at different zenith angle due to the deformation of the telescope. The system has two actuators per facet which can adjust their position up to an accuracy of 20 μm. This system maximizes the focusing power to achieve an PSF of $\sim 0.037^0$ ($\sim$ 11 mm), very close to theoretical value.

Camera: The MAGIC cameras are made of PMTs which are arranged over an circular region of diameter 1.2 m. Each camera consists of 1039 PMTs, known as pixels. Each of the PMTs is equipped with a light guide, called Winston cone, that increases the light detection efficiency (LDE).The camera field of view (FoV) is 3.5^0 and FoV per PMT is 0.1^0. The system also contains the power supply, cooling arrangement. The PMTs (Hamamatsu R10408) are specially designed for fast response ($\sim 3\ ns$) and high quantum efficiency (34% at 350 nm) [111]. The HV supply, typically 1250 V, is taken from a Cockroft-Walton type DC-DC converter. This HV is maintained to achieve low gain of PMTs ($\sim 3\times10^4$) which help to extend observation during moon light conditions. The analog electronic signal from PMTs are converted into optical signal by vertical cavity surface emitting lasers (VCSELs) and transmitted to receiver board in counting house through a 162 m long optical fiber. The whole camera system is covered by metalic sheild with movable lids which protect it from bad weather conditions.

Calibration system: Good quality data collection and efficient analysis requires proper calibration of the camera i.e. equalization of PMT gain throughout the camera and exact determination of conversion factor of Flash Analog-to-Digital Converter (FADC) counts correspond to a single photon. MAGIC calibration system consist of a Nd-YAG laser, operating at 355 nm with 0.7 ns pulse width. To obtain a dynamic range of signal strength, different attenuator are used. To achieve the homogeneous distribution of calibration light a diffuser is used. The system is placed at center of each mirror dish.

Trigger system: At the end of the optical fiber, the signal is again converted into electrical signal and and divided in two parts. one goes into trigger system and other into readout system. The function of trigger system is to discriminate the γ-induced signal from NSB. This process consists of three stages [112].

Level 0 **(L**0**)** : Signals from individual pixels go through the discriminators with a given threshold, so called discriminator threshold (DT). Every time signal from pixels overpasses DT, it issues a square signal of adjustable width. The height of DT depends on moonlight strength. It is more relaxed for dark night observation and more conservative higher the NSB becomes.

Level 1 **(L**1**)** : It is a digital filtration to find the spatial and temporal coincidence of all pixels that pass the L0 trigger. Camera pixels are grouped in 19 hexagonal overlapping cells (containing 37 pixels) called macrocells which covers a region of $\sim 2.5^0$ diameter. If n neighboring pixels in any macrocell, defined as Next Neighbour (NN), contains a signal above the DT, the L1 trigger produces a signal. The possible values of n are 2, 3, 4, but in standard stereo mode, the optimized value 3NN criteria is chosen which provides a considerable trigger rate with a threshold energy well above the noise level. The signals from each macrocell, fulfilling 3 NN criteria, is merged into a OR gate and proceed for next level.

Level 3 **(L**3**)** : This trigger level only applies for stereo observations. It receives the output of the L1 trigger from both telescopes and stretches them artificially to achieve 100 ns width. It finds an effective overlap between the corresponding stretched signals of both telescopes within a time span of $\sim$ 180 ns. The acceptance of L3 trigger starts the readout system.

Readout: The readout system digitizes and temporarily stores the analogue signals from the telescope. Currently MAGIC readout system is equipped with Domino Ring Sampler version 4 (DRS4) [113] analog memory chip. It has a very short dead time of 27 μs. It is characterized with large bandwidth of 700 MHz and a lower pedestal noise (0.7 phe per cell). The upgraded MAGIC readout is sampling the signals with a rate of 2 Gsamples/s [109]. The main disadvantage of DRS4 chip is the output's temperature dependency and need to be calibrated at regular intervals.

Observation and data taking

The standard observation and best performance of MAGIC is achieved in dark condition (i.e. with cloudless moonless nights). Total available observation time in dark condition (excluding bad weather condition and technical problems) is $\sim 65\%$ of $\sim$ 1600 hrs/yr. Observation in low and moderate moon condition (except full moon condition) can increase MAGIC duty cycle by a large amount. This requires some modifications in hardware system (addition of moon filter) which minimizes the effect of bright background. The presence of moon increases the NSB which again proportionately affects the value of median pixel DC (PMT anode current). Thus pixel median DC value is the measure of NSB and for reference purpose, the average median DC of MAGIC I camera is chosen when telescopes pointing towards the Crab Nebula at low zenith angle, with no Moon in the sky or near the horizon in good weather condition. This background condition is referred as NSB_{dark} which corresponds to 1.1 μA median DC. The higher NSB level increases the noise of recorded image which is proportional to $\sqrt{\mathrm{NSB}}$ (considering Poisson distribution of NSB). The higher noise level degrades the image quality of low energy showers. To suppress this effect, stronger image cleaning cuts are applied during the data analysis. With the standard HV, MAGIC can perform against maximum sky brightness of $8 \times \mathrm{NSB}_{dark}$. By reducing the HV value by a factor of 1.7 (reduced HV), MAGIC can operate up to $20 \times \mathrm{NSB}_{dark}$ without affecting the safety of the camera during the data taking.

Different types of data are taken with MAGIC during data taking. First one is **pedestal subtraction run** which is used to calibrate the base line of DRS4 capacitors. Second is **pedestal run** which records only randomly triggered noise events and this is used to evaluate the effect of the NSB and readout noise (which need to be subtracted from calibrated data). The **calibration run**, containing triggered events from calibration system, is used to estimate FADC conversion factor. The **data run** contains all events from telescope that issued valid triggers and used in standard data analysis.

The standard observation mode of MAGIC is stereo pointing mode. MAGIC generally uses two types of pointing modes.

ON-OFF mode: In this mode, the source is tracked by keeping it's position fixed at the center of the camera FoV. This is called ON source observation. For background estimation, telescope is focused towards some other part of sky (with same epoch, zenith angle and atmospheric conditions) where no gamma source is expected. This is called OFF source observation which is required for significance calculation.

Wobble mode: In this mode, telescope points slightly away from the actual source position to estimate background simultaneously with source observation [114]. Thus source position in camera is at a slight offset from camera center. The choice of small offset can produce contamination of ON and OFF region which degrades background estimation. On the other hand, large offset strongly affects the camera detection efficiency. The choice of proper offset is an optimization of these two effects. This method increases the effective source observation time because there is no dedicated OFF source observation required. This method also preserves exactly the same condition for ON and OFF source data. For MAGIC the standard offset is chosen 0.4^0 and each position is observed during 20 minutes. If only one OFF position is selected, it is taken from the diametrically opposite position of the camera with respect to the camera center as it is shown in Figure [2.18(a)]. More than one simultaneous OFF positions are also possible, as can be seen in Figure [2.18(b)], which helps to estimation background more precisely. These pointing positions are called wobble positions which are chosen symmetrically around the source position which minimizes the inhomogeneities (if any) in camera field of view. Typically 2 or 4 wobble positions are chosen. Thus during observation, source moves, in camera plane, over a circle of radius 0.4^0 around center of FoV. The better background estimation can be achieved by averaging over three OFF positions. Thus standard MAGIC observation is performed with four wobble configuration. The main disadvantage of wobble mode is a small decrease in γ-detection efficiency. Due to the shift of source position towards the periphery of trigger region ($\sim 2.7^0$), some fraction of the EM cascades may lie outside of this region (this fraction is $\sim 15\% - 20\%$).

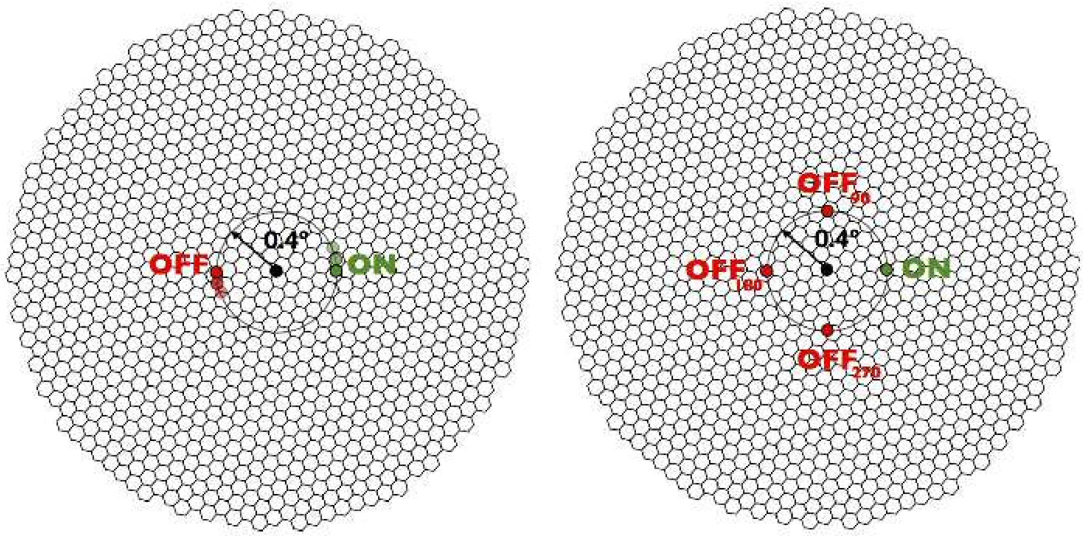

(a) Wobble mode with 1 OFF. **(b)** Wobble mode with 3 OFFs.

Figure 2.18: Schematic view of the wobble pointing mode. The black circle marks the center of the camera. A region placed 0.4^0 from the source is tracked, being the source all the time situated at this distance from the center of the camera (green circle). The simultaneous background is taken all the moment from a region situated in the opposite side of the circle with center in the center of the camera and radius 0.4^0 (red circle in the left figure) in the case of 1 OFF region. In the case of 3 or more OFF regions, the background is taken from regions separated the same distance from one another in the aforementioned circle as it is shown in the right figure. The subindex of the OFF regions determine the angle turned in the circle counted counterclockwise from the ON region. These figures are taken from [21].

Magic data analysis

MAGIC data analysis is performed with a dedicated custommade software, named MAGIC Analysis and Reconstruction Software (`MARS`) [115]. It starts with the raw data (FADC count stored in DAQ) and produces high level data using a bunch of programs written in C++ language. The main goal of data analysis is to separate γ induced events from hadron events and extract energy and direction informations of corresponding events. This process follows a long analysis chain [fig. 2.19] and important steps are briefly discussed here.

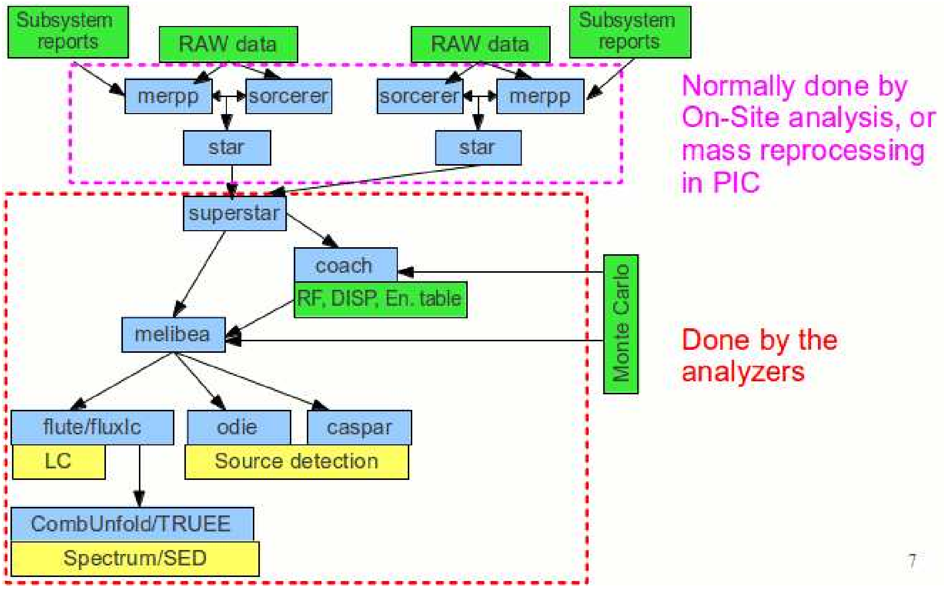

Figure 2.19: Scheme of standard MAGIC analysis chain. The flow chart is taken from [http://wiki.magic.pic.es]

Monte Carlo (MC) simulation

Due to the non availability of GeV/TeV gamma sources in the laboratory, one has to rely on MC simulations to estimate the energy and direction informations of the incoming event. In case of MAGIC, gamma events are simulated in two different ways, ringwobble and diffuse MC. Ringwobble MC simulates events over a ring of 0.4^0 radius (width 0.1^0) around the camera center. This MC is used to analyze point-like sources (whose data are taken with standard wobble mode). The diffuse MC is used for the analysis of extended sources or sources shifted from their nominal position. In diffuse MC, events are simulated over a circle of 1.5^0 radius. These are shown in fig. [2.20]. In both cases, different MCs are used for different zenith (zd) range i.e. low zd ($5^0 - 35^0$), medium zd ($35^0 - 50^0$), high zd ($50^0 - 62^0$) and very high zd ($62^0 - 70^0$). For more informations refer to [116].

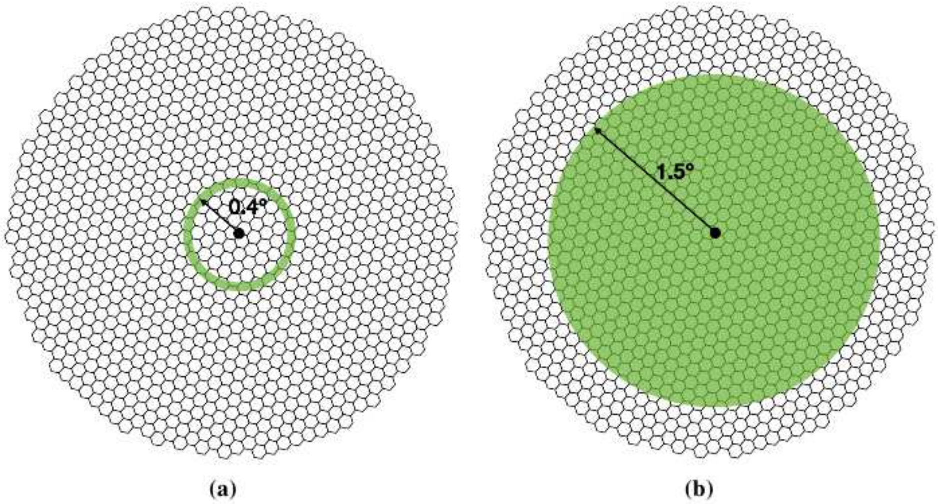

Figure 2.20: Ringwobble (left panel) and diffuse (right panel) MC schemes. The green shaded area is the one where the MC gamma rays are simulated. The images are taken from [21]

Signal extraction and calibration

The raw data i.e. output of the digitizer is converted to ROOT[1] format and merged with other subsystem data by a program called `merpp` (MERging and Preprocessing Program). This ROOT format data should be calibrated to convert FADC counts into number of phe. This is done by `sorcerer` (Simple, Outright Raw Calibration; Easy, Reliable Extraction Routines). The valid signal from each pixels are recorded over a 30 ns time window with a bin size of 0.5 ns. The pedestal data is used to estimate the baseline which is needed to be subtracted from the waveform. After pedestal subtraction, the signal is extracted using sliding window algorithm which integrates signal over 6 consecutive time bins and finds a position of integration time window which gives the largest signal. The signal arrival time is the weighted average position of the selected 6 bins. The FADC counts stored in each bin are used as the weight factor.

The F-factor method is used to convert the signal in terms of phe [117]. Let us consider a pulse with N phe which creates on an average a signal of μ FADC counts

[1] https://root.cern/

i.e. $\mu = N/C$ counts. where 1 FADC count corresponds to C phe. Assuming Poisson distribution of phe, the fluctuations in signal is given by $\sigma_{signal} = \sqrt{N}/C$ counts. Thus

$$N = (\frac{\mu}{\sigma_{signal}})^2 \text{ and } c = \frac{N}{\mu}$$

The noise due to electron multiplication in dynodes of PMT is non- Poissonian and requires a correction factor in signal fluctuation which is known as F-factor. The corrected formula, including the F-factor of PMT and fluctuation in pedestal data, is

$$C = \frac{N}{\mu} = F^2 \frac{\mu}{{\sigma_{signal}}^2 - {\sigma_{pedestal}}^2}$$

Image cleaning and Hillas parameterization

After signal extraction, each pixel contains charge and arrival time informations. But Most of them contain spurious data (NSB) and noise. Thus the goal of image cleaning process is to retain these pixels which contain signal from Cherenkov photons and remove others. The program called, `star`, performs the image cleaning and Hillas parametrization. Two types of image cleaning are explained here.

In absolute image cleaning method [118], only the charge (phe) contained in the pixels is used as criteria to keep or to reject the signal of a given pixel. This algorithm requires comparatively high threshold value (than RMS of dark NSB) to perform effective image cleaning. The use of high reference levels highly suppress the detection of low energy cascade which raises the threshold energy (E_{th}). On the other side, lower reference level allows noise induced image to overcome this threshold. The use of signal arrival time in image cleaning method helps to lower thresholds with less risk of accepting non gamma-ray events. In this algorithm, pixels, forming the image of EAS, are categorized in two distinct types: one is core pixel and other is boundary pixel. A pixel is regarded as a core pixel if the

NSB/NSB$_{dark}$	HV	Q_c (phe)	Q_b (phe)	Mean pedestal (phe)	RMS pedestal (phe)
$1-2$	Standard	6	3.5	-	-
$2-3$	Standard	7	4.5	3.0	1.3
$3-5$	Standard	8	5	3.5	1.4
$5-8$	Standard	9	5.5	4.1	1.7
$5-8$	Reduced	11	7	4.8	2
$8-12$	Reduced	13	8	5.8	2.3
$12-18$	Reduced	14	9	6.6	2.6

Table 2.1: The standard values of charge threshold for different moon light strength and corresponding noise levels used in standard MAGIC analysis.

corresponding phe is higher than a certain threshold Q_c, if the difference between pixel arrival time and the mean arrival time of the image core is less than Δt_c, and if it is adjacent to another core pixel. Boundary pixels are defined as the pixels with phe above a threshold Q_b, are adjacent to at least one core pixel and if their arrival time does not differ from the arrival time of that core pixel a time larger than Δt_b. The values of timing thresholds, used in MAGIC analysis, are $\Delta t_c = 4.5\ ns$, $\Delta t_b = 1.5\ ns$. These numbers have been estimated by performing detailed MC studies [119]

The value of charge thresholds depend on the level of moonlight. The corresponding values used in the image cleaning of the data are listed in table below. For proper analysis, both MC data and a real background data are required. For a particular observation, both of them need to mimic same observational conditions as those for original data. Thus for Moon analysis, MC and background data with same moonlight levels as that of actual observations, are required. The MC files are generally prepared for dark conditions. So before star operation, artificial noise should be added in MC files. In case of background sample, either artificial noise is added to dark data or data taken with same moonlight conditions are used. The noise level that has to be added is taken from the mean and RMS value of the so-called interleaved pedestal data. This values are given in table [2.1]. In this thesis, I have presented the analysis of both dark data and moon data (upto 8 times of NSB_{dark}) taken with standard HV settings.

After image cleaning, `star` calculates the value of different Hillas parameters for each event of both telescopes separately. The some useful parameters are already defined in sec. *Hillas parametrization*.

Calculation of stereo image parameters: After parametrization, the Hillas parameters of identical event from both telescopes are combined to calculate the stereo parameters. The program called `superstar` is used for this purpose. The definition of different stereo parameters is given below:

Shower axis: The shower axis can be obtained from the crossing of the extended major axes of the two images of the telescopes when they are projected into the one camera plane (fig. [2.21(c)]). This is the so-called *crossing point* method [120, 121]. This method cannot be used in mono observations.

Impact point: The point where the shower axis hit the ground. The point of intersection of the extended major axes of the shower image in each telescopes provides the information about impact point. The impact point calculation requires the coordinate of each telescopes.

Impact parameter: Perpendicular distance in the camera between the pointing direction and the shower axis. There is one impact parameter per telescope (fig. [2.21(a)]).

Shower maximum height (H_{max}): The height at which the number of particles in the shower reaches its maximum ($Hmax$). After shower axis determination, H_{max} is estimated with the help of the angle at which the center of gravity of image is viewed in each telescope. H_{max} is inversely proportional to the energy of primary particle. For same primary energy, H_{max} depends also on nature of primary particle i.e. gamma or hadron.

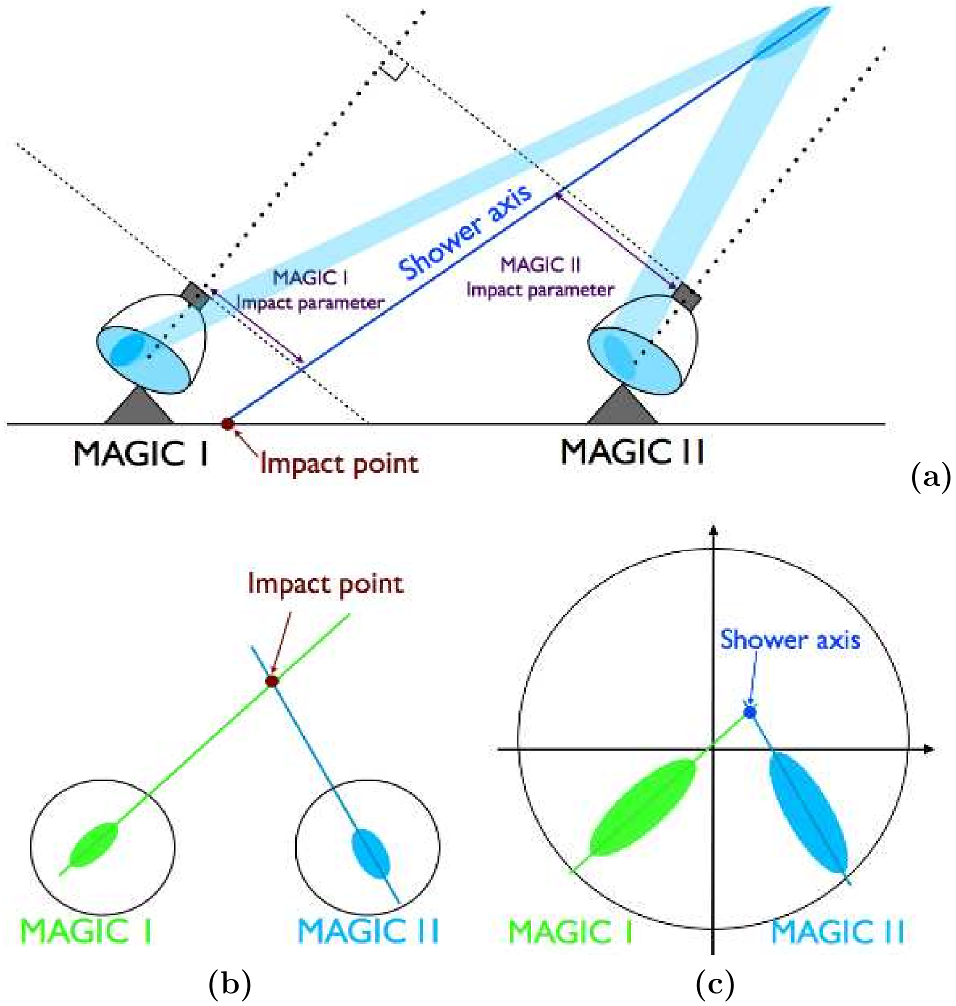

Figure 2.21: **(a)** Stereo event shower geometry; **(b)** Calculation scheme of the impact point on the ground. **(c)** Scheme of the shower direction determination. This picture is taken from [21]

γ/hadron separation

It is already mentioned that cosmic flux (mainly proton) is almost 3 order of magnitude higher than gamma flux at GeV regime and therefore discrimination of γ-events against this overwhelming background is the most important task of analysis. To perform this discrimination, a multi-dimensional classification algorithm based on decision trees, called Random Forest (RF) method is used [81]. In order to train the RF on how to distinguish the γ-events from the hadronic ones, the algorithm requires MC simulated gamma events and real background data (with no gamma emitter). In reality as the hadron flux is very intense compared to gamma, any sample of a non-detected source or a weak one is also suitable to train the RF. both MC gamma and real background data need to mimic the observational conditions (i.e. zd range, NSB strength and weather condition) under which the source is observed. The MC sample, used to teach the RF, called *train* sample is different from the *test* sample, used later in analysis to estimate collection area, in order to avoid biasness of RF.

The RF training starts with both gamma and hadron events as input. The MC simulated data and background data provides the gamma and hadron events respectively. A set of pre-defined Hillas parameters, say P, are used to identify γ-events out of hadron events. The γ/hadron separation is obtained by dividing the initial events into two subgroups of events, gamma rays and hadrons, based on optimized cuts of one randomly chosen parameter out of P parameters at a time. The optimization of the parameters cut values is obtained from the minimization of the Gini coefficient [122]. In each brunch, the algorithm chooses another parameter randomly and the subsequent division into gammas and hadrons takes place. In a particular brunch, the algorithm continues until one of the subsamples contains only gamma or hadron events. For easy identification of events, each events of a subsample, identified as γ-event, are labeled with 0, while events of other subsample, identified as hadron, are labeled with 1. The training of the RF grows up to a limit of n trees, which in MAGIC is usually n = 100. This training of RF is performed with `couch`.

This trained RF is then applied to real data using `melibea` program. Each event of the data has to pass through all the trees of previously trained RF, which allows to classify it into gamma or hadron. To quantify how likely an event is a gamma or hadron, each event is labeled with a hadronness value ranging from 0 to 1 (closer to 1 means more hadron-like event). The final hadronness value, h, of each event is determined by the mean of the hadronness assigned by all the trees during the `melibea`, h_i

$$h = \sum_{1}^{n} \frac{h_i}{n} \tag{2.12}$$

Arrival direction reconstruction

The estimation of the arrival direction of the incoming γ-ray for stereo observations is performed using the crossing point method. For single-telescope observations, *Disp* method [114, 123] is used to reconstruct the arrival direction. The *Disp* method has already been proven to be more robust and accurate method in reconstructing the arrival direction for stereo observations, therefore it is used in stereo analysis as well.

The image of γ-shower produces an elliptic image and major axis is the vertical projection of photon trajectory. Thus source position should be on major axis separated by a certain distance from the image centroid. The distance of constructed source position from the image centroid is known as *disp* and can be determined from Hillas parameters. For single *disp* value, two source positions are possible. To break this degeneracy, currently *disp* parameter is calculated (both in mono and stereo analysis) using RF algorithm, similarly as mentioned in γ/hadron separation. But in this case, the optimal cuts are chosen to minimize the variance of *disp* parameter in each brunch of RF algorithm.

In the case of stereoscopic observations, assuming that we have one image per camera, there are four estimated source positions i.e. four *disp* distances (two per image)(fig. [2.22(b)]). To estimate the accurate arrival direction, the distances between these four possible positions are calculated and the smallest one is chosen. The reconstructed arrival direction is the weighted average of the two closest positions, where the number of pixels contained in each image is used as the weight factor. The angular distance between the reconstructed and the true position of the source is denoted as θ parameter (fig. [2.22(a)]). Based on this parameter, the significance plots, i.e. the θ^2 plot can be obtained (discussed later). This method also useful in the reconstruction of events with truncated image (i.e. with large impact parameter).

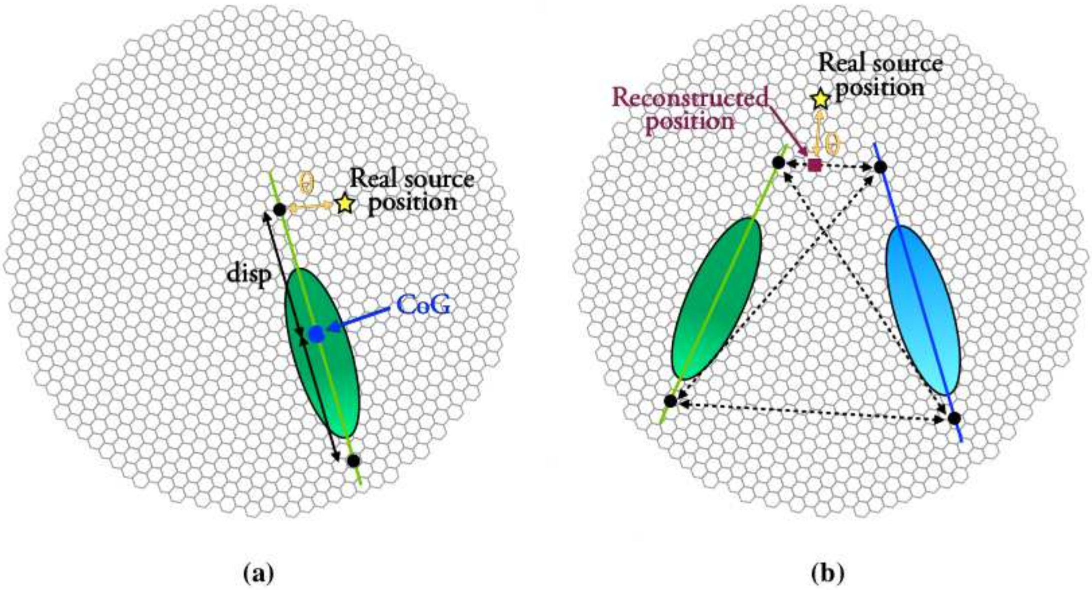

Figure 2.22: *Disp* method of arrival direction reconstruction (a) for single telescope observation (b) for stereo observation. These pictures are taken from [22]

Energy reconstruction

Based on observation mode i.e. stand-alone or stereo observation, two different methods are applied to calculate the energy of primary gamma photon. For single telescope observation, the reconstructed energy is obtained by RF algorithm which is similar to γ/hadron separation and arrival direction reconstruction. Since true energy of MC event (E_{true}) is known, the RF is trained with a set of predefined parameters selected randomly in each step, whose optimal cut is that which minimizes the variance of E_{true}.

To estimate the incident photon energy in stereoscopic observations, MC data are used but with different algorithm. The slots of a 2D histogram, binned in size and impact parameter/R_c, are filled with the E_{true} and its corresponding RMS of each event for MAGIC I and MAGIC II, separately. The estimated energy (E_{est}) of an event is the weighted average of the corresponding E_{true} for each image of both telescopes, where the RMS of each bin is used as the weight factor. The energy estimation requires a zenith correction i.e. multiplied by $cos(Zd)$, where Zd represents the zenith angle of a particular event. This 2D histogram is called the Look Up Tables (LUTs) for E_{true}. The energy bias, relative error between the E_{est} and E_{true}, is defined as:

$$E_{bias} = \frac{E_{est} - E_{true}}{E_{true}} \tag{2.13}$$

The E_{bias} of an energy bin is obtained by fitting a Gaussian to the distribution of all E_{bias} for each individual MC events included in that bin. The E_{bias} is the mean of that distribution.

Extraction of γ-ray events and calculation of significance

Signal extraction basically calculate the probability of an event to be actual signal from source over background. For stereo analysis, a program, `odie`, calculates the angular distance between the real and reconstructed source position for each event and fills the so-called signal histogram, binned in θ^2 [fig. 2.24]. Considering that the camera acceptance is homogeneous near the center where source is pointed, the background distribution would be flat over the whole histogram, while the γ-like events would accumulate at small θ^2 regime. The events used in signal histogram are chosen with predefined cuts in hadronness, size etc. The current standard set of cuts are shown in table [2.2].

To calculate significance of signal both γ-events from source and background events are calculated. Source signal (N_{on}) is counted from the number of events within source region. These events not only contain pure γ-events from source but also γ-like hadrons, $e^{\pm}$ and diffuse gammas (which are stronger for galactic sources). In order to estimate events other than γ-events from source i.e. N_{off}, another θ^2-

Energy range	E_{th} (GeV)	θ^2 (Deg^2)	Hadronness	Size (M1)	Size (M2)
Low energy	100	< 0.02	< 0.28	> 60	> 60
Medium to high energy	250	< 0.009	< 0.16	> 300	> 300
High energy	1000	< 0.007	< 0.1	> 400	> 400

Table 2.2: The standard cuts, used in MAGIC analysis, over θ^2, hadronness and size parameter are repesented here.

histogram, called background histogram, is plotted where θ is the angular distance of reconstructed source position from OFF source position [fig. 2.23]. Averaging of more than one OFF position data helps to estimate N_{off} more accurately. Since the source signal also contains the background data, the excess events are given by

$$N_{ex} = N_{on} - \alpha N_{off} \tag{2.14}$$

where α is 1/(number of OFF regions) for wobble mode observation. Once excess events are known the significance is calculated by $\sigma = N_{ex}/\sqrt{N_{off}}$, which is the Gaussian approximation of Li-Ma significance [124]

$$\sigma_{LiMa} = \sqrt{2(N_{on}\ln[\frac{1+\alpha}{\alpha}(\frac{N_{on}}{N_{on}-N_{off}})] + N_{off}\ln[(1+\alpha)(\frac{N_{off}}{N_{on}-N_{off}})])} \tag{2.15}$$

Energy resolution and threshold energy

The energy resolution defines how accurately an instrument can measure the actual energy of an event. The energy resolution is given by the RMS of the Gaussian of all E_{bias} in each bin. The current MAGIC system can achieve an energy resolution as good as 15% above a few hundred GeV. For high energy, this become worse due to truncated images and large impact factor [5].

The energy threshold of the telescope is defined as the peak of the MC simulated en-

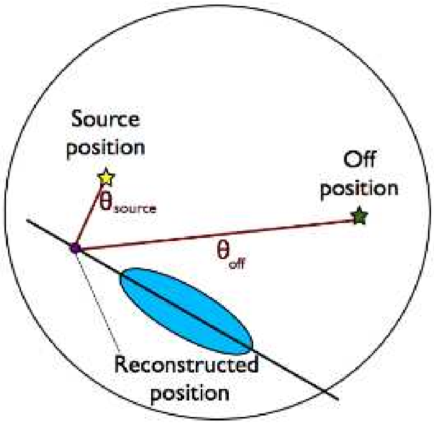

Figure 2.23: Schematic representation of measuring θ for source and background histogram. This picture is taken from [21]

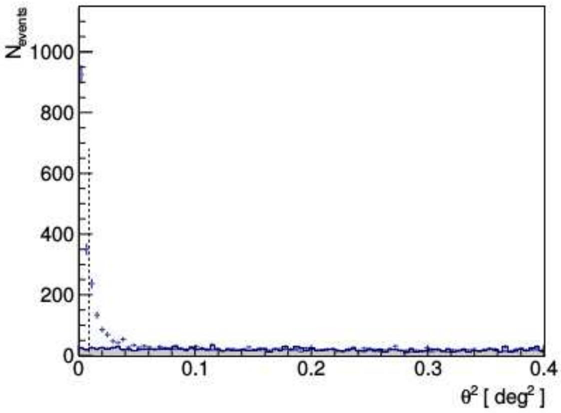

Figure 2.24: θ^2 distribution obtained for the Crab Nebula after medium-to-high cuts. The grey histogram is filled with a θ^2 calculated with respect to the off position. The points correspond to an histogram filled with a θ^2 calculated with respect to the source position

ergy distribution for a source with photon spectral index 2.6. It is usually evaluated after analysis cuts, such as hadronness, size and θ^2 cuts, to obtain the distribution of surviving events. The figure [2.25] shows a differential rate plot for two zd ranges. After applying a cut of 50 phe, hadronness and θ^2 cuts, the current energy threshold of the MAGIC telescope is ~ 75 GeV for low Zd observations.

Angular resolution

Angular resolution gives the accuracy in measuring the position of point-like source. This is also known as point spred function (PSF). Considering the 2-dimensional distribution of reconstructed arrival directions, angular resolution is defined as the angle that encloses 39% of the events. But in case of MAGIC, it is defined as the 68% containment radius. The angular resolution of MAGIC reaches a value of 0.11^0 at 250 GeV and it is as good as 0.06^0 above a few TeV [5].

Sensitivity: The sensitivity is defined as the minimum signal that can be detected in 50 hours of observation with 5σ using the significance $\sigma = N_{ex}/\sqrt{N_{off}}$. This

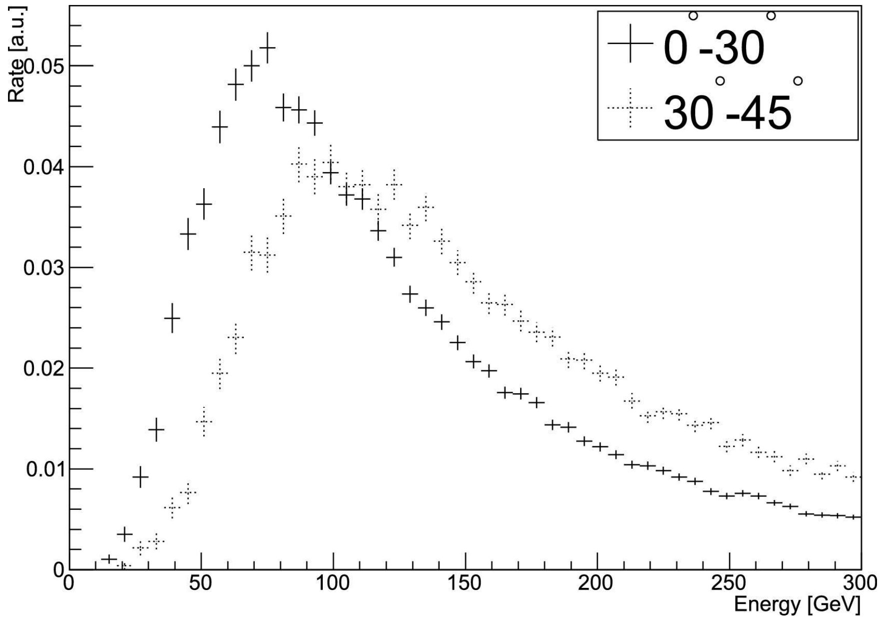

Figure 2.25: Rate of MC γ-ray events (in arbitrary units) surviving the image cleaning with at least 50 phe for a source with a spectral index of 2.6. Solid line: zenith distance below 30^0, dotted line: zenith distance between 30^0 and 45^0. This plot is taken from [5]

is generally expressed in the unit of the Crab nebula flux (C.U.). For a particular observation of time t with known N_{ex} and N_{off}, the significance at time t_0 is given as

$$\sigma(t_0) = \sqrt{\frac{t_0}{t}} \frac{N_{ex}}{\sqrt{N_{off}}} \tag{2.16}$$

The sensitivity in term of minimum flux that can be detected in $t_0 = 50$ hours with a significance 5σ in Crab units is

$$Sensitivity = \frac{5\sigma}{\sigma(50h)} \times C.U. \tag{2.17}$$

There are two ways to give the sensitivity of an instrument. A set of cuts (hadronness, size, etc) can be chosen that give the best sensitivity above a given energy threshold. This is called integral sensitivity. Similarly other set of cuts can be chosen to achieve best sensitivity in a given energy range. This is known as differential sensitivity. In the case of MAGIC, the best integral sensitivity $0.66 \pm 0.03\%$ C.U., is achieved above 220 GeV [5].

Skymap

Skymap is the 2D histogram of reconstructed direction of all excess events (N_{ex}). Here all event's coordinate are transformed into sky coordinate (mainly in RA and Dec) before filling the histogram. In `Mars` software, this task is performed with a program called `caspar`. In calculating skymap, most difficult task is the correct estimation of background event. Due to the inhomogeneities in the pixel response, stars in the FoV and observations at different Zd and Az, the background estimation is affected. In wobble mode observation, background estimation is comparatively easy, since source and background are calculated from same data sample. To avoid contamination of source region, for each wobble position camera is divided in two halves and source data are taken from the half where source present and background from other. Both N_{on} and N_{off} histogram are smoothed with two functions. One is density function (gives number of events at any camera position) which incorporate camera inhomogeneities and this is described by a Gaussian function (kernel) whose standard deviation defines the source region. The other is camera PSF which is also described by a Gaussian function with σ_{PSF} equals to angular resolution for point like source i.e $\sigma_{PSF} = 0.1^0$. Thus standard deviation of smoothed histogram is

$$\sigma = \sqrt{\sigma_{kernel}^2 + \sigma_{PSF}^2} \tag{2.18}$$

For extended source, σ_{kernel} will be bigger than for point-like source. For point source this is equal to instrument PSF. Thus

$$\sigma = \sqrt{2}.\sigma_{PSF} \tag{2.19}$$

Skymaps are usually given in terms of Test Statistics (TS) significance which is Li-Ma significance with smoothed background model.

Energy spectrum and Light curve

The differential spectrum of a source is the number of photons per unit time, per unit area and per unit energy range. This is given by

$$\frac{d\phi}{dE} = \frac{dN_\gamma(E)}{dE.dA_{eff}(E).dt_{eff}} \quad \text{photons TeV}^{-1}\text{cm}^{-2}\text{s}^{-1} \tag{2.20}$$

where N_γ is the number of gamma photons in a particular energy E, A_{eff} is the effective collection area at a given energy E and t_{eff} is the effective observation time for the source. In MAGIC analysis chain, differential flux is estimated by two dedicated programs. For mono observation, this program is `fluxlc` (FLUX and Light Curve) and for stereo observation, it is called `flute` (FLUx vs Time and Energy). These programs use both real data and MC `melibea` output as input. At this stage, each events are characterized with specific hadronness, reconstructed energy and direction. The real data are used to estimate excess γ-event (N_γ) at a particular energy range and the effective observation time (t_{eff}). The MC data are used to calculate collection area (A_{eff}).

$N_\gamma(E)$ is the number of excess events $N_{ex} = N_{on} - N_{off}$ in the energy range E. The calculation of excess events from a given data set is the same as the signal extraction, described previously. A set of cuts (on hadronness, θ^2) is chosen in each energy bin, and the number of excess events are estimated. These cuts are obtained from MC as follows: certain value of efficiency is defined to each variables, and program changes the hadronness and θ^2 cut in each energy bin until the number of surviving events reaches the fixed efficiency. These cuts are usually looser than the ones used to detect a signal, because that assures a better estimate of the collection area. The default size cut is set to 50 phe. For analyzing data taken under Moon light condition, an increased size cut is used to remove events due to increased NSB.

The effective observation time (t_{eff}) is not identical with total observation time for the source. The finite dead time of real detector and some gaps during data taking makes t_{eff} less than total observation time. Dead time is the time interval after each successful event detection for which detector is unable to registrar any new event. Assuming Poissonian distribution for arrival time distribution of cosmic events with constant rate, it can be shown that the time difference between the arrival time of an event and the next one, behaves exponentially. Thus the probability of observing n events in time t with constant rate λ is given by

$$P(n,t) = \frac{(\lambda t)^n e^{-\lambda t}}{n!} \tag{2.21}$$

Therefore, the time evolution of the probability is given by

$$\frac{dP(0,t)}{dt} = \lambda e^{-\lambda t} \tag{2.22}$$

The event rate of total N_0 events is

$$\frac{dN}{dt} = N_0 \lambda e^{-\lambda t} \tag{2.23}$$

For constant dead time (d), fraction of event is lost and the event rate would be

$$\frac{dN}{dt} = N_d \lambda e^{-\lambda(t-d)} \tag{2.24}$$

where N_d is the triggered events. The true rate of events (λ) can be obtained by fitting an exponential to the distribution. The effective observation time can be estimated by dividing the number of triggered events with the true rate of events i.e $t_{eff} = N_d/\lambda$.

Zd range (deg)	A_{sim} radius (m)
$5 - 35$	350
$35 - 50$	500
$50 - 62$	700
$62 - 70$	1000

Table 2.3: The collection area obtained from MC simulation for different zd ranges are repesented here.

The collection area is the geometrical area around the telescopes where the gamma rays are detected. MC simulated γ-events are used to calculate the simulated collection area (A_{sim}) of an ideal instrument which would detect all simulated events for a given energy and Zd range. The values of A_{sim} for different zd range are given in Table [2.3]. The effective collection area is given as

$$A_{eff} = A_{sim}\frac{N_{sur}(E)}{N_{sim}(E)} \tag{2.25}$$

where $N_{sim}(E)$ is the total simulated events for a given energy range and $N_{sur}(E)$ is number of events that survive the cuts in a given energy range. Usually, MC gammas rays are simulated with a power-law function. In the case of MAGIC, the photon index is $\Gamma = 2.6$.

Light curves show integral fluxes in a given energy range and in bins of time. Conventionally integral flux is calculated above a certain energy threshold E_0 in each time interval. Thus given as

$$\phi_{E\geq E_0}(t) = \int_{E_0}^{\infty} \frac{d\phi}{dE} dE \quad \text{photons cm}^{-2}\text{s}^{-1} \tag{2.26}$$

The other useful parameter is Spectral Energy Distribution (SED) and given as

$$E^2\frac{d\phi}{dE} = E^2\frac{dN_\gamma(E)}{dE.dA_{eff}(E).dt_{eff}} \quad \text{TeV cm}^{-2}\text{s}^{-1} \tag{2.27}$$

This is used in broadband spectrum study. SED shows the relative contribution of each wavelength to the total energy released by the source.

Upper limit

Flux Upper limit (UL) is estimated when no significant γ-ray signal is found. The number of excess events (N_{ex}), number of off events (N_{off}), a predefined value of Confidence Level (C.L.) and systematic error are used to calculate an UL to the maximum number of expected signal events N_{UL} using the method described in [125]. The C.L. usually used to calculate MAGIC ULs is 95% and the systematic error assumed is 30%. If no information about the source is available, a power law energy spectrum is assumed with photon index $\Gamma = 2.6$. The flux of non detected source is given by

$$\phi(E) = KS(E) = K(E/E_0)^{-\Gamma} \tag{2.28}$$

Thus integral flux above E_0 would be

$$\int_{E_0}^{\infty} \phi(E)dE = K \int_{E_0}^{\infty} S(E)dE = \frac{N_{UL}}{\int_{E_0}^{\infty} \int_0^{t_{eff}} A_{eff}(E)dEdt} \tag{2.29}$$

where t_{eff} is the effective time of the observation. The UL on the integral flux can be estimated from above equation as

$$K_{UL} < \frac{N_{UL}}{t_{eff} \int_{E_0}^{\infty} S(E)A_{eff}(E)dE} \quad \text{photons cm}^{-2}\text{s}^{-1} \tag{2.30}$$

Detection of VHE γ-photons with Water Cherenkov Detector

Water Cherenkov Detection technique is another successful indirect method to observe VHE γ-photons. The use of Cherenkov emission in water for charge particle detection was first pioneered by Haverah Park experiment between $1970 - 90$. In ground based gamma-ray astronomy, IAC and water Cherenkov detection techniques are complementary to each other. The IAC telescopes are pointed instruments with a comparatively small field of view. On the other hand, water Cherenkov observatories (WCOs) have large field of view and observe the sky in survey mode. Thus present generation IAC telescopes are suitable for the deep observation of point-like or nearly point-like source whereas WCOs are appropriate for observing sources of larger extension. With respect to the operating energy range, these methods are also complementary to each other, but the sensitivity of WCO is less compared to IAC technique.

Basic Principle

The high energy γ-photon, after entering the earth's atmosphere, initiates EAS via interacting with air molecules. The charge particles and photons of EAS propagates to the ground in the form of a thin circular disc of particles at nearly the speed of light. Unlike IAC telescope which detects emitted Cherenkov photons in air medium, water Cherenkov detector (WCD) detects the charge counterpart using the Cherenkov effect of water medium. High energy photons also produce Cerenkov light once they produce a $e^{\pm}$ pair, with a typical depth of 37 cm needed for this pair production process in water. The WCDs are basically a container opaque to visible light and equipped with a high speed photodetector system, made of photomultiplier tubes (PMTs). Due to high refractive index of water ($n_{water} = 1.33$), Cherenkov emission angle is $\sim 41^0$ which is much broader than in air medium. The large Cherenkov cone in water ensures high detection efficiency with low density of photodetector system. For significant and efficient observations, an array of WCDs are required which should be able to contain atleast one full cascade. This requires that linear size of array (in both X and Y direction) should be comparable with the lateral distribution of EAS at that altitude.

In WCDs, isolation of Cherenkov radiation from ambient light makes this detector suitable for continuous observation through out the diurnal cycle. This provides very high duty cycle and long exposure time. The incoming direction of the shower is estimated from the precise time measurement of the arrival of the particle front in different parts of the array. For individual PMTs located a few meters apart, a timing resolution of ~ 1 ns is required in order to attain sub-degree angular resolution. For ground based gamma detector, background rejection is one of the biggest challenge as cosmic ray flux is 10^4 times stronger than γ-ray in GeV-TeV range. The hadronic background showers can be reduced significantly by analyzing the 2D pattern of triggered PMTs and their charge. Efficient discrimination of hadronic cascade using 2D pattern analysis requires fine sampling of particle cascade on ground. As water Cerenkov observatories (WCOs) require the arrival of particles upto the detector, they benefit from a high altitude location. WCO can detect any celestial sources which transit inside a cone of 45^0 aperture centered on the Zenith, which is nearly equivalent to a field of view of 2 sr.

High Altitude Water Cherenkov gamma-ray observatory

The High Altitude Water Cherenkov (HAWC) [6, 7] gamma-ray observatory is a second generation telescope which uses the Cherenkov effects in water for observing VHE gamma photons. It is situated at Sierra Negra in the state of Puebla in central Mexico ($18^0\ 59'41''$ N, $97^0\ 18'30.6''$ W) at 4100 m above sea level. This is an upgraded and modified version of previous Milagro [8] experiment. The HAWC observatory contains an array of 300 WCDs which cover an area over 22000 m^2. It can successfully detect γ-photons and CR over an energy range starting from 100 GeV to 100 TeV. The energy upper limit is well above the present generation IACT range and opens a complementary energy window. Instantaneous FoV of HAWC is $\sim$ 2 sr which covers 15% of the sky. This makes HAWC a potential instrument to observe extended sources. The duty cycle of HAWC is $>$ 95%. The high duty cycle with large FoV also makes HAWC suitable for scanning unrevealed TeV sky. The figure [4] shows full HAWC array. Detailed simulations show that the angular resolution of HAWC is about 0.1^0 and energy resolution is around 30% for energies greater than 10 TeV [25].

Figure 2.26: High Altitude Water Cherenkov experiment with an array of 300 WCDs. This picture is taken from [23]

The higher altitude of HAWC observatory than Milagro is one of key features of its improved sensitivity. The lateral distribution of EAS depends on the depth in the atmosphere. For γ-induced EAS, the shower reaches it's maximum when energy per particle becomes $\sim$ 83 MeV (see in sec. *Gamma-ray initiated EAS*).This corresponds to a height of 5400 m in air. The height of HAWC site is comparatively close to this height than Milagro (2630 m). This significantly helps to achieve an improved sensitivity over Milagro by about a factor of 15 [25].

Water Cherenkov Detector (WCD)

The WCDs are cylindrical tanks, made of corrugated steel, of 7.3 m diameter and 5 m in height as shown in figure [2.27]. Each tank contains watertight bladder whose inner side is coated with black color. Each tank is filled with $\sim 200,000$ litres of purified water which covers a vertical height of 4.5 m. The bottom of each tank is equipped with 4 upward facing HAMAMATSU PMTs. One 10-inch Hamamatsu R7081 $- MOD$ PMT with high quantum efficiency is placed at the center and three 8-inch Hamamatsu R5912 PMTs form an equilateral triangle with 10-inch PMT at centeroid whose vertex is at 1.8 m away from the center [fig. 2.27]. The whole structure is covered by a dome, made of robust steel frame, to protect from natural calamities.

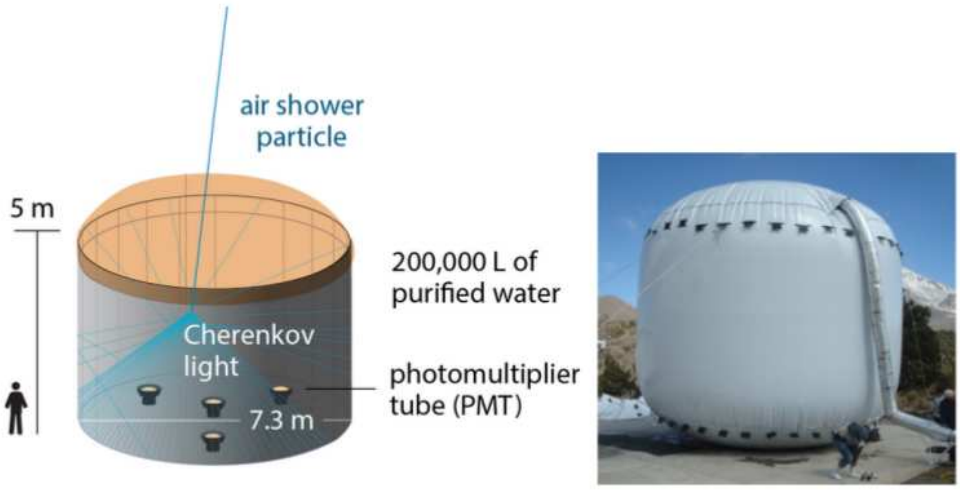

Figure 2.27: Left Panel: Schematic of a HAWC WCD. This shows simulated Cherenkov radiation from an incoming particle and four upward facing PMTs at the bottom. Right panel: Outside view of WCD which is covered with inflated bladder, white in color from outside. The figure is taken from [23]

The secondary products, which reaches at the height of HAWC, from an EAS mostly consist of $e^{\pm}$, γ, and $\mu^{\pm}$ These secondary particles are captured by WCDs. Due to it's high refractive index, water is an excellent medium to produce Cherenkov light from high energy charge particles. The purified water is used to increase the attenuation length up to $\sim$ 10 m for the wavelength range of 300 nm to 500 nm. The detailed simulation shows that electromagnetic (EM) components of EAS loss almost all of their energy via Cherenkov radiation when traversing a minimum distance of $\sim$ 4 m in purified water medium. Thus almost all energy associated with EM part of EAS is converted in radiation well before hitting the bottom of the tank and this radiation is detected with 4 PMTs. But most of muons can reach the bottom of the tank and produce light through out their track length.

Air shower reconstruction

The analysis of ground based WCD data starts with air shower reconstruction. This consists of estimation of core position, arrival direction and identification of the nature of primary particle.

Estimation of core position

In the development of EAS, Coulomb repulsion and transverse momentum reinforce secondary charge particles to move away from shower axis and form circular disc of few meter thickness. The impact point of shower axis on ground is called the core position (fig. [2.28]). The particle density is maximum near shower axis and decreases rapidly with lateral distance from the axis (fig. [2.13]). HAWC array basically registrar the energy density of EAS as the function of lateral distance from shower axis. The estimation of core position is possible by calculating the center of mass (COM) of the measured charge distribution. For detailed analysis, well known Nishimura-Kamata-Greisen (NKG) function is used to fit the observed charge distribution and core position are obtained from fitted model parameters. More details can be found in [24, 28].

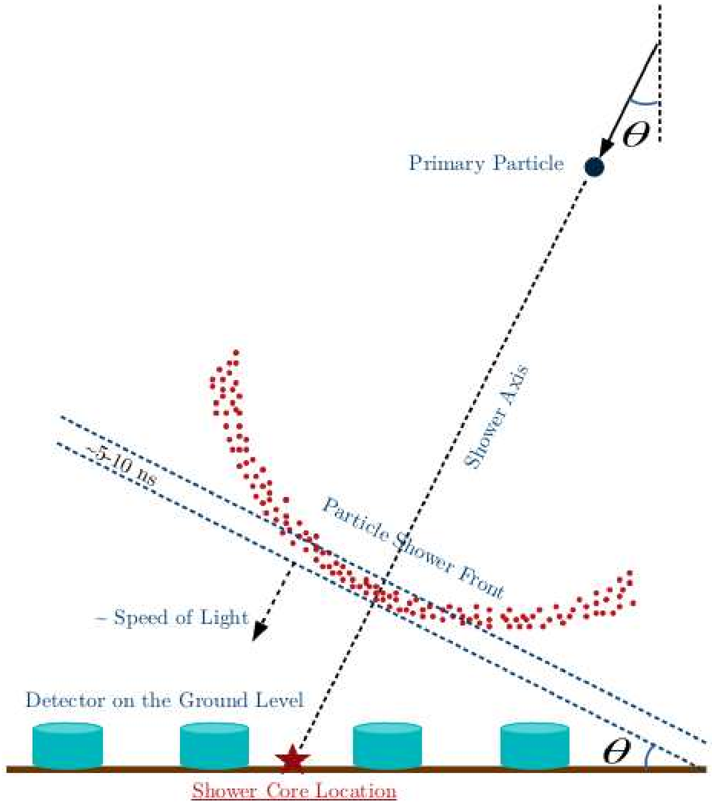

Figure 2.28: Schematic of the detection of an EAS with array of WCD. The shower of secondary particles are shown as few nSec thick particle shower front. The impact point of the shower axis on the ground is the core location shown with the red star. The zenith angle of incoming shower is θ. This picture is taken from [24]

Estimation of arrival direction

To reconstruct the direction of shower axis, HAWC uses the precisely measured arrival time information of each PMTs. Considering plane secondary particle front, it is clear from figure [2.28] that each WCD detect shower front few nSec earlier than it's right side one. Thus the arrival time profile of all triggered PMTs is used to produce the shape of the shower front. This shower front is fitted with plane wave function using χ^2 minimization where each PMT is weighted by it's measured charge. The slightly curved nature of actual shower front, obtained from detailed simulation, is included as a form of correction factor in timing information of each PMT. The estimation of shower front orientation with respect to zenith gives the arrival direction. For more detail description, refer to [28].

γ/Hadron separation

In ground-based γ-photon detector, CR flux plays an crucial role as dominant background and thus separation of gamma and hadron-induced showers is an essential task. γ/hadron separation is more difficult in WCD detector than IACT. However hadronic interactions and large transverse momentum transfer in hadron induced shower make it quiet different from γ-induced shower. The lateral particle distribution in hadronic shower is more random and chaotic than in EM shower. To distinguish γ-events from hadron, some parameters are defined which describe the smoothness of lateral energy distribution. The value of these parameters are calculated for each triggered events and predefined cuts are used to reduce CR background. Typical examples for simulated proton and gamma showers are shown in fig. [2.29]. For detail description refer to [23, 28].

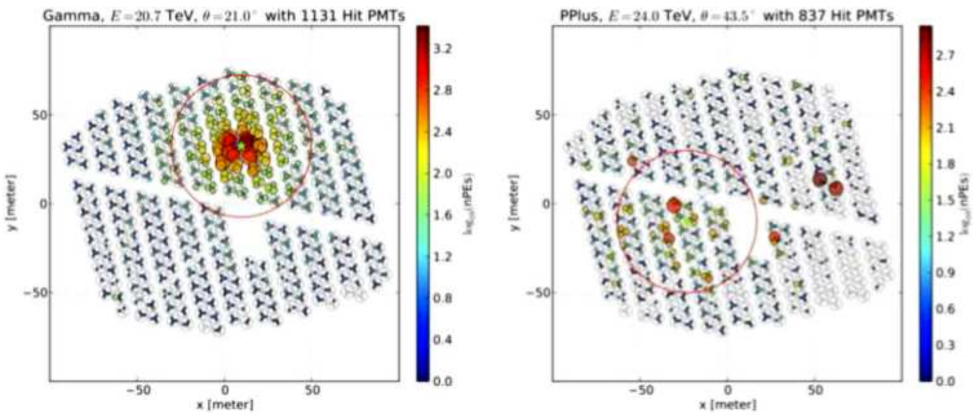

Figure 2.29: Example for a simulated gamma shower (left panel) and proton shower (right panel) as observed by the full HAWC detector. The color code indicates the number of photoelectrons per PMT. These plots are taken from [25]

CHAPTER 3

Analysis of HE gamma-photon emission from supernova remnant 3C 391 and multi-wavelength modeling with hadronic mechanism

In this chapter, we describe the HE gamma emission from the supernova remnant 3C 391 as a consequence of hadronic emission mechanism via neutral pion decay process (see in *chapter 1*).The first part of this chapter represents the importance of choosing 3C 391 as a potential candidate and describes multi-waveband astrophysical observations of 3C 391. The second part is mainly focused on the GeV data analysis (Fermi-LAT data) and detailed description of multi wavelength modeling of 3C 391 with the help of hadronic emission mechanism. The thermal X-ray emission of 3C 391, observed by Suzaku in KeV band, has also been explained with the recombining plasma scenario. This chapter is primarily based on work, named as *Recombining Plasma in the gamma-ray-emitting mixed-morphology supernova remnant 3C 391* which was published in *The Astrophysical Journal* on 2014 [126][arXiv:1406.2179v1]. In this work, I have participated in GeV data analysis and modeling of 3C 391 and X-ray part is done by other collaborators.

Galactic Source of hadronic gamma-ray emission

A supernova remnant (SNR) is the ejecta of a supernova explosion of a massive star and represents the class of most energetic gamma-ray emitters in galactic astronomy. About 10% of the Galactic SNRs have radio shells and center-filled thermal X-rays which are called mixed-morphology (MM) SNRs [127]. Middle-aged MM SNRs interacting with molecular clouds (MC) form a special class of galactic sources in terms of their distinctively higher GeV luminosities than those of other detected SNRs, i.e. $\sim 10^{35} - 10^{36}$ erg s^{-1} for IC443, W28, W51C, W44, and W49B [128–133].

MM SNRs interacting with MC are interesting targets for the detection of gamma rays of hadronic origin, which provides clear evidence that these SNRs are sites of proton acceleration [134]. The hadronic mechanism is the production of two gamma rays from the decay of a neutral pion created in a proton-proton interaction. In supernova (SN) explosion, the ejected materials from the outer layer of the progenitor star produce an outgoing spherical shell of supersonic velocity, known as SNR blast wave. The presence of dense molecular cloud in the vicinity of SN explosion provide a different scenario compared to the SN explosion far away from star forming region. The passage of supersonic SNR blast wave through the dense molecular material around source produce a strong shock in that medium. The abrupt change in pressure and temperature around the shock wavefront accelerates particles to high energies via a cumulative effect of random back and forth movement of particles through shock wavefront due to inhomogeneous magnetic field [135]. This diffusive shock acceleration process produce high energy protons from hydrogen rich molecular cloud medium and provide a potential target for hadronic gamma-ray emission. The gamma-ray spectra of these SNRs rise steeply below 250 MeV and at energies greater than 1 GeV they trace the parent proton energy distribution [134]. Interactions with MC may hint that MM SNRs are associated with star forming regions containing massive stars with strong stellar winds surrounded by circumstellar matter (CSM) and possibly these massive stars are the progenitors of MM-type remnants. When the supernova (SN) blast wave breaks out of the CSM into the ISM, its velocity rapidly rises and the particle acceleration increases. The amount of gamma-ray emission from an SNR blast wave breaking out of the CSM has been calculated in [136].

In case of young SNRs, the shock, due to SNR blast wave, creates an X-ray emitting plasma where thermal energy of electrons (kT_e) is higher than the ionization energy (kT_z). This is called ionizing plasma (IP) which, with time evolution, gradually reaches in an equilibrium state, called collisional ionization equilibrium (CIE), characterized by $kT_e = kT_z$. Recent X-ray studies of *ASCA* [137, 138] and *Suzaku* on MM SNRs revealed the existence of radiative recombining plasma scenario [138–141] in middle aged SNRs where the thermal energy of electrons is less than ionization energy ($kT_e < kT_z$). There are two main scenarios to describe the origin of recombining plasma (RP) in SNRs.

1) Thermal Conduction: When the hot ejecta inside the SNR interior, which is in the form of normal IP or CIE plasma, encounters cold MC, the electron energy will be transferred to the MC by thermal conduction and the electron temperature falls rapidly [142–144]. This condition then forms the RP.

2) Adiabatic Cooling: If the CSM surrounding a progenitor is dense enough, CIE plasma will be formed at the early stages of the evolution of an SNR. When the blast wave breaks out of the dense CSM and expands rapidly into the rarefied ISM, the electron temperature drops due to the fast cooling by adiabatic expansion, which results in RP [136, 145, 146].

To identify the galactic hadronic gamma-ray emission, a Fermi-LAT detected middle aged SNR, 3C 391 has been chosen as a potential candidate. It's interaction with surrounding MC was confirmed by 1720 MHz OH masers and near-infrared observations (details are given below). The Galactic SNR 3C 391 (G31.9 + 0.0), a member of the MM class, was suggested to be a result of an asymmetric core-collapse SN explosion of a massive ($\gtrsim 25 M_\odot$) progenitor star [147]. The HI absorption measurements by [148], show that the distance to 3C 391 is at least 7.2 kpc (assuming a Galactocentric radius of 8.5 kpc) and for the emission without absorption indicate an upper limit of 11.4 kpc.

Multi-wavelength observations of the region of 3C 391

In the radio band, 3C 391 is observed by VLA [149] as a partial shell of $5'$ radius with a breakout morphology, where the intensity of the radio emission in the shell rises in the bright northwest rim (NW) and drops and vanishes toward the southeast rim (SE). The CO(1-0) line observations of 3C 391 by [150] showed that 3C 391 is embedded in the edge of an MC supporting the idea that the progenitor has exploded within the MC and that the SN blast wave has now broken out through the cloud boundary. Indirect evidence for 3C 391 expanding into a medium with different gas density comes from X-rays. In the X-ray band, 3C 391 was observed with *Einstein* [151], *ROSAT* [152], *Chandra* [153], and *ASCA* [137, 138]. *ROSAT* and *Einstein* data revealed two bright X-ray peaks within the SNR: a brighter X-ray peak toward the interior of the weak SE radio rim and a fainter one in the interior of the bright NW radio shell.

Using *ROSAT* observations, [152] applied a single-temperature thermal model and obtained an absorbing column density of $N_H \sim 2.4 \times 10^{22}$ cm^{-2} and electron temperature of $kT_e \sim 0.5$ KeV. They also found enhanced abundances of Mg, Si, and S. [153] found that the X-ray spectra obtained from *Chandra* data can be best described by the non-equilibrium ionization collisional plasma (VNEI) model. The spectral fits showed that the diffuse emission have ionization parameters ($\tau = n_e$t) close to or higher than 10^{12} cm^{-3} s. They concluded that the hot plasma in the SNR is very close to, or in, the ionization equilibrium. They found the electron temperature at $\sim 0.5 - 0.6$ KeV and estimated an age of $\sim 4 \times 10^3$ yr for the remnant. From the data of *ASCA* observation, [138] found the electron temperature value as ~ 0.53 KeV by applying a non-equilibrium ionization (NEI) model to the spectra. They obtained an ionization timescale of $\tau \sim 2.5 \times 10^{12}$ cm^{-3} s suggesting that the plasma has reached ionization equilibrium.

Two OH masers at 1720 MHz with velocities 105 and 110 km s^{-1} has been observed in coincidence with the southeast and northeast rim of 3C 391 respectively [26]. This shows first clear evidence for 3C 391 interacting with an MC. The CO(1-0) data supports the evidence of SNR-MC interaction [150]. Further evidence for shock interactions are obtained through the CS line observations [154], the measurements of strongly enhanced [O I] 63 μm [155] at the NW rim of 3C 391, and the recent OH maser observations by [156].

3C 391 was observed in GeV gamma rays by Fermi-LAT [2] and it was listed in the 2nd Fermi-LAT catalog [157] as a point-source, called 2FGL J1849.3 − 0055. The analysis of the GeV data of 3C 391 showed a $\sim 12\sigma$ detection [133]. They also showed that the peak of the significance map was shifted $4'$ away from the NW edge of the radio shell. The spectrum of 3C 391 was best described as a power-law model with a spectral index of $\Gamma = -2.33 \pm 0.11$. They found the integrated flux of 3C 391 as $F(0.1\text{-}100 GeV) = (1.58 \pm 0.26) \times 10^{-7}$ photons cm^{-2} s^{-1} [133]. At TeV energies, H.E.S.S. reported integral flux upper limits at the 95% CL in units of the flux of the Crab nebula as 0.8 Crab units [158].

The gamma-ray emission from 3C 391 might be the result of hadronic interactions between the SNR shock and the associated MC. To understand if this is the case, we have performed a detailed GeV data analysis of 3C 391 including the study of gamma-ray source morphology and variability. We have also performed the modeling of the GeV gamma-ray spectrum. Moreover, we investigated the characteristics of the continuum radiation; thermal bremsstrahlung continuum or radiative recombination continuum (RRC) by utilizing the superior spectral capabilities for diffuse sources of XIS onboard the *Suzaku*. We report on our results of RP in 3C 391 and discuss different scenarios of its origin.

Fermi-LAT data analysis of 3C 391

To explore the gamma-ray emission from 3C 391, we analyzed the Fermi-LAT data in GeV regime. The analysis of MeV to GeV data also provides the characteristics of gamma spectrum at low energy end which will ensure the hadronic emission [134].

Description of data selection criteria and analysis parameters

The Fermi-LAT data analysis of the 3C 391 has been done with 5 years data taken in the period between 2008-08-04 and 2013-08-18. The photon was taken from a circular region of interest (ROI) with a radius of 18° centered at the position of RA(J2000) = $18^h\ 49^m\ 26^s\!.40$ and Dec(J2000) = $-00^\circ\ 55'\ 37''\!.20$ and the events suggested for Fermi-LAT Pass 7 for galactic point source analysis type were selected using *gtselect* of Fermi Science Tools (FST). To prevent event contamination at the edge of the field of view caused by the bright gamma rays from the Earth's limb, we cut out the gamma rays with reconstructed zenith angles greater than 105°. For the rest of the analysis, we used the *pointlike* [159, 160] (FST-v9r32p0) and the standard binned likelihood analysis tools (FST-v9r27p1), both based on the *gtlike*, to cross-check the validity of the results. The analysis was performed within a square region of $\sim 25^\circ \times 25^\circ$. The gamma-ray events in the data were binned in energy at 15 logarithmic steps between 250 MeV and 300 GeV. For the binned likelihood analysis [161], the matching energy dependent exposure maps were produced based on pointing direction, orientation, orbit location, and live-time accumulation of LAT.

The point-spread function (PSF) of Fermi-LAT is up to 3° at 100 MeV and 0°.1 above 10 GeV. The large PSF of LAT means that at low energies, sources from outside the ROI can affect our source. To compensate for this and to ensure that the exposure map accounts for contributions from all the sources in the analysis region, exposure maps were created such that they included sources up to 10° outside the ROI. In addition, since at low energies the PSF is large, the exposure map was expanded by another 10° to accommodate this additional exposure [161].

Likelihood analysis and its application to 3C 391

Likelihood, in statistics, is a function of parameters of a statistical model which is defined as the probability of obtaining a given observed outcome from some definite values of the parameters of the model. This is useful to obtain the effectiveness of a set of parameter values to produce a given outcome. Likelihood analysis is also performed to obtain the best value of a set of parameters which can fit the observed data as good as possible.

In case of Fermi-LAT data analysis, we construct a likelihood that is applicable to LAT data and then we maximize this likelihood to obtain best fit value of the parameters of the input model. The input model is the distribution of gamma-ray sources on the sky according to the Fermi catalog, and includes their location and spectra in the form of some parameters. We estimate the value of these parameters from analysis so that our input model can reproduce the observed data at best. We have an implicit assumption that there is sufficiently accurate mapping between input model and counts produced in the detector. For a single source analysis, we have to consider the contribution from neighbouring sources due to large PSF of LAT at low energies and to estimate the value of parameters of a single source, we have to vary the parameters of all sources within ROI simultaneously. The fitting of the parameters require repeated likelihood calculation for different sets of trial value of parameters. The choice of new trail parameter set to converge efficiently to best fit is guided by different optimizer.

LAT data are distributed into a large number of bins because of characterization with many variables. The events in each bin are Poisson distributed and for small counts it cannot be approximated as normal distribution. The value of likelihood function L is the product of probabilities of detected counts in each bin. If the expected number of counts for i-th bin, according to the source model, is m_i, the probability of n_i detected count is

$$P_i = \frac{m_i^{n_i} exp[-m_i]}{n_i!} \tag{3.1}$$

The likelihood is given by

$$L = \prod_i P_i \tag{3.2}$$

P_i can be considered as the product of two factors, $m_i^{n_i}/n_i!$ which depends on data (detected number of counts n_i) as well as input model (expected count m_i) and $exp[-m_i]$. For L, the products of second part is the exponential of minus the sum of all m_i. This sum is the total number of expected counts N_{exp} that source model predicts. Thus L can be written as

$$L = exp[-N_{exp}] \prod_i \frac{m_i^{n_i}}{n_i!} \tag{3.3}$$

This likelihood, with finite size bins and n_i that may be greater than 1, is the basis for binned likelihood. The finite bin size looses some information and therefore accuracy decreases. The binned likelihood analysis with smaller bin size is more accurate.

In usual source detection, two hypothesis are assumed; one is null hypothesis with no new source and other is alternative hypothesis with the assumption of the existence of a new source at a particular location. To compare the effectiveness of these hypothesis in explaining the observed data, test statistics (TS) i.e. ratio of likelihood function values using both hypothesis is used and this is defined as

$$TS = 2\ln\frac{L(\text{Alternative hypothesis;N}_{obs})}{L(\text{Null hypothesis;N}_{obs})} \tag{3.4}$$

where L and N_{obs} represent likelihood function and the total observed counts of specific observation respectively. The square root of test statistics value i.e. $\sqrt{TS}$ is interpreted as the significance of excess counts in unit of 'Gaussian sigma'.

The spectral properties of the gamma-ray emission were studied using likelihood method by comparing the observation with models of possible sources in the ROI. Predictions were made by convolving the spatial distribution and spectrum of the source models with the instrument response function (IRF) and with the exposure of the observation. In the analysis we used the IRF version P7SOURCE_V6.

The model of the analysis region contains the diffuse background sources and all the point-like sources from the 2nd Fermi-LAT catalog located within a distance of 18° from the ROI center. We fixed all parameters of the point-like sources in the model, except 3 sources (shown in Figure [3.1] with yellow markers) within the distance of 2° from the best-fit location of 3C 391, where we set their normalization and spectral parameters free. The standard diffuse background model has two components: the diffuse Galactic emission (*gal_2yearp7v6_v0.fits*) and the isotropic component (*iso_p7v6source.txt*), which is a sum of the extragalactic background, unresolved sources, and instrumental background. The normalization of the galactic diffuse background is set free during the analysis. The normalization of the isotropic component is fixed to one due to the difficulty to disentangle it from Galactic interstellar emission over limited regions.

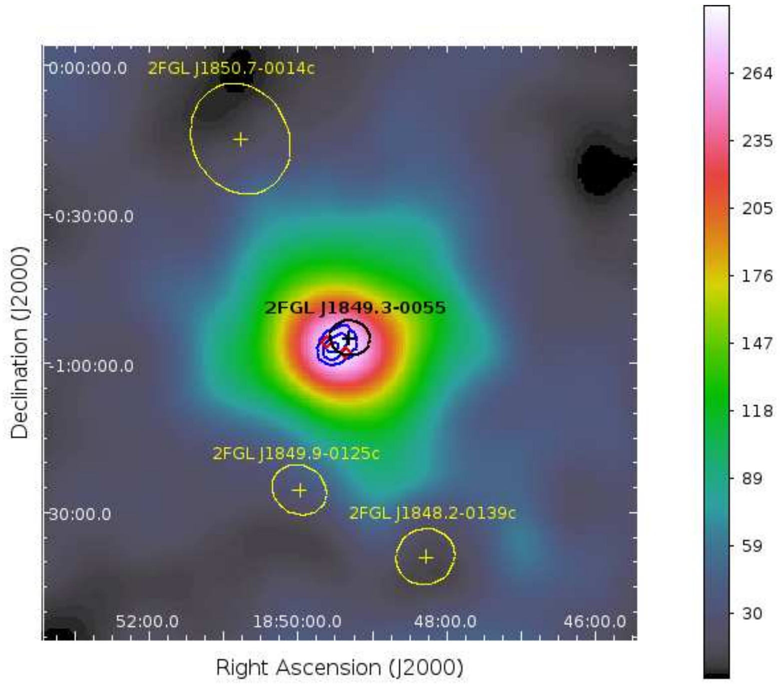

Figure 3.1: Gamma-ray TS map of the 3C 391 neighborhood with a bin size of 0°.01 × 0°.01. The blue contours show the *Suzaku* data, where 3 contours represent 14, 29, 43 cts. The yellow crosses and circles represent the 2nd Fermi-LAT catalog sources and the black cross and circle is the GeV source from the 2nd Fermi-LAT catalog corresponding to SNR 3C 391. Two red diamonds represent the two masers detected by [26].

The background and source modeling was done by the binned likelihood analysis using *gtlike* of FST. To determine the best set of spectral parameters of the fit, we vary the parameters until the maximum likelihood is maximized. The detection of the source in this analysis is given by test statistics (TS) value, where larger TS values indicate that the null hypothesis (maximum likelihood value for a model without an additional source) is incorrect. This means that the detection significance is approximately equal to the square root of TS.

Finding best fit source position and spectrum

Using both FST *binned likelihood* (with FST-v9r27p1) and *pointlike* (with FST-v9r32p0) analysis we detected 3C 391 with a significance of $\sim 18\sigma$. We computed the best-fit position within the ROI of 3C 391, which was found as longitude l = $31^\circ.879 \pm 0^\circ.022$ and latitude b = $0^\circ.022 \pm 0^\circ.022$. This best-fit position (RA(J2000) = $18^h49^m26^s.34$ and Dec(J2000) = $-00^\circ55'37''.35$) enhanced the TS by 2.58σ over the position of 2FGL J1849.3−0055 in the 2nd Fermi-LAT catalog. Then the model was refitted using the best-fit position to compute the TS map and the spectrum.

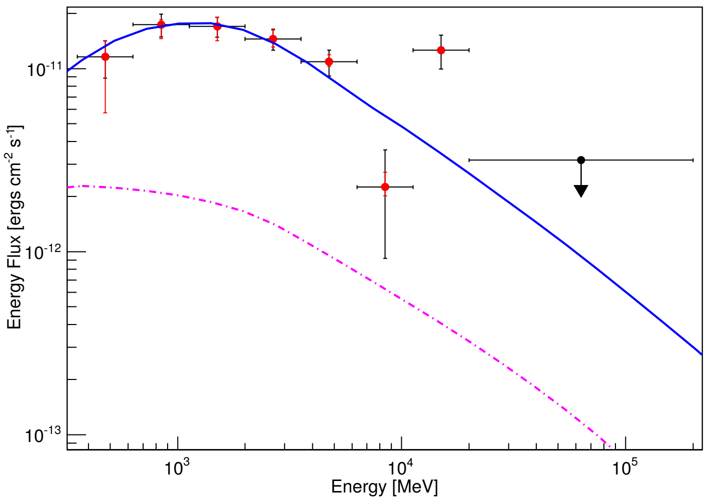

Figure 3.2: The gamma-ray SED of 3C 391, where the Fermi-LAT spectral data points are represented with red filled circles and their corresponding statistical and systematic errors are shown in black and red lines, respectively. The black arrow represents the integral flux upper limit at TeV energy, reported by H.E.S.S collaboration. The thick blue line passing through the data points shows the hadronic model fit to the data. The dashed-dotted magenta line represents the bremsstrahlung spectrum. The parameters used to estimate the emission spectra both for hadronic and leptonic models are mentioned in sec. *Multi-wavelength modeling of 3C391.*

The observed spectral energy distribution (SED) of 3C 391 is shown in Figure [3.2], where the data points are represented by red filled circles and their corresponding statistical and systematic errors are shown in black and red lines, respectively. To check the functional form of the spectrum, we first considered 3C 391 as a point-like source. First, the power-law (PL) function was fitted to the data between 250 MeV and 300 GeV, but we noticed that the spectrum deviates from a PL function. So, we checked, if the gamma-ray emission is better described by a log-parabola (LP) or a broken power-law (BPL) function, where the functional forms are as follows:

Spectral Model	Photon Flux [10^{-8} ph cm^{-2} s^{-1}]	Γ_1	Γ_2	E_b [MeV]	TS
PL	15.0 ± 1.7	2.30 ± 0.03	–	–	337
LP	7.14 ± 0.34	2.27 ± 0.04	0.15 ± 0.45	2430	337
BPL	4.89 ± 0.57	1.28 ± 0.50	2.50 ± 0.04	1060	338

Table 3.1: Spectral fit parameters for PL, LP, and BPL between 250 MeV and 300 GeV assuming 3C 391 as a point-like source.

- Log-parabola:

  $F(E)^{LP} = N_\circ \, (E/E_b)^{(\Gamma_1+\Gamma_2 \ln(E/E_b))}$

- Broken Power-law:

  $$\begin{aligned} F(E)^{BPL} &= N_\circ \, (E/E_b)^{-\Gamma_1} \text{ for } E < E_b \\ &= N_\circ \, (E/E_b)^{-\Gamma_2} \text{ for } E > E_b \end{aligned}$$

The results to these spectral fits are summarized in Table 3.1. Using different functions in fitting the spectrum of 3C 391, the likelihood ratio, TS, was used as a measure of the improvement of the likelihood fit with respect to the simple PL. The TS values of 337, 337, and 338 were found for PL, LP, and BPL fit, respectively.

The PL resulted in spectral index of $\Gamma_1 = 2.30 \pm 0.03$, which is in agreement with the best-fit power-law index value given for 3C 391 in the 2nd Fermi-LAT catalog ($\sim$ 2.19) [157]. This result also matches to the results obtained by [133], $\Gamma_1 = 2.33 \pm 0.11$. Additionally, the LP fit results (shown in Table 3.1) were found to be in good agreement with the results in the 2nd Fermi-LAT catalog [157], which are $\Gamma_1 = 2.35 \pm 0.16$ and $\Gamma_2 = 0.308 \pm 0.099$ for a fixed E_b value of 2430 MeV.

The best-fit parameters for the BPL fit are $N_\circ = (1.15 \pm 0.69) \times 10^{-11}$ MeV^{-1} cm^{-2} s^{-1}, $\Gamma_1 = 1.28 \pm 0.50$, and $\Gamma_2 = 2.50 \pm 0.04$, where the given uncertainties are statistical. The total energy flux was found as $(6.28 \pm 0.16) \times 10^{-11}$ erg cm^{-2} s^{-1} with $E_b = 1060 \pm 250$ MeV.

Apart from the statistical uncertainties, there are systematic errors originating from the uncertainty of the Galactic diffuse background intensity. In order to calculate these systematic errors, we followed the prescriptions by [130] and [162] by varying the normalization value of the Galactic background by $\pm 6\%$ from the best-fit value and used these new frozen values of the normalization parameter to recalculate the SED of 3C 391. The systematic errors on the SED are shown in Figure [3.2] in red color on top of the statistical errors.

Study of source morphology

To investigate the morphology of 3C 391, we created a $2^\circ \times 2^\circ$ TS map of 3C 391 and its neighborhood with a bin size of $0^\circ\!.01 \times 0^\circ\!.01$. The TS map shown in Figure [3.1] was produced with *pointlike* using a background model file, which contained all the point-like sources and diffuse sources, but excluded 3C 391 from the model. So, it shows the TS distribution of gamma rays originating dominantly from 3C 391. In Figure [3.1] the blue contours represent the *Suzaku* XIS image in the $0.3 - 10.0$ keV energy band (from Figure 3.6), the yellow crosses and circles represent the 2nd Fermi-LAT catalog sources and their statistical errors, respectively, and the black cross and circle represent the location and its statistical error of the GeV source from the 2nd Fermi-LAT catalog corresponding to 3C 391, respectively. The peak value of the gamma-ray significance coincides with the X-ray remnant. The red diamonds indicate the locations of the two OH masers reported by [26].

To search for the energy dependent morphology, we split the data set into two energy ranges (250 MeV $-$ 1 GeV and $1 - 300$ GeV) and computed the TS maps for each energy range. We found no significant gamma-ray excess at the location of 3C 391 for the energy range between 250 MeV and 1 GeV, but 3C 391 was detected in the higher-energy range of $1 - 300$ GeV with a significance of $\sim 15\sigma$ using a BPL spectral model.

Additionally, using *pointlike* we have checked the extension of 3C 391 by fitting a disk template and assuming 3C 391 has a PL/BPL type spectrum. To detect the extension of a source, we use the TS of the extension (TS_{ext}) parameter, which is the likelihood ratio comparing the likelihood for being a point-like source (L_{pt}) to a likelihood for an existing extension (L_{ext}), $TS_{ext} = 2\log(L_{ext}/L_{pt})$. *pointlike* calculates TS_{ext} by fitting a source first with a disk template and then as a point-like source.

According to the extension studies by [160], the extended source detection threshold is $TS_{ext} = 16$, where the threshold is defined as the source flux at which the value of TS_{ext} averaged over many statistical realizations is 16. From simulation studies, it is found that to resolve a disk-like extension of r = $0^{\circ}.1$ at the level of $TS_{ext} = 16$, the source must have a minimum flux of 3×10^{-7} ph cm^{-2} s^{-1} for a spectral index value of 2.0 and a flux of 2×10^{-6} ph cm^{-2} s^{-1} for a spectral index value of 2.5 [160]. So, for 3C 391 TS_{ext} was found as 0.008 and 0.52 after a disk template fitting for 3C 391 having a PL and BPL type spectrum, respectively (Table 3.2). Both of the TS_{ext} values are smaller than 16, which indicate that a disk-like extension with r $\sim 0^{\circ}.1$ could not be resolved at the integrated flux level and spectral index values of 1.5×10^{-7} ph cm^{-2} s^{-1} and 2.3 for the PL type spectrum and 4.9×10^{-8} ph cm^{-2} s^{-1} and 2.5 (Γ_2) for the BPL type spectrum of 3C 391.

Disk Model	Longitude [°]	Latitude [°]	Sigma [°]	TS_{ext}
PL	31.87 ± 0.02	0.023 ± 0.017	0.10 ± 0.15	0.008
BPL	31.88 ± 0.02	0.028 ± 0.017	0.10 ± 0.26	0.52

Table 3.2: Fit results of disk-like extension model applied to 3C 391 gamma-ray data between 250 MeV and 300 GeV for the PL and BPL type spectral models.

Study of source variability and pulsation

Variability or pulsations can effect the analysis results for 3C 391. So, we checked for both of these effects in the data. We searched for long term variability in the light curve of 3C 391 produced using the data from the circular region of 1° around the best-fit position. Figure 3.3 shows the 1-month binned light curve after fitting the spectrum with a BPL, where each flux point remains within 1σ and 3σ. Fitting these flux points to a straight line (shown as a blue line in Figure [3.3], yields a χ^2/degrees of freedom (dof) of ~ 1.25. Thus, we conclude that there is no long term variability observed in the close neighborhood of 3C 391.

We have also checked if the spectral shape of 3C 391 fits to the standard spectrum of a pulsar, Power Law with Exponential Cutoff (PLEC). The best-fit cutoff energy is found as 28.80 ± 6.73 GeV, which is an order of magnitude away from the range of typical pulsar cutoff energies [163]. The PLEC fit didn't show a significant improvement over the PL, BPL, and LP spectral fits.

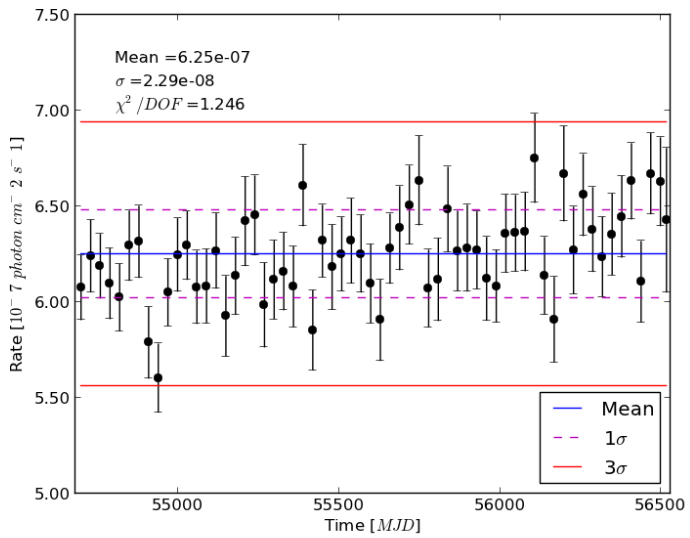

Figure 3.3: The monthly gamma-ray variability for 3C 391 with BPL-fit spectrum in the energy range of $0.25 - 300$ GeV.

Estimation of proton density in molecular environment

The presence of protons up to a certain density level in surrounding molecular environment is mandatory to produce gamma-photons effectively from hadronic mechanism. To estimate the average density of proton in the vicinity of 3C 391, we used the CO data of Harvard-Smithsonian Center for Astrophysics 1.2 m Millimeter-Wave Telescope [164]. We analyzed the CO gas in the whole velocity range integrated from -50 to 120 km s^{-1}, where the velocity intervals were divided such that each range included at least one cloud cluster peaking in temperature at a certain velocity. Figure [3.4] shows the CO maps produced at different velocity ranges of $[-50, 0]$, $[0, 15]$, $[15, 35]$ km s^{-1} starting from top-left; and $[35, 60]$, $[60, 90]$, $[90, 120]$ km s^{-1} starting from bottom-left. The white contours represent the TS values of 3C 391 gamma-ray data at 41 and 83, and the blue contours are the X-ray counts at 14, 29, and 43.

The velocity integrated CO intensity (W_{CO}) for the whole velocity range and for the region covering the whole X-ray remnant was found to be ~ 110 K km s^{-1}. Since the CO sky maps are binned as $0^\circ.125 \times 0^\circ.125$, the area corresponding to the total W_{CO} emission is $(0^\circ.125)^2$. We calculated W_{CO} for each above mentioned velocity range and found that the highest contribution at the SNR's X-ray location came from the velocity range of $90 - 120$ km s^{-1}, which is also apparent in the CO sky maps in the blue framed panel on the bottom right corner of Figure [3.4].

When we calculated the integrated CO intensity over the velocity and extent of the cloud, S_{CO}, we took all the velocity ranges into account: $S_{CO} = \sum_i (W_{CO}\ A)_i$, where i represents the different velocity ranges. So, we found $S_{CO} = 1.72$ K km s^{-1} deg^2 for CO data used from the whole velocity range. For the dominant velocity

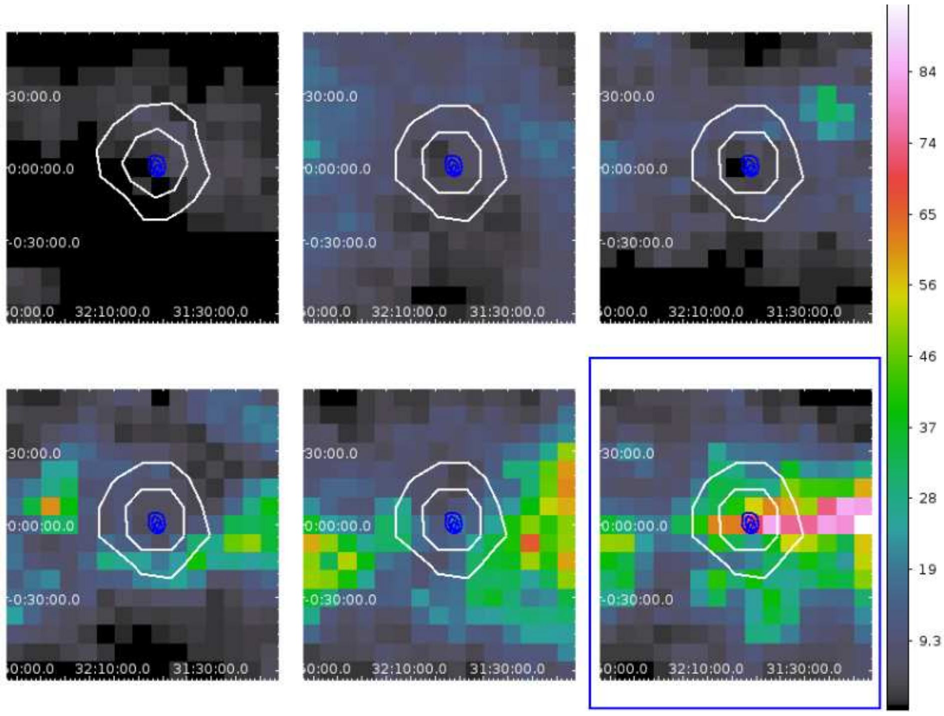

Figure 3.4: Maps in galactic coordinates (longitude-x-axis and latitude-y-axis) of the integrated CO intensity (W_{CO}) for 6 different velocity ranges (Top from left: $[-50, 0]$, $[0, 15]$, $[15, 35]$; Bottom from left: $[35, 60]$, $[60, 90]$, $[90, 120]$ km s^{-1}) at the location of 3C 391 and its vicinity. For all maps, the range for W_{CO} is fixed between 0 and 92.8 K km s^{-1}.

range of $90 - 120$ km s^{-1}, we found $S_{CO} = 1.11$ K km s^{-1} deg^2. Assuming a linear relationship between the velocity integrated CO intensity, W_{CO}, and the molecular hydrogen column density, $N(H_2)$:

$$\frac{N(H_2)}{W_{CO}} = (1.8 \pm 0.3) \times 10^{20} \text{ cm}^{-2}\text{K}^{-1}\text{km}^{-1}\text{s}^{-1} \tag{3.5}$$

as given in [165]. Equation [3.5] gives

$$\frac{M_{CO}}{M_\odot} = 1200 \; S_{CO} \; d_{kpc} \tag{3.6}$$

where d_{kpc} is the distance to the cloud in kpc. We calculated the total hydrogen column density as $N(H_2) = 1.98 \times 10^{22}$ cm^{-2} using the CO data in the whole velocity range. For the velocity range of $90 - 120$ km s^{-1} we obtained $N(H_2) = 1.28 \times 10^{22}$ cm^{-2}. The total mass of the clouds with velocities in the range of $90 - 120$ km s^{-1} was found from Equation [3.6] as M$_{CO} = 6.9 \times 10^4$ M$_\odot$ using lower limit on distance to the cloud (~ 7.2 kpc). We estimated the size of the emission region as 15.7 pc. By assuming a spherical geometry of the cloud we computed the density of the source region to be 4.25 M$_\odot$ pc^{-3} and the average density of protons to be 269 protons cm^{-3}. But using the upper limit of the distance to the cloud (~ 11.4 kpc) we obtained an upper limit to the average proton density, 671 protons cm^{-3}. Considering only the highest cloud velocity range, we recalculated the proton density as 173 and 435 protons cm^{-3} for the source distances of 7.2 and 11.4 kpc, respectively. Averaging the proton density over all different combinations of the distance and velocity parameters we obtained 387 protons cm^{-3}, whereas a typical value for giant MCs is found as ~ 300 protons cm^{-3} [150].

Multi-wavelength modeling of 3C391

To understand the origin of observed gamma-ray of 3C 391, both the hadronic and leptonic emission models have been applied to fit the GeV spectrum of 3C 391. The details of those fitting and their interpretation are described here.

First we have chosen the hadronic emission model, where gamma-ray spectrum results from the decay of neutral pions, π° [166]. In order to calculate the gamma-ray spectrum, we considered that the relativistic protons follow a BPL type spectrum:

$$\begin{aligned} \frac{dN}{dE_p} &= N_1 E_p^{-\alpha} \text{ for } E_p < E_{br} \\ &= N_2 E_p^{-\beta} exp\left(-\frac{E_p}{E_{p_{max}}}\right) \text{ for } E_{br} \leq E_p \leq E_{p_{max}} \end{aligned} \tag{3.7}$$

In Equation [3.7], E$_p$ is the proton energy and E$_{br}$ is the spectral break energy, where the spectral index changes from α to β. E$_{p_{max}}$ is the maximum energy of protons and during the fitting procedure it is assumed to be at 10 TeV. N_1 and N_2 are normalization constants.

The best-fit parameters for the proton spectrum were obtained by a χ^2-fitting procedure to the flux points. The estimated parameters are $\alpha = 2.48 \pm 0.45$, $\beta = 3.0 \pm 0.22$, and $E_{br} = 12$ GeV. The χ^2/dof is estimated to be $\simeq 1.6$. The best-fit gamma-ray spectrum resulting from the decay of neutral pions for an ambient gas density of ~ 387 cm^{-3} is shown in figure [3.2] with the blue solid line. The estimated total energy can be written as $W_p \simeq 5.81 \times 10^{48} \left(\frac{387 \text{ cm}^{-3}}{n_H}\right)$ erg, where n_H is the effective gas number density for p-p collision. In addition to BPL spectrum, different proton spectra, like PL, LP, and PLEC were considered to explain the gamma-ray spectrum. However, we didn't find any significant difference in the estimated best-fit parameters for all the input proton spectra.

To check the hadronic scenario from the energy point of view, we considered the energy from the SN explosion converted into accelerated protons, $W_p = L \times \tau_p$, where L is the gamma-ray luminosity and τ_p is the characteristic cooling time of protons. When the gamma-ray luminosity is dominated by hadronic emission, then $\tau_p = 5.3 \times 10^7$ (n/(1 proton cm^{-3}))$^{-1}$ yr [55]. Using the average proton density of 387 protons/cm^3 for n, we found $\tau_p = 1.37 \times 10^5$ yr. So, taking $W_p \sim 5.81 \times 10^{48}$ erg, the luminosity of 3C 391 was found as $L = 1.34 \times 10^{36}$ erg s^{-1}.

We also calculated the contribution from the leptonic emission models [167]. We found that the relativistic electrons can not account for the gamma-ray spectrum at GeV energies through inverse Compton (IC) and bremsstrahlung processes. We assumed the broken power-law type spectrum for electrons, which is similar to that considered for protons (Equation [3.7]). The fit to the radio data [27] gave a synchrotron spectral index $\sigma \simeq 0.55$ ($S_\nu \propto \nu^{-\sigma}$). Therefore, we took $\alpha = 2.1$ in the electron spectrum before the break, because this parameter determines the shape of the synchrotron spectrum at radio wavelengths. On the other hand, β can be found

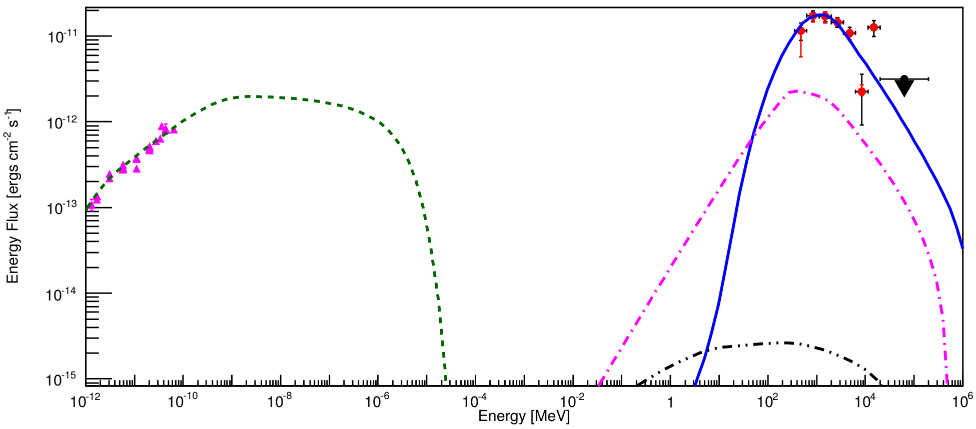

Figure 3.5: The models fit to the radio [27] (magenta filled triangles) and gamma-ray data (red filled circles with their corresponding statistical and systematic errors) are shown with solid blue (π^0-decay spectral model component), green dashed (synchrotron emission), magenta dotted-dashed (non-thermal bremsstrahlung component), and black double-dot-dashed (IC emission component) lines.

out from the fit to the observed gamma-ray spectrum. We considered an electron to proton ratio of 0.01 following the observed spectra of the Galactic cosmic electrons and protons. We then considered the magnetic field and the number of electrons in the emission volume such that synchrotron spectrum of electrons could explain the observed radio data as shown in Figure [3.5]. To estimate the spectrum from leptonic models we used the following parameters: $\alpha = 2.1$, $\beta = 3.0$, $E_{br} = 7$ GeV, B = 210 μG, n = 387 cm^{-3}. We found the total energy of electrons as $W_e = 1.4 \times 10^{47}$ erg. Assuming that the gamma rays at GeV energies are produced by the same population of electrons, we estimated the IC spectrum by taking the cosmic microwave background radiation and interstellar background radiation fields following [168]. We found that neither the IC nor the bremsstrahlung emission could account for the observed gamma-ray fluxes shown in Figure [3.5].

X-ray data analysis

To determine the existence the recombining plasma scenario, we have analyzed the thermal X-ray data of 3C 391 and after background subtraction, the excess is fitted with RC plasma model.

Observation and data reduction

3C 391 was observed with XIS on board *Suzaku* on 2010 October 22, under the observation ID of 505007010 and an exposure time of $\sim$ 99.4 ks. *Suzaku* was an X-ray astronomy satellite jointly developed by the Institute of Space and Aeronautical Science and NASA. It was developed to explore the high energy X-ray sources in the energy range of $0.1 - 100$ KeV. It was launched on 10 July, 2005 and placed at an orbit of 550 km away from earth's surface. The high spectroscopic resolution and observation over wide energy band are two essential key factors to explore the high energy astrophysical phenomenas. The *Suzaku* consists of four instruments: X-ray Telescope (XRT), X-ray Spectrometer (XRS), Hard X-ray Detector (HXD) and X-ray Imaging Spectrometer (XIS). The XIS system consists of four CCD cameras (XIS 0, 1, 2, and 3). One of the cameras (XIS1) uses a back-illuminated (BI) CCD while the others (XIS0, 2, and 3) use front-illuminated (FI) CCDs. XIS2 has not been functional due to an unexpected anomaly in 2006 November. The XIS was operated in the normal full-frame clocking mode. For detailed descriptions of the *Suzaku* satellite, the XIS instrument, and the X-ray telescope, refer to [169], [170], and [171], respectively.

For the data reduction we used *HEASoft* package version 6.11.1. The calibration database (CALDB: 20130305) was used and fitting was carried out in the X-ray spectral fitting package (*xspec*) version 11.3.2 [172]. The redistribution matrix files

(RMFs) of the XIS were produced by *xisrmfgen* and *auxillary* response files (ARFs) were generated by *xissimarfgen* [173].

Background estimation and model fitting

For the spectral analysis of 3C 391 we selected three regions, which are the whole SNR and the NW and SE regions of the SNR. These regions are shown on the XIS1 image of 3C 391 in the 0.3 − 10.0 keV energy band in Figure [3.6] as white dashed, blue solid, and black solid ellipses, respectively. The region representing the whole remnant has a size of $4'.85 \times 3'.94$ centered at RA(J2000) = $18^{\mathrm{h}}\ 49^{\mathrm{m}}\ 28^{\mathrm{s}}.6$, Dec(J2000) = $-0^{\circ}\ 56'16''.4$. The reasons for this selection are given in the Discussion section.

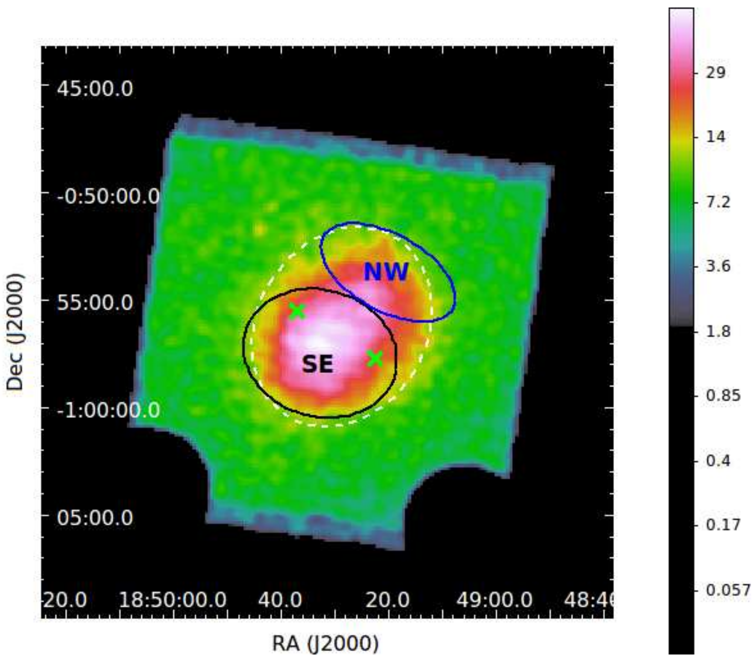

Figure 3.6: Background-subtracted FI spectrum of 3C 391 in the 1.0 − 5.0 keV energy band fitted with an absorbed VNEI model with RRC and Lyα lines of the Si and S for the whole SNR. At the bottom of this panel, the residuals from the best-fit model are shown.

The background for 3C 391 is a combination of the non-X-ray background (NXB), the Cosmic X-ray background (CXB) emission and the Galactic ridge X-ray emission, GRXE [174]. First, we estimated the NXB data from night-Earth observations using the tool *xisnxbgen* [175], and subtracted the NXB from the spectrum. We selected background region, the nearby blank sky region (Obs.ID 500009020) on the Galactic plane, consisting of the GRXE and the CXB. NXB-subtracted background spectrum was subtracted from the source spectrum using *xspec*. The spectrum was binned to a minimum of 20 counts per bin using *grppha* to allow use of the χ^2 statistic.

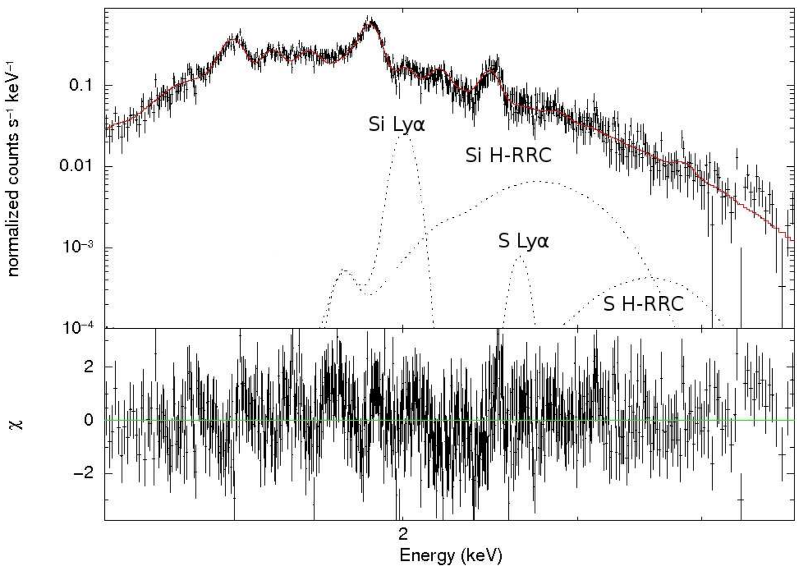

Figure 3.7: Background-subtracted FI spectrum of 3C 391 in the 1.0 − 5.0 keV energy band fitted with an absorbed VNEI model with RRC and Lyα lines of the Si and S for the whole SNR. At the bottom of this panel, the residuals from the best-fit model are shown.

We first started the XIS analysis with the whole SNR region. We applied an absorbed (wabs in *xspec*; [176]) VNEI model for a NEI collisional plasma with variable abundances [177], which gave the reduced χ^2 value of $950.2/659 = 1.44$ for the energy range of 1.0 − 5.0 keV. During model fitting N_H, kT_e, n_et, and the abundances of Mg, Si, and S were free parameters, while the other elemental abundances were fixed to their solar values [178]. Residuals of the VNEI spectral fit show that there is a clear residual emission at energies of ~ 2.0 keV and ~ 2.6 keV. Therefore, we added two Gaussian components (gauss model in *xspec*) to the VNEI model. These two lines in the spectrum correspond to the H-like (Lyα) lines of Si and S, which are the indicators of highly ionized plasma. We note that, we found Al K-shell emission at $\sim$ 1.58 keV from this remnant, as it was also found for G344.7$-$0.1 [179], G350.1$-$0.3, and G349.7+0.2 [180]. We follow the prescription described in [181] for W49B to understand if the X-ray continuum comes from the thermal bremsstrahlung process or from RRC. We added the RRC model of H-like Si (2.666 keV) and S (3.482 keV). The added Lyα lines and the RRC components improved the quality of the fit (χ^2/dof = 860/717). This suggest that these residuals are caused by the RRC of Si and S. Figure [3.7] shows the background-subtracted FI spectrum fitted with the absorbed VNEI plus RRC models and the Lyα lines of the Si and S, in the energy range of 1.0 $-$ 5.0 keV. The same analysis steps described above were also applied for the NW and SE regions of 3C 391. The parameters (90% confidence level) computed for the best-fit model obtained for the whole SNR and for the NW and SE regions are presented in Table [3.3].

Physical interpretation of analysis results

In the multi-wavelength modeling section, we have showed that the gamma-ray spectrum of 3C 391 can be described by a hadronic emission model, a clear evidence for acceleration of protons in this SNR. The neutral pion decay model assumed the protons to follow a BPL distribution with α index standing for the acceleration of cosmic rays in the shock and β index represents the energy, above which protons escape from the SNR shell. Since, the bremsstrahlung spectrum depends linearly on the number density of ambient matter, for 3C 391 it can only account for the observed spectrum at GeV energies, if n = 3000 cm^{-3}. However, the spectrum has to be much steeper at $\sim$ 1 GeV to explain the observed spectrum at this energy. Introducing an abrupt break at $\sim$ 800 MeV in the electron spectrum can explain the observed fluxes at $\sim$ 1 GeV, but this break in the electron spectrum will make

Component	Parameters	Whole	NW	SE
wabs	N_H [10^{22} cm^{-2}]	3.1 ± 0.1	3.4 ± 0.1	2.9 ± 0.1
VNEI	kT_e [keV]	0.58 ± 0.01	0.61 ± 0.01	0.54 ± 0.01
	Mg (solar)	1.2 ± 0.1	1.6 ± 0.2	1.4 ± 0.1
	Si (solar)	0.9 ± 0.1	0.9 ± 0.1	1.1 ± 0.1
	S (solar)	0.8 ± 0.1	0.7 ± 0.1	0.8 ± 0.1
	τ [10^{12} cm^{-3} s]	1.8 ± 0.2	1.7 ± 0.3	1.8 ± 0.1
	Norm [ph cm^{-2} s^{-1}]	4.1 ± 0.4	3.1 ± 0.5	3.2 ± 0.9
Al Kα	E [keV]	1.58 (fixed)	1.58 (fixed)	1.58 (fixed)
	σ (keV)	0 (fixed)	0 (fixed)	0 (fixed)
	Norm [10^{-4}ph cm^{-2} s^{-1}]	2.1 ± 0.2	2.2 ± 0.4	2.1 ± 0.1
Si Lyα	E [keV]	2.0 (fixed)	2.0 (fixed)	2.0 (fixed)
	σ (keV)	0 (fixed)	0 (fixed)	0 (fixed)
	Norm [10^{-4}ph cm^{-2} s^{-1}]	4.9 ± 0.5	3.8 ± 0.3	3.9 ± 0.2
S Lyα	E [keV]	2.6 (fixed)	2.6 (fixed)	2.6 (fixed)
	σ (keV)	0 (fixed)	0 (fixed)	0 (fixed)
	Norm [10^{-4}ph cm^{-2} s^{-1}]	3.6 ± 0.2	3.1 ± 0.3	2.9 ± 0.2
RRC H-like Si	E [keV]	2.666 (fixed)	2.666 (fixed)	2.666 (fixed)
	Norm [10^{-4}ph cm^{-2} s^{-1}]	5.2 ± 0.3	4.3 ± 0.6	4.1 ± 0.3
RRC H-like S	E [keV]	3.482 (fixed)	3.482 (fixed)	3.482 (fixed)
	Norm [10^{-4}ph cm^{-2} s^{-1}]	4.4 ± 0.5	3.7 ± 0.4	3.6 ± 0.2
	χ^2/d.o.f	860/717=1.2	452/361.6=1.25	301/251=1.2

Table 3.3: Best-fit spectral parameters of 3C 391 with corresponding errors at the 90% confidence level in the 1.0 − 5.0 keV band for an absorbed VNEI and RRC models for three regions shown in Figure [3.6]

.

the synchrotron radio spectrum inefficient to explain the observed radio fluxes. In the case of IC emission process, total energy has to be $\sim 10^{51}$ erg to account for the observed spectrum. This means that almost all the energy released during the SN explosion has been transferred to the relativistic electrons, which is very unlikely. Moreover, the magnetic field needs to be ≤ 1 μG to explain the radio data. Additionally, density of the ambient matter has to be ~ 0.3 cm^{-3} to reduce the bremsstrahlung component, which will be inconsistent with our measured value of 387 cm^{-3}.

The total gamma-ray luminosity was found as L = 1.34 $\times 10^{36}$ erg s^{-1}, similar to the first GeV-emitting SNRs that were discovered by Fermi-LAT, e.g. IC443 [128], W51C [130], W44 [131], and W49B [132], all of which are MC interacting MM SNRs with gamma-ray luminosities higher than 10^{35} erg s^{-1}.

Gamma-ray emission model in 3C 391

There are mainly two scenarios describing how hadronic gamma rays are produced in SNRs. The 'crushed cloud' scenario describes the hadronic gamma rays as a product of interactions between the MC, compressed and shocked by the passage of the blast-wave of the SNR, and the relativistic protons inside the shocked MC. Thus γ-photon emission region coincides with proton acceleration region. This is depicted in figure [3.8(a)]. The relativistic protons can be either reaccelerated cosmic rays or freshly accelerated protons entering the radiatively compressed MC region. In this scenario since the crushed clouds are thin, multi-GeV particles can escape from the shocked MC, which might be the reason of seeing a break in the proton spectrum [182, 183].

In the 'escaped cosmic rays' scenario, energetic protons escape from the acceleration region and interact with nearby unshocked MC. This p-p interaction produce π°-

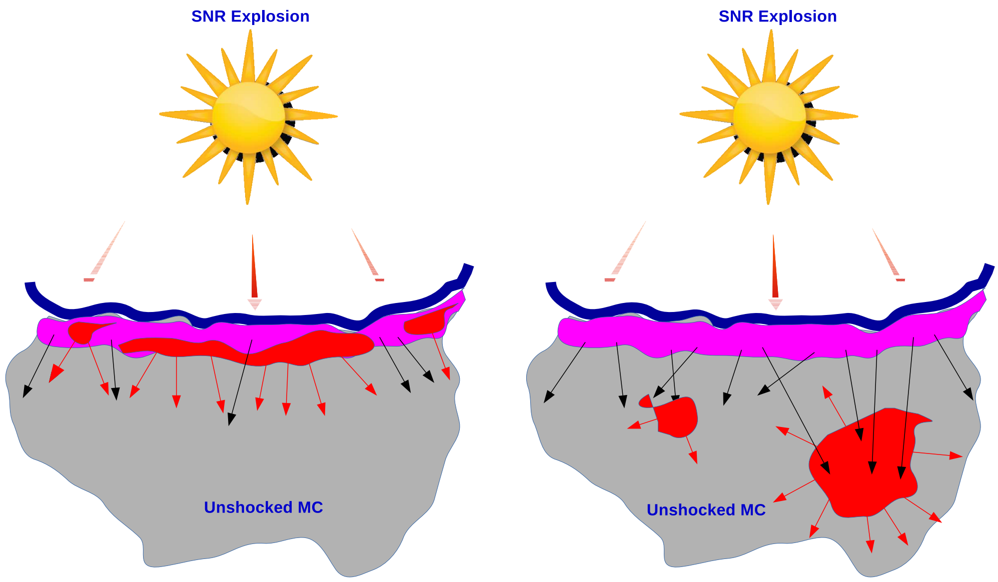

(a) **(b)**

Figure 3.8: Two different hadronic γ photon emission scenarios from SNR-MC interaction are depicted here. The thick blue curve and the light gray colored area represent the supersonic blast wave from SN explosion and unshocked MC respectively. The pink color represents the proton acceleration region i.e. the shocked and compressed MC due to the interaction of SNR shock front. The red colored region and red arrow represent the p-p collision region and emitted γ-photon. The black arrow represents the escaped protons from acceleration region. **(a)** represents the crushed cloud scenario. **(c)** represents the escape cosmic ray scenario.

decay gamma rays. This situation is schematically depicted in figure [3.8(b)]. For this scenario to happen, there must be GeV/TeV sources found outside the radio shell of 3C 391 that could produce these escaping protons [184]. But there are no nearby cosmic ray sources to 3C 391 and all other sources were taken into account in the gamma-ray background model.

The reason why the spectral break of protons is at $\sim$ 12 GeV for 3C 391 could be that relativistic particles are escaping from their acceleration sites, the shell of the SNR or the crushed MC, when the shell is expanding into the rarefied ISM during the earlier epochs of the SNR. Since particles at very high energies ($\sim$ TeV) can only be confined during the early stages of the SNR evolution, and because 3C 391 is a middle-aged SNR, most of the very high energy particles must have already escaped from the shell [183]. The interactions between the SNR and MC, which are evident by the OH masers [26], can enhance loss of the energetic particles. The part of the shock energy is used to pump the maser radiation. Alternatively, the SNR shock expanding in dense medium can be slowed down by the dense MC shifting the maximum particle energy to the GeV region [185]. Assuming the BPL spectrum of protons without any spectral cutoff, we estimate that the differential flux of gamma rays at 1 TeV is $\sim 0.06\%$ of Crab nebula flux. TeV observations of this source with the upcoming Cherenkov Telescope Array (CTA) may provide more robust constraints of the various parameters of the input proton spectrum.

X-ray emission model in 3C 391

The massive progenitor star of 3C 391 inside an MC exploded and the shock waves expanded in the dense MC breaking out into a more rarefied ISM in the SW region, where most of the very high energy particles escaped causing a break in the proton spectrum. This 'break-out' scenario could also be an explanation for observing recombining plasma in 3C 391. Using *Suzaku* data we discovered RRC of H-like Si and S at ~ 2.7 and ~ 3.5 keV from the spectrum.

We chose three regions to do X-ray spectral analysis, to compare the kT$_e$ values in different regions of 3C 391: the whole SNR, the NW region, and the SE region (Figure [3.6]). We chose the NW and SE regions to check if there is any temperature gradient across the SNR. Finding a temperature gradient would be sign for electron cooling through thermal conduction mechanism. The NW region is closer to the site of denser molecular material, where the molecular density drops gradually toward the SE of 3C 391 [150]. This is a good region to test the thermal conduction scenario of the RP. The SE region includes two OH maser spots; an indication that the SNR shell is breaking out of the MC and into the rarefied ISM [26]. By choosing this region, we aim for checking the adiabatic cooling scenario over ionized plasma. When we compare the kT_e values of these regions, we found kT_e for NW and SE region to be $\sim$ 0.61 keV and $\sim$ 0.54 keV, respectively. Since these values are very close to each other it is not possible to determine which cooling mechanism is dominating.

Analyzing X-rays from the whole remnant and assuming a distance of 7.2 kpc for 3C 391 [[**?**]], we calculated the electron density $n_{\rm e}$ as ~ 0.82 cm^{-3} from the emission measure ($EM = n_{\rm e}n_{\rm H}V$, where $n_{\rm H}$ is the hydrogen density and V is the volume of the X-ray emitting plasma). Then, from the relation $\tau/n_{\rm e}$, we found the age of 3C 391 as $\sim 69,000$ yr using the best-fit τ value ($\sim 1.8 \times 10^{12}$ cm^{-3} s) of VNEI plus RRC model, higher than the SNR age found by *Chandra* [153].

The possible origin of the RP found in NW region might be due to the hot electrons getting in contact with cooler and denser MC impeding the expansion of the SNR shell. In the SE region of 3C 391, it is possible that the RP formed when SN blast wave expanded into the rarefied ISM and caused the electron temperature to drop through the adiabatic cooling mechanism. Both of these cooling mechanisms might have worked together in different regions of the SNR to produce RRC in 3C 391. To understand which scenario dominates in which part of 3C 391, detailed over-ionization maps need to be produced, as it is done for W49B [186].

CHAPTER 4

Search for VHE gamma-photon emission from unassociated HAWC sources

In this chapter, we describe a multi-telescope collaborative campaign in searching for HE and VHE gamma-ray emission from three High Altitude Water Cherenkov (HAWC) [2.4.2] detected sources which have no previous counterparts in other wavelength regimes. This chapter is mainly devoted in the exploration of unassociated sources spectrum in different energy regimes. In the first part, we describe the observations and corresponding source characteristics, measured by HAWC collaboration. The second part of this chapter is focused into the detailed description of MAGIC and Fermi-LAT data analysis of these sources. The analysis resulted in a non detection and ended up with upper limit estimation of the photon flux. Finally we represent different possible scenarios which can explain this non detection in other energy ranges. This chapter is primarily based on the work, named as *MAGIC and Fermi-LAT gamma-ray results on unassociated HAWC sources* which was published in *Monthly Notices of the Royal Astronomical Society* on 2019 [187][arXiv:1901.03982]. In this work, I have participated in the detailed analysis of the data from the MAGIC telescopes on two HAWC sources i.e. 2HWC J2006+341 and 2HWC J1907+084*.

Introduction and motivation

The different detection techniques, as described in *chapter 2*, of present day gamma-ray astronomy provide an unique opportunity to explore the universe over a wide energy range from a few tens of MeV to hundreds of TeV. The study of a source spectrum over this broad energy band can only be accomplished with a collaborative effort of different instruments operating at different energies. This is the first such collaborative work of different gamma-ray observatories to explore the characteristics of some unidentified sources over a wide energy range. In this campaign, the lower energy spectrum i.e. MeV to GeV range is covered with space based detector, Fermi-LAT which operates in scanning mode with a high duty cycle and large FoV. The IAC technique, most sensitive to explore γ-ray sources $>$ 100 GeV to several tens of TeV, is exploited by the MAGIC telescopes. The low threshold energy ($\sim$ 50 GeV) of MAGIC provides an effective overlap with Fermi-LAT observation. The high energy part of spectrum up to 100 TeV is covered with water Cherenkov technique of HAWC observatory.

The large effective area, high duty cycle and wide FoV make HAWC an optimal instrument to perform survey studies on multi-TeV sources. After an initial survey study, HAWC has published two catalogs of TeV sources: 1HWC for sources in the inner Galactic plane using 275 days of data with a configuration of approximately one-third of the full array (HAWC-111; [188]), and 2HWC for almost the entire sky using 507 days of the completed HAWC detector [189]. The second catalog improves over the first with respect to exposure time, detector size and angular resolution, resulting in a significant improvement in sensitivity. As done for the previous catalog, 2HWC data was analyzed using a binned likelihood method [190].

Likelihood is a function of parameters of some statistical model which is defined as the probability of obtaining a given observed outcome from some definite values of parameter of the model. In case of HAWC analysis, the statistical model includes a source model i.e. spectral and spatial description of all known sources in the sky and a model of the detector response as a function of PSF, angular resolution etc. The parameters of source model can be optimized by maximizing the likelihood function so that source model with these optimized parameter values can fit the observed data. The optimization of detector response parameters can be done with the data of standard source like Crab Nebula. In usual source discovery, two hypothesis are assumed; one is null hypothesis with no new source and an alternative hypothesis with the assumption of the existence of a new source at a particular location. To compare the effectiveness of these hypotheses in explaining the observed data, test statistics (TS) i.e. ratio of likelihood function values using both hypothesis is used and this is defined as

$$TS = 2 \ln \frac{L(\text{Alternative hypothesis;N}_{obs})}{L(\text{Null hypothesis;N}_{obs})} \tag{4.1}$$

where L and N_{obs} represent the likelihood functions and the total observed counts of specific observation respectively. The square root of test statistics value i.e. $\sqrt{TS}$ is interpreted as the significance of excess counts in unit of 'Gaussian sigma'.

In case of 2HWC analysis, HAWC used two different source approaches. In the first approach, the source model is characterized by point-like morphology with power-law spectrum, $\mathrm{d}N/\mathrm{d}E = N_0 \left(\frac{E}{E_0}\right)^{-\Gamma}$ (with N_0 the normalization, E_0 the pivot energy and Γ the spectral index), with spectral index $\Gamma = 2.7$. The second approach is characterized by extended source morphology modeled as a uniform disk of 0.5 deg, 1 deg and 2 deg in radius and spectral index $\Gamma = 2.0$. The total number of sources identified in this catalog was 39, of which 19 were not associated with any previously reported TeV source within an angular distance of 0.5 deg. All 2HWC sources presented a test statistic (TS) above 25 (equivalent to a pre-trial significance of $\sim 5\sigma$).

The 2HWC catalog motivated follow-up studies with H.E.S.S. [191], VERITAS [192] and also MAGIC and *Fermi*-LAT. In this work, we focused on the 19 sources with no high-energy (HE; $E \gtrsim 10$ GeV) or very-high-energy (VHE; $E \gtrsim 300$ GeV) association, in order to provide new multi-wavelength information of candidates without a lower energy counterpart. After evaluating those sources, a short list of three targets was selected: 2HWC J2006+341 (RA = 301.55 deg, Dec = 34.18 deg), 2HWC J1907+084* (RA = 286.79 deg, Dec = 8.50 deg) and 2HWC J1852+013* (RA = 283.01 deg, Dec = 1.38 deg). In order to check the detection probability of these sources with MAGIC telescope, we have extrapolated source spectrum, provided in second HAWC catalog, over MAGIC observation range and comparison with MAGIC sensitivity curve to ensure the detection. These sources were specially chosen because they lie in the FoV of previous MAGIC observations, allowing MAGIC to analyze these sources without performing new dedicated observations.

Even though the HAWC spectra of each source were determined using a likelihood fit, the 2HWC catalog did not use a likelihood method to describe multiple sources simultaneously. In the 2HWC catalog, the asterisks of 2HWC J1907+084* and 2HWC J1852+013* indicate that the sources were near another source with larger significance and thus their characterization may be influenced by neighboring sources. 2HWC J2006+340, 2HWC J1907+084* and 2HWC J1852+013* were detected in the point source search with significances of 6.10σ, 5.80σ and 8.50σ, respectively. The corresponding photon index and flux normalization values obtained in the 2HWC catalog [189] are listed in Table [4.1]. The corresponding energy range presented in table is computed with a dedicated HAWC analysis [189].

In HAWC, detected events are classified by size in nine analysis bins, depending on the fraction f_{hit} of photomultiplier tubes in the array that participate in the reconstruction of the air shower. The likelihood analysis in HAWC is computed over f_{hit} bins, which can be considered an energy estimator. However, the f_{hit} bins

HAWC source 2HWC	RA [°]	Dec [°]	l [°]	b [°]	1σ stat. error [°]	Photon index	Flux normalization [$\times 10^{-15}$ TeV^{-1}cm^{-2}s^{-1}]	Energy range [TeV]
J2006+341	301.55	34.18	71.33	1.16	0.13	2.64 ± 0.15	9.6 ± 1.9	1 – 86
J1907+084*	286.79	8.50	42.28	0.14	0.27	3.25 ± 0.18	7.3 ± 2.5	0.18 – 10
J1852+013*	283.01	1.38	34.23	0.50	0.13	2.90 ± 0.10	18.2 ± 2.3	0.4 – 50

Table 4.1: Coordinates, photon index, flux at the pivot energy (7 TeV) and energy range for the analyzed sources. Values are provided in the 2HWC catalog, except for the energy range, which was obtained in a dedicated analysis. Only statistical uncertainties are shown. Based on a study of the Crab Nebula by HAWC [28], the systematic uncertainty can be divided into several components: 0.10 deg in angular resolution, 0.2 in photon index, and 50% in flux normalization.

depend strongly on the declination and spectral hardness of each source, and so does this f_{hit}/energy correlation. The energy range is then given as a constraint on the photon distribution as a function of f_{hit} for each separate source. Following [189], the energy range has been chosen as the boundaries within which the events contribute to the 75% of the TS value.

Search for low energy gamma photons

The characterization of HAWC detected dark sources into different types of known galactic components requires proper information about source spectrum over wide energy range. This knowledge also helps to reveal the possible emission mechanisms in different wave bands. To explore dark source characteristics in lower gamma-photon region (i.e. hundreds of MeV to hundreds of GeV range), we have decided to analyze both Fermi-LAT and MAGIC data for these three sources. The details of the analysis methods are described in later part of this section.

Fermi-LAT data analysis

For this work, Fermi-LAT data analysis has been done with 8.5 years data taken in the period between August, 2008 and February 2017. The events-data was taken from a circular region of interest (ROI) with a radius of 10^0 centered at the position of each HAWC sources. The good quality data are selected using *gtselect* of Fermi Science Tools (FST) based on Fermi-LAT `Pass 8` SOURCE photon reconstruction algorithm. The `Pass 8` data offers two primary benefits for the study of HE gamma-ray sources: a greater acceptance compared with previous LAT reconstructions and an improved PSF with a 68% containment angle less than 0.2 deg above 10 GeV that is nearly constant with increasing energy [193]. To prevent event contamination at the edge of the field of view caused by the bright gamma rays from the Earths limb, we cut out the gamma rays with reconstructed zenith angles greater than 105^0. For each source of interest, we analyze data in energy range between 10 GeV and 300 GeV using the standard binned likelihood framework ,based on *gtlike*, provided by the Fermi Science Tools (v10r01p01). Data within ROI were binned into 8 logarithmic energy bins per decade and a spatial bin size of 0.05°. For the binned likelihood analysis [161], the matching energy dependent exposure maps were produced based on pointing direction, orientation, orbit location, and live-time accumulation of LAT. The detail of Fermi-LAT likelihood analysis is explained in *chapter 3*.We used the standard background model which includes known point source and diffuse background model. The standard diffuse background model has two components: the diffuse Galactic emission ($gll\_iem\_v06.fits$) and the isotropic component ($iso\_P8R2\_SOURCE\_V6\_v06.txt$), which is a sum of the extragalactic background, unresolved sources, and instrumental background.[1].

We did not extend our analysis to lower energies for two primary reasons: for any HAWC source to be detected at lower energies, it must be detectable at > 10 GeV with the LAT, unless the HAWC and LAT emission is produced by a different component; and this high-energy cut suppresses photons from gamma-ray pulsars and Galactic diffuse emission in the plane. As a source model for this analysis we use the Third Catalog of Hard *Fermi*-LAT Sources for point sources [194] and the

[1]For more details, please see: http://fermi.gsfc.nasa.gov/ssc/data/access/lat/BackgroundModels.html

Fermi Galactic Extended Source (FGES) catalog for extended sources [195].

Using ~ 8.5 years of `Pass 8` data, we search for new sources separately with both point-like or extended source morphology at the location of the HAWC candidate. The spectrum of the source is modeled as a simple power law. After initially fitting a putative point source at the HAWC position, the position is re-localized. The normalization parameter of other sources within 5^0 are left as free parameters in the fit. To search for a possible extended source, we use a uniformly illuminated disk with a radius of 0.2 deg as the initial spatial model. The $fermipy$ package [196] fits both the radius and centroid of the possible extended source. If a statistically significant source is not found, ULs at the position of the 2HWC source are computed at 95% confidence level (CL) using a Bayesian method. The assumed spectral indices are 2.0, 3.0 and the index reported in the 2HWC catalog (see Table 4.1). Extended source ULs are computed assuming a radius of 0.16 deg, for comparison with the limits placed by MAGIC.

MAGIC data analysis

The analysis presented here is performed using the standard MAGIC analysis software `MARS` [115] which takes the raw data (FADC count stored in DAQ) as input and produces high level data. This high level data contains the direction and energy information of incoming photons. This analysis process follows a long analysis chain as described in *chapter 2*. The detection significance is computed using the Gaussian approximation of Equation [2.3.6.7] of *chapter 2*. The differential and integral flux upper limits (ULs) are calculated using algorithm explained in *chapter 2* with a confidence level (CL) of 95%, assuming a Poissonian background and a total systematic uncertainty of 30%.

As mentioned above, these analyzed sources were included in the FoV of former

HAWC source	W1		W2		W3		W4	
2HWC	Distance [deg]	t_{total} [h]	Distance [deg]	t_{total} [h]	Distance [deg]	t_{total} [h]	Distance [deg]	t_{total} [h]
J2006+341	0.5	16.0	0.9	14.0	0.4	16.3	1.0	14.8
J1907+084*	0.5	1.0	1.2	1.0	0.7	1.3	1.1	0.9
J1852+013*	1.1	30.8	0.7	28.8	1.2	29.6	0.6	27.5

Table 4.2: Distance in degrees between the four MAGIC wobble pointing positions (W1, W2, W3 and W4) and the selected 2HWC sources. The total time after data quality cuts, in hours, achieved by MAGIC in each case is also shown.

MAGIC observations. These archival data were taken using the false-source tracking mode, or *wobble-mode* where the telescopes point at four different positions located 0.4 deg from the nominal source position, which allows us to evaluate the background simultaneously with source data (see in *chapter 2*). Since our observations were not dedicated to the 2HWC sources, so their coordinates are shifted from the camera center by different distances other than the standard offset of 0.4 deg (Figure: [4.1]). This requires a dedicated analysis, known as off-centered source analysis. To account for their location in the camera, the background used in the calculation of ULs was evaluated through the *off-from-wobble-partner* (OfWP) method [115]. In this method, background data are taken only from opposite wobble position which is 180^0 away. Thus wobble positions are grouped into two pairs (W1, W2) & (W3, W4) and ON and OFF positions are chosen from the same pair. The distances between the camera center and the 2HWC sources at the four different *wobble* positions are properly summarized in Table [4.2]. The total observation time, after data quality cuts, for each case is also quoted in Table [4.2]. It is worth highlighting that the MAGIC sensitivity depends on the angular offset from the pointing direction. However, after the MAGIC upgrade of 2011–2012, the sensitivity at offset angles larger than 0.4 deg improved considerably as shown by [5]. For the analysis performed in this work, and given the range of angular offsets for all the candidates, the sensitivity remains between $\sim 0.6 - 1.0$ % CU.

Observations of 2HWC J1852+013* were carried out entirely under dark conditions, i.e. in absence of moonlight. On the other hand, 2HWC J2006+341 and 2HWC

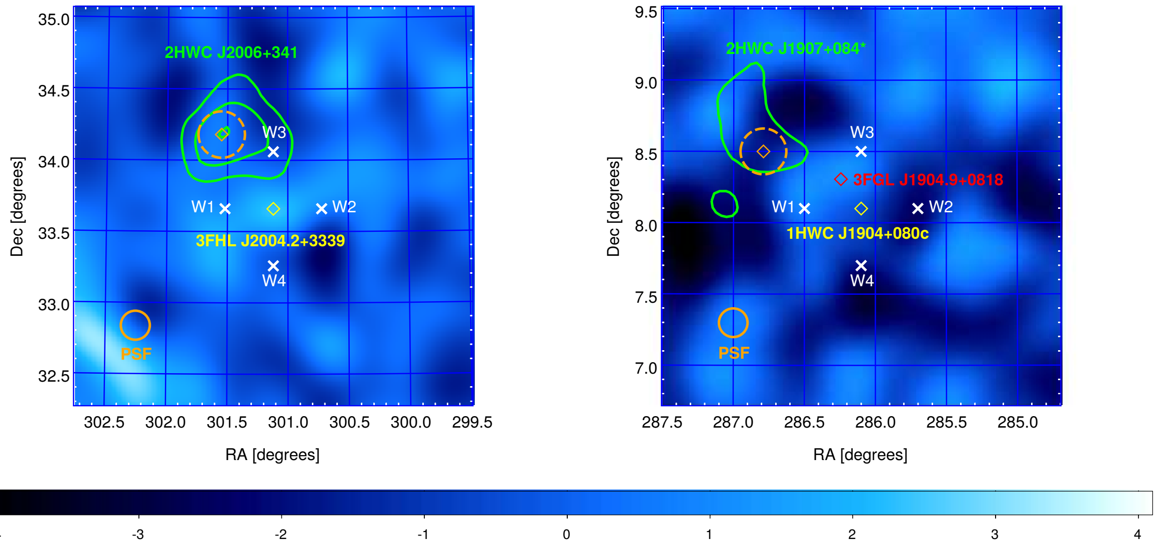

Figure 4.1: MAGIC significance skymaps for the FoV of 2HWC J2006+341 and 2HWC J1907+084*, searching for sources of ~ 0.16 deg radius. The four different *wobble* positions, to which MAGIC pointed during the 3FHL J2004.2+3339 and 1HWC J1904+080c observations, are tagged with W1, W2, W3 and W4 in white color. MAGIC PSF is shown in orange at the left bottom in each panel. *Left panel:* Skymap of the observations at the direction of 3FHL J2004.2+3339 (yellow diamond). This FoV contains 2HWC J2006+341 (orange diamond) located at ~ 0.63 deg from the nominal position of MAGIC observations. Centered at the position of 2HWC J2006+341, the orange dashed circle corresponds to the assumed extension of 0.16 deg used for the MAGIC analysis. The HAWC contours (4σ, 5σ and 6σ) are shown as green solid lines. *Right panel:* Skymap for the observations of the 1HWC J1904+080c (yellow diamond) FoV in which 2HWC J1907+084* (orange diamond) is enclosed. Dashed orange circle represents the $0.16°$ MAGIC extended assumption, while HAWC contours (at the level of 5σ) are shown as green solid lines. The position of the closest *Fermi*-LAT source, 3FGL J1904.9+0818, is marked as a red diamond.

J1907+084* were observed with nominal high-voltage at background levels ranging between 1 and 8 times the brightness of the dark sky due to different Moon phases (Table [2.1]). The higher moonlight level increases the brightness of night sky background (NSB). The standard Monte Carlo-simulated gamma-ray data would not be sufficient to train the RF algorithm. This requires more complicated non-standard MAGIC analysis [197].

The higher moonlight level affects the pixel trigger rate by increasing the accidental trigger rate. To suppress these spurious data, higher discriminator threshold (DT) has been applied. Higher background also increases signal fluctuation. Thus mean and RMS of pedestal charge distribution would be different for different moonlight condition. The charge threshold of image cleaning process, performed in `star` operation, depends on mean and RMS of pedestal distribution. This requires different cleaning thresholds for moon data. Following the prescription of [197], MAGIC data are divided in three categories:

- Dark data (M1 DC $< 2\ \mu$A) standard cleaning
- Moderate moon data (2 μA <M1 DC< 4 μA) Mean: 3.0 phe, RMS: 1.3 phe
- Descent moon data (4 μA <M1 DC< 8 μA) Mean: 4.1 phe, RMS: 1.7 phe

Moon data analysis has started from `star` level and based on M1 DC value appropriate data cleaning is required. In γ/Hadron separation, MC simulated gamma-ray events are required which can mimic exactly the actual observational condition. To include the extra fluctuation due to moon light condition, artificial noise has been added to MC data in `star` level through *MAddNoise* option. In both RF training process and `flute` operation, these tuned MC data has been used. All these above mentioned steps has been performed individually for each moonlight level. To produce a single spectrum, flute outputs of all these moonlight data are combined through `foam` operation of `MARS` software. foam produces the average spectrum. It just adds up all the event statistics to obtain the overall excess in each bin of estimated energy. Then it adds all the exposures (vs. E_{est}), i.e. the product of each sample's effective time and the effective area A'(E_{est}), The average spectrum is then obtained by dividing the excesses by the exposures.

Since the HAWC sources each have a maximum significance in the point-source HAWC maps, they may be point-like sources for MAGIC as well. Therefore, we analyze the candidates under two hypotheses: we assume that the sources are point-like for MAGIC (point spread function; PSF $\lesssim 0.10$ deg, beyond a few hundred GeV) or are extended with a radius of 0.16 deg. Larger extensions cannot be adopted due to the OfWP method and the standard 0.4° offset applied in the *wobble* pointing mode, because the expected region of gamma-ray emission from the 2HWC source and the background regions selected to compute flux ULs would overlap.

Observation and results

In the following section, we describe the different regions of the sky that contain the three selected sources, along with the corresponding observations and results. MAGIC differential ULs are listed in Table [4.3], while *Fermi*-LAT integral ULs (above 10 GeV) are described in Table [4.4] for both point-like and extended hypotheses. Figure [4.1 presents the MAGIC significance skymaps for 2HWC J2006+341 and 2HWC J1907+084* assuming an extended source with a 0.16° radius. The flat significance field displayed in all skymaps is compatible with background in the entire FoV. The multi-wavelength spectral energy distribution (SED) for each 2HWC source is presented in Figure [4.3].

2HWC J2006+341

2HWC J2006+341 is in the FoV (at $\sim 0.63°$) of the compact radio/optical nebula G70.7+1.2, which is thought to be powered by a pulsar/binary system interacting with a surrounding molecular cloud. An unidentified source, 3FHL J2004.2+3339, was detected at the position of this putative binary system. Therefore, VHE gamma-ray emission from the G70.7+1.2 region could be expected due to the interaction between the pulsar wind with both the stellar wind of the companion star and the molecular cloud.

MAGIC observed 3FHL J2004.2+3339 with an extended range of zenith angles from

5 deg to 50 deg. The total data sample amounts to ~ 61 hours of good quality data from April 2015 to August 2016. No significant signal is found in the direction of 2HWC J2006+341 as either a point-like or extended source. In order to calculate the integral flux ULs, MAGIC adopts a power-law distribution with photon index $\Gamma = 2.64$, following the HAWC results. Under point-like assumption, the integral UL, computed at 95% CL for energies greater than 300 GeV, is 4.0×10^{-13} photons $\mathrm{cm}^{-2}\mathrm{s}^{-1}$, while for 0.16 deg radius, it increases to 3.3×10^{-12} photons $\mathrm{cm}^{-2}\mathrm{s}^{-1}$. On the other hand, the integral UL for a point-like source in the direction of 3FHL J2004.2+3339 is 4.3×10^{-13} photons $\mathrm{cm}^{-2}\mathrm{s}^{-1}$ for energies above 300 GeV and assuming a power-law index of 2.6. In the GeV regime, no known *Fermi* catalog source is found to be coincident with 2HWC J2006+341. The closest *Fermi*-LAT source is the already mentioned 3FHL J2004.2+3339 (coincident within the errors with 3FGL J2004.4+338, [95]). This source has been searched extensively for pulsations [198]. Using the analysis method described in previous section,no significant (TS $\geq$ 25) source is detected using either the point or extended source models.

2HWC J1907+084*

2HWC J1907+084* is located at ~ 0.79 deg from 1HWC J1904+080c, included in the first HAWC survey. 1HWC J1904+080c was detected with a pre-trial significance of 5.14σ, which motivated MAGIC follow-up observations. The coordinates were not coincident with any known TeV source, although it was close (at 0.3 deg) to a *Fermi*-LAT gamma-ray hotspot ($< 5\sigma$), 3FGL J1904.9+0818 [95]. Nevertheless, its significance was only $\sim 4\sigma$ after trials in the published 1HWC catalog [188].

MAGIC performed observations in the direction of 1HWC J1904+080c over 6 non-consecutive nights from May 10, 2015 to May 19 2015. After rejecting the data affected by non-optimal weather conditions, the total amount of time reached in this FoV was 4.20 hours. The region was observed at medium zenith angles from

30 deg to 50 deg. No excess is found during the analysis of 2HWC J1907+084* data. The 95% CL integral ULs for $E > 300$ GeV and index $\Gamma = 3.25$ are 2.8×10^{-12} photons $\mathrm{cm}^{-2}\mathrm{s}^{-1}$ and 4.6×10^{-12} photons $\mathrm{cm}^{-2}\mathrm{s}^{-1}$ for the point-like and extended hypotheses, respectively. MAGIC does not find any significant excess at the position of 1HWC J1904+080c either, which leads to an integral flux UL for energies greater than 300 GeV of 4.1×10^{-12} photons $\mathrm{cm}^{-2}\mathrm{s}^{-1}$, assuming a power-law spectrum of $\Gamma = 2.6$. From the *Fermi*-LAT, the `Pass 8` analysis yields no significant emission in the direction of 2HWC J1907+084*, either during the point-like or the extended analysis.

2HWC J1852+013*

2HWC J1852+013* is located in the FoV of the W44 SNR, as well as in the FoV of the established VHE sources HESS J1858+020 and HESS J1857+026 (subdivided in 2 emission sites MAGIC J1857.2+0263 and MAGIC J1857.6+0297; [199]). The region was thus extensively observed by the MAGIC collaboration. 2HWC J1852+013* is also located at 0.56 deg away from 3FGL J1852.8+0158, which is classified as a probable young pulsar using machine learning techniques [200].

The dataset used by MAGIC here comprises approximately 120 hours of dark quality data, taken from April 2013 to June 2014, with a span in zenith range from 25 deg to 50 deg. MAGIC does not find any excess in the direction of 2HWC J1852+013*. Adopting $\Gamma = 2.90$, the constraining 95% CL integral ULs are 3.8×10^{-13} photons $\mathrm{cm}^{-2}\mathrm{s}^{-1}$ for the point-like search and 1.7×10^{-12} photons $\mathrm{cm}^{-2}\mathrm{s}^{-1}$ for the extended search. Specific background selection using OfWP was applied in this case, ensuring that no background control region overlaps with any of the several VHE emitting sources in the FoV. As per the previous sources, ULs are given for $E > 300$ GeV. Neither cataloged nor new sources from the `Pass 8` analysis arises in the *Fermi*-LAT analysis of 2HWC J1852+013*.

Energy range [GeV]	2HWC J2006+341		2HWC J1907+084* [photons cm^{-2}s^{-1}]		2HWC J1852+013*	
	Point-like	Extended	Point-like	Extended	Point-like	Extended
139.2 – 300.0	2.6×10^{-11}	6.2×10^{-11}	7.1×10^{-11}	3.1×10^{-10}	1.7×10^{-11}	4.6×10^{-11}
300.0 – 646.3	1.4×10^{-12}	1.0×10^{-11}	8.0×10^{-12}	1.7×10^{-11}	8.6×10^{-13}	4.9×10^{-12}
646.3 – 1392.5	2.5×10^{-13}	1.3×10^{-12}	2.5×10^{-12}	2.3×10^{-12}	9.0×10^{-14}	3.9×10^{-13}
1392.5 – 3000.0	6.0×10^{-14}	9.9×10^{-14}	1.7×10^{-13}	1.0×10^{-12}	6.7×10^{-14}	1.2×10^{-13}
3000.0 – 6463.3	1.8×10^{-14}	2.7×10^{-14}	–	1.4×10^{-13}	7.6×10^{-15}	1.3×10^{-14}
6463.3 – 13924.8	–	9.5×10^{-15}	–	1.3×10^{-14}	1.1×10^{-14}	5.5×10^{-14}

Table 4.3: MAGIC differential ULs (at 95% CL) for 2HWC J2006+341, 2HWC J1907+084* and 2HWC J1852+013* assuming a power-law spectrum with spectral index of $\Gamma = 2.64$, 3.25, and 2.90, respectively. ULs for both point-like ($\lesssim 0.10$ deg) and extended (~ 0.16 deg radius) assumptions are shown in each case. Due to low statistics, ULs at the highest energy ranges are not always computed for 2HWC J2006+341 and 2HWC J1907+084*

	$\Gamma_{\rm HAWC}$		Γ=2.0		$\Gamma = 3.0$	
	Point-like	Extended	Point-like	Extended	Point-like	Extended
	[$\times 10^{-11}$ photons cm^{-2}s^{-1}]		[$\times 10^{-11}$ photons cm^{-2}s^{-1}]		[$\times 10^{-11}$ photons cm^{-2}s^{-1}]	
J2006+341	2.4	4.4	2.3	4.7	2.4	4.2
J1907+084*	3.1	3.1	2.7	2.7	3.2	3.2
J1852+013*	2.1	3.7	2.0	3.3	2.0	3.7

Table 4.4: *Fermi*-LAT 95% CL flux ULs, above 10 GeV, assuming point-like source and extended source a radius of 0.16°.

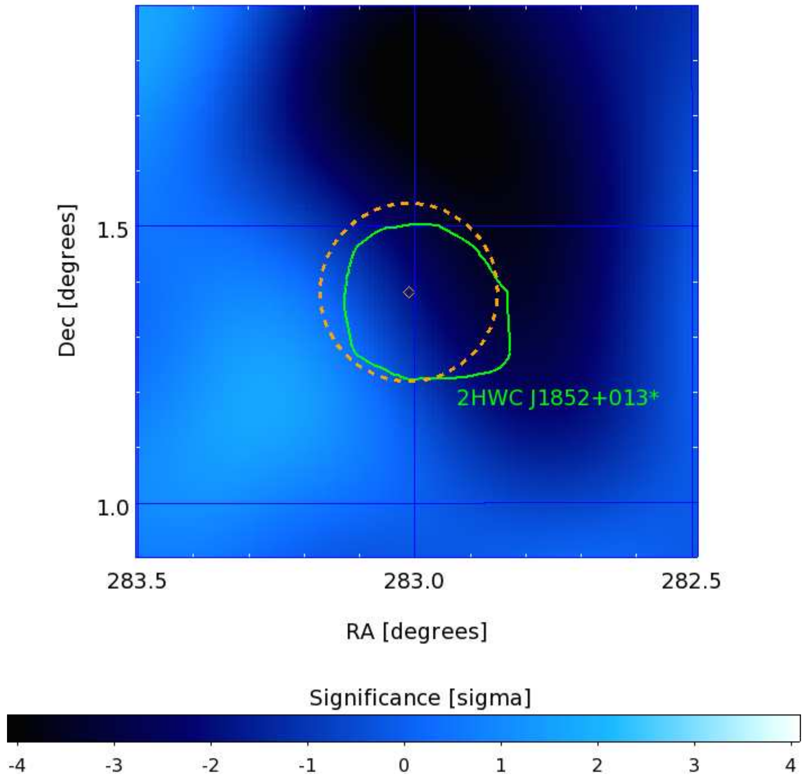

Figure 4.2: 1°× 1° MAGIC significance skymap, looking for 0.16° extended sources around 2HWC J1852+013*, whose position is depicted as an orange diamond. Dashed orange circle shows the extension of 0.16° analyzed by MAGIC, whilst the green solid line corresponds to the 8σ HAWC contour.

Search for known associated sources around HAWC source positions

Given that the largest population of TeV emitters in our Galaxy are pulsar wind nebulae (PWNe) [201], the selected candidates may be expected to be this source type. However, the lack of a detection by either MAGIC or *Fermi*-LAT complicates the identification of these sources. In order to investigate their possible PWN nature, we look for detected pulsars near these 2HWC sources using the ATNF catalog[2] [202].

[2]http://www.atnf.csiro.au/people/pulsar/psrcat/

According to the characteristic ages of the pulsars around the three selected 2HWC sources (all above a few tens of kyr), if these pulsars had high initial kick velocities, they could now be significantly offset from their initial positions and have left behind an old PWN with no compact object powering it. In this case, the pulsar position is shifted from the PWN, and without injection of magnetic flux, the nebula's emission is expected to be dominated by inverse Compton(IC).

PSR J2004+3429 is the closest known pulsar to 2HWC J2006+341 at a separation of 0.40 deg, and is the only one within a 1 deg radius. This pulsar lies at a distance of 10 kpc, displays a spin-down power of $\dot{E} = 5.8 \times 10^{35}$ erg s^{-1} and has a characteristic age of $\tau = 18$ kyr. Although energetic enough to power a TeV PWN (see [203]), the distance between 2HWC J2006+341 and PSR J2004+3429 makes this connection improbable: given the characteristic age of 18 kyr, an offset of 0.40 deg ($\sim$ 70 pc) could only be explained with an improbably large kick velocity for the pulsar of $\sim$ 4000 km s^{-1}. The mean 2-D speed for both young and old ($<$ 3 Myr) pulsars was determined to be only 307 ± 47 km s^{-1} by [204] with a study involving a subsample of $\sim$ 50 pulsars' proper motion. The offset may be cosiderably less when considering HAWC systematic and statistical errors on the 2HWC source location of $0.40\,\mathrm{deg} \pm 0.10\mathrm{deg}_{syst} \pm 0.13\mathrm{deg}_{stat}$. Assuming the most constraining possible value, 0.24 deg, the necessary kick velocity would decrease to $\sim$ 2300 km s^{-1}. This value is not far away from the fastest known pulsar at $\sim$ 1500 km s^{-1} [204], though that value is also uncertain given the distance model applied. The highest speed for a pulsar with a well-measured distance is only 640 km s^{-1} [203]. Therefore, we conclude that it is unlikely that PSR J2004+3429 is directly responsible for the emission detected by HAWC. On the other hand, [205] evaluated the probability of random association between 15 2HWC sources and their nearby pulsars, including 2HWC J2006+341 and PSR J2004+3429. For this case, they obtained a chance overlap of only 8% (assuming a source extension of 0.9° as provided in the 2HWC catalog by assigning the halo-like structures visible in the residual skymaps to 2HWC J2006+341, which presents its own uncertainties).

There are two pulsars within 0.50 deg of 2HWC J1907+084*: PSR J1908+0833 at 0.30 deg, and PSR J1908+0839 at 0.33 deg. The former is located at a distance of $\sim$ 11 kpc, with a characteristic age of τ = 4.1 Myr and a spin-down power of $\dot{E} = 5.8 \times 10^{32}$ erg s^{-1}. The very low spin-down power and old age make it unlikely to be currently powering a TeV PWN. Alternatively, PSR J1908+0839, at 8.3 kpc and with a characteristic age of τ = 1.2 Myr, is more energetic with $\dot{E} = 1.5 \times 10^{34}$ erg s^{-1}, so a relation between this pulsar and the 2HWC source cannot be initially ruled out. As done for 2HWC J2006+341, we calculate the kick velocity for the pulsar, now with an offset of 0.33 deg and a characteristic age of 1.2 Myr. The obtained velocity is $\sim$ 40 km s^{-1}, which is low relative to the average kick velocity observed through proper motion studies but remains to be a valid possibility (see Figure 4b from [204]). This velocity stays within the young pulsars' 2-D speed distribution even considering HAWC uncertanties (0.33 deg $\pm$ 0.10deg$_{syst}$ $\pm$ 0.27deg$_{stat}$). We can compare PSR J1908+0839 with the pulsar hosted by Geminga, a well-known TeV PWN detected by Milagro [206] and recently by HAWC [207]. Geminga's pulsar displays a spin-down power of $\dot{E} = 3.25 \times 10^{34}$ erg s^{-1}, very similar to that shown by PSR J1908+0839, but its distance is $\sim$ 30 times smaller ($d_{Geminga}$ = 250 pc). Given the similar spin-down power, the nebula PSR J1908+0839 powers should also have a comparable luminosity with respect to Geminga's PWN, which would lead to a flux around three orders of magnitude smaller than the flux of Geminga and undetectable by HAWC. Therefore, it is unlikely that 2HWC J1907+084* and PSR J1908+0839 are associated with one another.

Finally, the closest pulsar to the source 2HWC J1852+013* is PSR J1851+0118, offset by only 0.10 deg. This pulsar lies at a distance of 5.6 kpc and has a characteristic age of $\sim$ 100 kyr [208]. If both objects are related the required pulsar velocity is a reasonable value of $\sim$ 100 km s^{-1}, though this may be as high as $\sim$ 245 km s^{-1}

when considering the largest offset given by $0.10\,\mathrm{deg} \pm 0.10\mathrm{deg}_{syst} \pm 0.13\mathrm{deg}_{stat}$. However, this pulsar has a relatively low spin-down power, $\dot{E} = 7.2 \times 10^{33}$ erg s^{-1}, which along with its high characteristic age make it unlikely to accelerate particles that can emit gamma rays in the TeV regime. To quantitatively test this scenario, we use the `Naima` software[3] to model the relativistic parent population of the non-thermal gamma-ray emission accounting for different radiative models (see [209]). To obtain the emissivity of the electron population that gave rise to the gamma-ray emission seen by HAWC, we assume that IC is the dominant radiative process and that the electron spectrum is defined by a simple power law. The target photon field for this process is expected to be a combination of cosmic microwave background (CMB) and infrared (IR) photons. The assumed energy densities in each case are standard Galactic values of $u_{CMB} = 0.25$ eV cm^{-3} and $u_{IR} = 0.30$ eV cm^{-3}. With such features, the total energy carried by electrons above ~ 10 TeV needed to explain HAWC detection would be $W_e(> 10\ \mathrm{TeV}) \sim 6.0 \times 10^{46}$ erg.

Alternatively, we consider the cooling time of these electrons (t_{cool}), which is computed as follows [55]:

$$t_{cool} = 3 \cdot 10^8 \left(\frac{E_e}{\mathrm{GeV}}\right)^{-1} \left(\frac{u}{\mathrm{eV/cm^3}}\right)^{-1} \ [\mathrm{yr}] \tag{4.2}$$

where $E_e = 10$ TeV is the electron energy and u is the total energy density of the medium. In this case, we account for IC and synchrotron losses and hence, assuming a temperature of ~ 25 K for the IR photon field [?], u can be described as:

$$u \simeq \frac{B^2}{8\pi} + u_{CMB}\left(1 + 0.01 \cdot \frac{E_e}{\mathrm{TeV}}\right)^{-3/2} + u_{IR}\left(1 + 0.1 \cdot \frac{E_e}{\mathrm{TeV}}\right)^{-3/2} \tag{4.3}$$

where B is the magnetic field. We use the aforementioned energy densities for the CMB and IR photon fields, and for the magnetic field we assume the minimum possible value given by the interstellar magnetic field, $B = 3\ \mu$G, as there is no

[3] naima.readthedocs.org

measured value for the source. Under these assumptions, the cooling time is $t_{cool} \sim$ 57 kyr. Given the spin-down power of PSR J1851+0118, $\dot{E} = 7.2 \times 10^{33}$ erg s^{-1}, the total energy released by the pulsar during the t_{cool} period would be $W'_e \sim 1.3 \times 10^{46}$ erg. Consequently, even assuming that all the energy released by the pulsar was used to accelerate electrons above 10 TeV, there would not be enough energy to power a PWN with the gamma-ray brightness detected by HAWC. According to our model, such a PWN would require an energy injection greater than $\sim 6.0 \times 10^{46}$ erg, which is already higher than W'_e. The low B and u_{IR} used in this calculation of t_{cool} provide maximum values for both t_{cool} and the injected pulsar energy, W'_e. Higher u_{IR} value would produce higher losses and therefore, a smaller W_e. However, an extremely high value for u_{IR} (well above 2 eV cm^{-3}, the IR energy density observed around Cassiopea A and one of the highest for a Galactic TeV source) would be needed to decrease W_e below 10^{46} erg. We do not consider more complex scenarios in which $\dot{E}$ or B change with time. The same parent population study was applied to 2HWC J1907+084* and we reach the same conclusions that corroborated the non-relation with the surrounding pulsars.

MAGIC and LAT ULs also help to constrain our understanding of the spectrum and morphology of these HAWC sources. The SEDs for the three candidate PWNe are shown in Figure [4.3]. MAGIC and *Fermi*-LAT analyses are computed with the photon index provided by HAWC (see Table [4.1]). In the cases of 2HWC J2006+341 and 2HWC J1907+084*, the MAGIC **and LAT** extended ULs are at the level of the HAWC spectrum considering HAWC systematic errors of 0.2 in the photon index and 50% in the flux normalization. However, point-like hypotheses are in contradiction with HAWC results below energies of $\sim$ 4 TeV and $\sim$ 900 GeV, respectively. Therefore, it is expected that these two 2HWC sources are extended, with at least a radius of $\sim$ 0.16 deg. On the other hand, both MAGIC and *Fermi*-LAT results on 2HWC J1852+013* are incompatible with the HAWC spectrum below energies of $\sim$ 10 TeV.

These results can be understood in two ways: 2HWC J1852+013* is much more extended than the assumed radius of 0.16 deg, which would increase MAGIC and *Fermi*-LAT ULs above the flux estimated by HAWC; or the source does not emit in the sub-TeV regime, consistent with the constraining ULs obtained by both MAGIC and the LAT. In the later case, the spectral shaped of 2HWC J1852+013* would have a harder spectrum in the sub-TeV regime, and a minimum energy of around 10 TeV, instead of 400 GeV, should be assumed (see Table [4.1]). To constrain the former case, we calculated LAT ULs for disks of larger radii. For a disk of 1.0 deg radius the LAT UL at energies > 0.2 TeV is within 1σ statistical errors of the measured HAWC flux, extrapolated to lower energies. However, this would also require a harder spectrum in the GeV regime so as to not exceed LAT ULs at lower energies. Additionally, as reported in the 2HWC catalog [**?**], there may be a significant contribution from diffuse galactic emission at the location of 2HWC J1852+013* to which HAWC would be sensitive and MAGIC would not.

Conclusion

After the release of the 2HWC catalog, MAGIC and *Fermi*-LAT performed dedicated analyses on three new TeV sources detected by the wide FoV observatory HAWC. None of them were detected at lower energies and no hotspot was found near them. However, owing to the increased time and good quality data of most of the MAGIC and the *Fermi*-LAT observations, constraints on the extension of the sources were possible. With this aim, we performed both point-like and extended source searches. For 2HWC J2006+341 and 2HWC J1907+084*, a radius of ~ 0.16 deg is viable given limits from the extended source search by MAGIC. For 2HWC J1852+013*, MAGIC and *Fermi*-LAT results with respect to HAWC spectra suggest a much larger extension or a harder spectrum below ~ 10 TeV. Moreover, we find that none of the known pulsars in the vicinity of 2HWC J2006+341, 2HWC

J1907+084* or 2HWC J1852+013* are likely to directly power these objects. It may be that these 2HWC sources are PWN created by as yet un-detected pulsars, or have some other origin such as a Galactic supernova remnant. More sensitive observations in the near future will provide valuable information on the nature of these sources and help to disentangle features in the crowded regions.

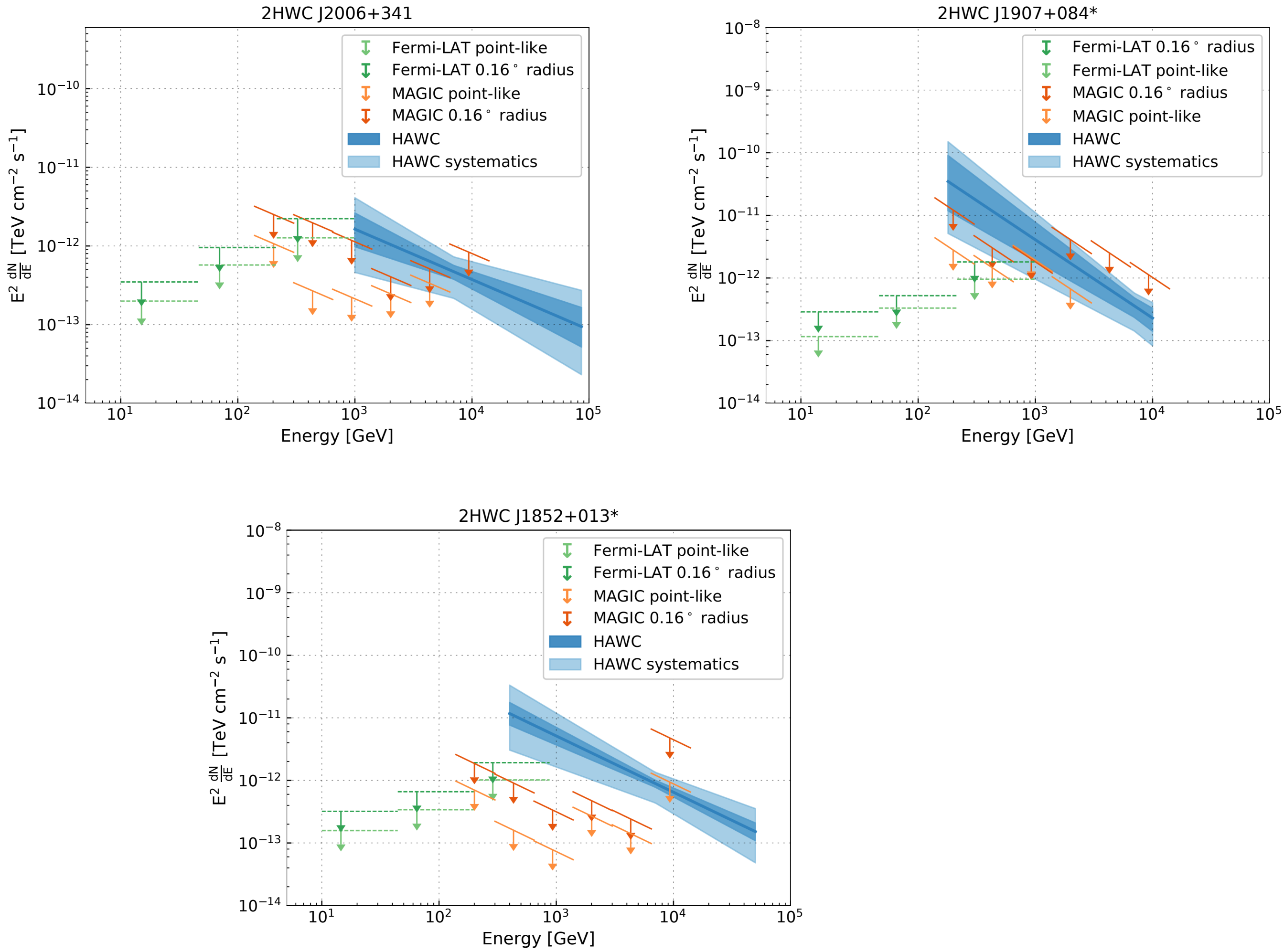

Figure 4.3: Spectral energy distribution from 10 GeV up to $\sim$ 90 TeV. In all cases, the assumed spectrum for the sources is a power-law function with photon index Γ = 2.64 for 2HWC J2006+341 (*top left*), Γ = 3.25 for 2HWC J1907+084* (*top right*) and Γ = 2.90 for 2HWC J1852+013* (*bottom*), as obtained by HAWC (see Table [4.1]). *Fermi*-LAT 95% confidence level ULs for 0.16 deg disk and point-like hypotheses are shown with dashed green and light green lines, respectively. MAGIC 95% confidence level ULs are displayed for both a point-like hypothesis (light orange) and a 0.16 deg radial extension (orange). The HAWC spectrum (dark blue) is obtained for the parameters given in Table [4.1]. The light blue band indicates the HAWC spectrum taking into account 1σ systematic errors of 0.2 and 50% in the photon index and flux, respectively.

CHAPTER 5

Development of a calibration system for future large size telescope of Cherenkov Telescope Array

In first part of this chapter, we describe the future aspects of Imaging atmospheric Cherenkov (IAC) technique with a brief description of new generation IAC telescope array, Cherenkov Telescope Array (CTA). India, as one of the members of CTA consortium, has contributed in the hardware development of a calibration system for the optical calibration of the camera of a prototype large size telescope (LST) of CTA. The second part of this chapter is mainly focused on the detailed description of the development and characterization of calibration system. In this project, I have actively participated in assembly and characterization of individual components as well as whole system.

Cherenkov Telescope Array (CTA)

The wide energy range of present day observational gamma-ray astronomy has been covered with a combination of spaced-based direct detection and ground-based indirect detection techniques. At present, IAC technique has been proven unambiguously as the most efficient detection technique and mostly responsible for the rapid evolution of gamma-ray astronomy. A deep survey of 230 hr of H.E.S.S over a small portion of galactic center detects tens of new sources [9]. Similar deep survey over full sky can explore multiple sources, but requirement of enormously long observation time with present generation IAC telescopes makes it quite impossible. Within the constraint of less duty cycle of IAC telescope (compared with other techniques), it can be partially achieved with IAC telescope of order of magnitude better sensitivity.

The extensive study of GeV-TeV sky over decade with present generation IAC telescopes (MAGIC, HESS etc.) slowly starts to saturate their sensitivity range (i.e. detection of $\sim 1\%$ of the Crab flux at 5σ significance level in 50 hr observation above 300 GeV) and further exploration requires a new generation telescope with order of magnitude better sensitivity over a energy range of about 20 GeV to some 300 TeV.

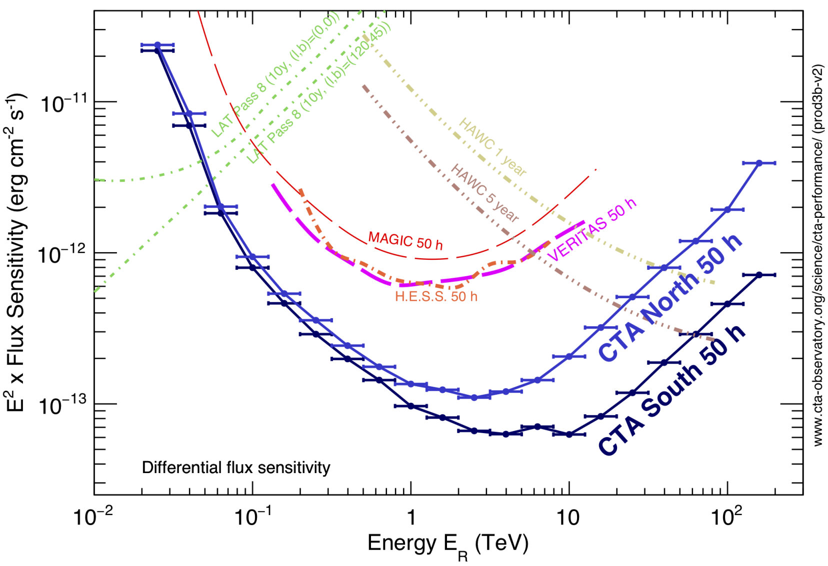

Figure 5.1: Comparison of differential energy flux sensitivity of CTA with the H.E.S.S., MAGIC, VERITUS and HAWC ones. The plot is taken from [https:www.cta-observatory.org]

The Cherenkov Telescope Array (CTA) is a large international collaborative effort aimed at the design and operation of a dedicated VHE gamma-ray observatory in the energy range 20 GeV-300 TeV, which will achieve about one order of magnitude better the sensitivity than the current major IAC arrays [5.1]. The CTA consortium plans to build two observatories, one in northern and other in southern hemisphere, to get full-sky coverage. The sites for northern and southern hemisphere array are respectively at Observatorio del Roque de los Muchachos on La Palma, Spain and at European Southern Observatory in Chile. Since most part of galactic plane can easily be observed from southern part, CTA southern observatory will mainly observe sources in the galactic plane. It will therefore be designed to have maximum sensitivity over the full energy range. The northern observatory will be focused in extra-galactic observation and will therefore cover only low and mid energy ranges from 20 GeV to 20 TeV.

In order to provide order of magnitude better sensitivity in such a wide energy range, CTA has been designed in a optimized way, balancing cost against the performance in different energy bands. The uniform array of identical telescopes with fixed separation was not the effective solution. The detailed simulation shows that use of different telescope types in different energy regime will boost the performance to desired level.

- **The low energy range ($\lesssim$ 100 GeV):** The primary photons of energy of a few tens of GeV will produce less number of Cherenkov photons spread over a large area on the ground. To detect these primary photons, the Cherenkov light needs to be sampled efficiently over the light pool. This requires closely spaced large sized telescopes ($\sim$ 23 m diameter) to collect as much as possible Cherenkov photons. Since the event rate in low energy range is comparatively high, coverage of a small portion of CTA array ($\sim 10^4$ m^2) with this type of telescopes will provide the desired sensitivity [11].

- **The middle energy range (0.1-10 TeV):** This is the core energy band of CTA which is also well studied with the operation of present generation telescopes. This mid energy range will be covered with an array of medium sized telescopes ($\sim$ 12 m diameter) with a spacing of $\sim$ 100 m. The order of magnitude improved sensitivity can be achieved both by increasing the collection area and by the higher quality shower image reconstruction. The multiple images of a single event will help to improve the event reconstruction [11].

- **The high energy range (> 10 TeV):** In the highest energy regime, the event rate is very small and therefore an array of area of several square kilometers is required to achieve sufficient improvement in sensitivity. Since the Cherenkov light content, from high energy photon, is comparatively large, it is possible to detect shower beyond the cherenkov light pool. Thus the array of small sized telescopes ($\sim$ 4 m diameter) with an inter telescopic distance of $\sim$ 150 m is sufficient to achieve desired performance [210].

Large Sized Telescope (LST)

The Large-Sized Telescope project is a collaborative effect of ten countries across the globe including India. These telescopes are mainly responsible for the low energy sensitivity of CTA between $20 - 150$ GeV. The 23 m diameter parabolic reflective surface, supported by carbon fiber structure, provides a collection area of 400 m^2. The large collection area of LST helps to push the CTA threshold energy down to few tens of GeV. The Cherenkov photons after reflection are focused into a camera, consisting of PMTs as detectors, at 28 m distance where optical signal is converted into electrical signal and then digitized & stored in DAQ system. The camera field of view is 4.5^0. The short re-positioning time of 20 s and low threshold energy of LSTs provide an unique opportunity to observe transient phenomenas (like GRBs).

For more detailed information, refer to [211, 212]

Both northern and southern hemisphere array will consists of 4 LSTs at the center of the array.

Medium Sized Telescope (MST)

The Medium-Sized Telescope array covers the most crucial part of CTA energy spectrum and provides an excellent sensitivity over the core energy range, from 100 GeV to several TeV. The MST is a modified Davies-Cotton type telescope with alt-az mount. The MST has a reflector of 12 m diameter and a focal length of 16 m. The MST cameras are also made of PMTs and posses a wide field of view of $> 7.2^0$ [211, 213].

Small Sized Telescpe (SST)

The Small-Sized Telescopes are sensitive to highest energy gamma-photons and extend CTA accessible energy range from several TeV to 300 TeV. Three different prototypes are designed for SST, one single-mirror design and two dual-mirror designs. The dual mirror structure allow excellent imaging over a wide field of view. The SSTs have a primary mirror of diameter of 4 m. The diameter of secondary mirror in dual-mirror design is ~ 2 m. The SST camera uses silicon photomultiplier (SiPM) and silicon sensors as photo detectors and posses a wide field of view of 8-10 degree. For more detailed information referred to [211, 214, 215]

CTA collaboration have planned to spread out 70 SSTs over several square kilometers in southern hemisphere array of CTA.

Development and characterization of calibration system

As a part of CTA collaboration, Indian CTA group decided to take part in hardware development of CTA. In this regard, a calibration system for a prototype LST of the northern hemisphere array has been built by India through a collaboration of Saha Institute of Nuclear Physics, Kolkata & Tata Institute of Fundamental Research, Mumbai.

Necessity of IAC camera calibration

The conventional IAC telescope camera has been designed to detect very short duration Cherenkov pulse ($3-5$ nsec) produced in EAS of high energy cosmic particles and therefore photo detector having very fast time response, like Photo Multiplier Tube (PMT), has been primarily chosen. The IAC camera is a two dimensional array of large number of PMTs and each of them is considered as the pixel of the camera. The PMT converts photons into an amplified electrical signal through a series of processes, controlled by system parameters like quantum efficiency (QE) of cathode, phe collection efficiency (PECE) of anode and secondary electron collection efficiency (SECF) of dynodes.

- **Uniformity of PMT response:** The reliable data collection requires uniformity of individual PMT response through out the camera plane, when subjected to the same input signal. In the case of the IAC camera, there are some discrepancies between the pixels due to electrical components. Though all PMTs of LST camera are commercially identical, the system parameters (QE, PECE and SECE) and emission of secondary electrons from dynodes are slightly different from pixel to pixel. Thus the output signal of one pixel is not identical with that from the others. Also the read-out electronics and the electrical to optical signal converter at the end of pixel module can be different from pixel to pixel and can be changed their behaviour with time. In this regard, a relative calibration of pixels are necessary which equalize the response of different PMTs to a same mean value by monitoring the gains of individual pixels [216].

- **Linearity of camera pixels:** During data taking process, camera pixels are differently illuminated due to the fluctuation of NSB and the presence of bright star within FoV. All these factors have a time varying component which can vary over a time scale of minutes to hours. The pixel intensity also depends on moon phase during observation. The good quality data acquisition requires a linear proportionality of pixel outputs with input intensities (photons/pixel). To evaluate the linearity of pixel response over a range of input intensities, the whole read-out chain needs to be calibrated at a regular interval during data taking using interleaved calibration.

- **Calibrate of pixel chain:** The knowledge of exact number of Cherenkov photons which have formed the image of an event, allows to reconstruct the energy of the primary photon. The IAC camera requires an absolute calibration which allows to estimate the number of initial photons from the signal of a pixel. The absolute calibration provides the conversion factor from one photon to the corresponding charge (terms of phes) stored in DAQ [216].

- **Time calibration:** The photon detection, amplification and signal transportation to trigger system requires some time ($\sim$ 100 nSec) and can slightly differ this time from pixel to pixel. The estimation of accurate arrival time information requires a precise knowledge of transportation delay time. The camera and whole read-out chain needs to be calibrated to determine the transportation delay time and its fluctuation over time.

All IAC telescopic systems require a standard light source which helps to calibrate its camera by illuminating the pixels exactly as the Cherenkov light pool of a γ-initiating EAS. This is known as the optical calibration of camera. The calibration system is typically placed at the center of mirror dish, as shown in the figure [5.2]. Here after the **calibration system** is referred to as **calbox**.

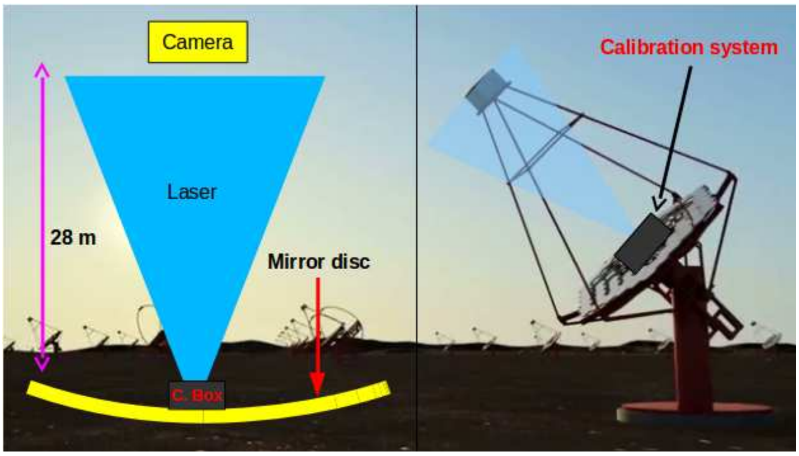

Figure 5.2: The schematic diagram reveals the basic idea of prototype LST camera calibration and sitting arrangement of calibration system

Basic features of the calibration system

- **Monochromatic pulsed light source:** The Cherenkov spectrum at observation level ($\sim$ 2 km a.s.l.) is given by equation [2.9] and $d^2N/d\chi d\lambda$ is proportional to $1/\lambda^2$. This reveals that bulk of the Cherenkov radiation is emitted in 355 nm (i.e. in bluish ultra-violet range). Moreover Cherenkov pulse is a short duration pulse with a rise time of $\sim$ 2 ns. To mimic this pulse, sharply monochromatic pulsed light source with short rise time are required for calbox.

- **Source of variable intensity:** To ensure the linearity of pixel chain, the calbox should have a output light of variable light intensity. This can be achieved by the combination of optical filters (discussed later). According to

CTA requirement, the source intensity should be high enough to illuminate the camera, at 28 m distance, upto a intensity level of 10-1000 phe per pixel.

- **Uniformity of output emission:** The pixels of LST camera are distributed over a circular region of diameter of ~ 2 m which produce a cone of aperture of $\sim 4^0$ at the center of mirror disc. To produce an uniform illumination of all these pixels, a diffuse source of uniform intensity over a wide solid angle is required.

- **Water proof housing:** The calbox should be designed to survive under extreme weather conditions (i.e. snow, rain etc). To protect inner components and electronics, calbox requires a water and air tight housing arrangement. It also requires to be light tight to prevent light leakage in operational condition.

- **Temperature control:** During data taking period, the inside temperature of calbox should have to be maintained to its equilibrium value to ensure a consistent behaviour of electronic components. The inside temperature should have to be monitored continuously for the safety of electronic gadgets.

- **Remote access:** As a part of camera, the remote access and control of different components are essential requirements of the calbox because the whole camera subsystem which will be operated remotely through ethernet connection.

- **Triggering arrangement:** The discrimination of calibration signals from both EAS-initiated events and randomly generated NSB events requires a separate triggering mechanism of calbox which should be sent to DAQ system every time it fires.

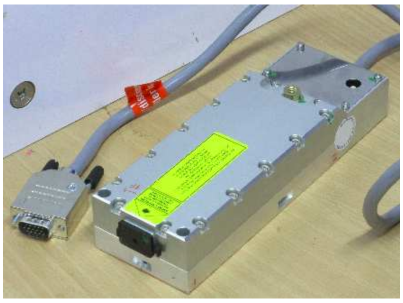

Figure 5.3: Image of LASER head module

Figure 5.4: Image of the front side of LASER controller module.

Hardware description

The description of hardware part of calbox involves detail information of a large number of both optical and electronics components. We describe below the essential components of the system:

Optical components

LASER and its controller: A passively Q-Switched Nd-YAG laser, operating at the third harmonic at 355 nm has been chosen as monochromatic light source for calbox. This is designed to provide pulsed emission of width 300 ps at frequency 355 nm. The laser repetition rate can be controlled externally by an input trigger signal, fed to laser controller. The laser can operate upto a frequency of 2 KHz. It can provide 1.2 μJ energy per pulse with a peak power of 4 KW. The operating temperature range, specified by manufacturer, are 15^0-35^0. The laser head module is connected with its controller which controls the lasing action. The controller module requires a 100-240 V, 50 Hz AC power supply. The picture of laser and its controller are shown in figure [5.3,5.4].

Optical filter and filter wheels: in order to have variable intensities, a set of 10 neutral density optical-UV filters of different attenuation power has been used to control laser pulse intensity. A pair of filter wheels, each having six filter positions, are simultaneously used to produce 36 filter combinations ranging from 0.0 to 7.0 optical density. Optical density (OD) describes the amount of energy blocked or rejected by an optical filter. Thus OD is the measure of filter attenuation and is defined as the negative logarithm of filter transmittance [217].

$$OD = -\log_{10} T = -\log_{10} \frac{I}{I_0} \tag{5.1}$$

Where I_0 and I represents the intensities of laser light before and after the filter attenuation respectively. This range of attenuation is sufficient to produce desired intensity level of 10-1000 phe per pixel at 28 m distance. The picture of filter wheels combination is shown in figure [5.5].

Figure 5.5: The combination of two filter wheels which provides a broad attenuation range.

Light diffuser: To obtain a uniform diffuse light source from the collimated laser beam, a diffuser is required which takes laser beam as input and produces a diverging light beam of uniform intensity over wide solid angle as output. Teflon is chosen as diffuser material due to its high reflectivity (> 95% above 350 nm). The basic structure of diffuser contains a spherical cavity (diameter of 11 mm) with three mutually perpendicular exit tunnels [figure:(5.6)]. One tunnel with largest diameter (5.5 mm) is used as the entrance path of laser beam which, after multiple reflections inside spherical cavity, losses its directionality and comes out as a diffuse beam. To obtain a diverging beam, exit path is designed as a cone with an angular aperture of 10^0. The whole structure is placed on a vertically moving platform to adjust its height with laser beam. The seating arrangement of diffuser is also shown in figure [5.7].

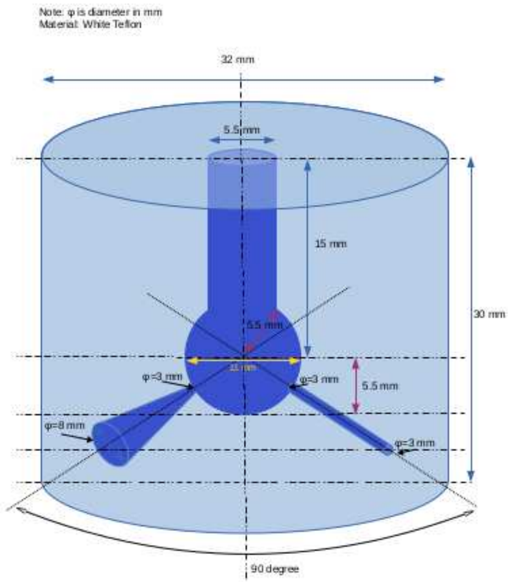

Figure 5.6: Basic structural diagram of diffuser, designed by B. B. Singh and L. Saha.

Figure 5.7: Picture of diffuser module with vertically adjustable platform.

Photo diode: For the purpose of precise alignment of diffuser with respect of collimated laser beam, a high speed HAMAMATSU photo diode (Hamamatsu S5052) has been mounted on the third exit tunnel of the diffuser. A small rotation of diffuser in horizontal plane from its aligned position would produce a drop in the photo diode signal. By comparing photo diode signal with standard value (measured in perfectly aligned condition), one can readjust the diffuser. This arrangement also provides an independent way to measure output light characteristics simultaneously with the PMT. The photo diode is shown in figure [5.8].

Light guide: To minimize light leakage in the path between diffuser and the exit window of calbox, a teflon made cylindrical structure is used to guide diffuse photons up to exit window. This also helps to reduce ambient photon density inside calbox. This is shown in figure [5.8].

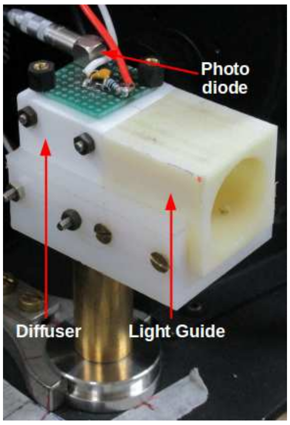

Figure 5.8: The composite system of light guide and diffuser equipped with photo diode.

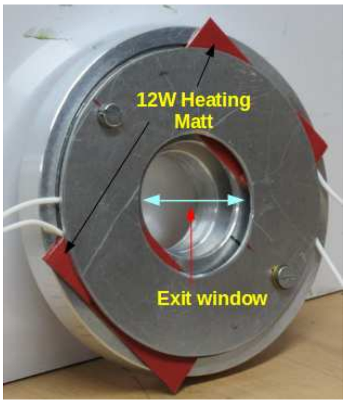

Figure 5.9: The exit window mounting arrangement with 12W window heating mats

Exit window: The exit window of calbox consists of a UV anti-reflecting coated fused silica plate and its corresponding mounting arrangement. The diameter of exit window is 30 mm. The whole arrangement should be consistent with the water proof housing requirement of calbox. The whole arrangement should be water tight to fulfill the water proof housing requirement of calbox. The exit window glass with its mounting arrangement is shown in figure [5.9].

Electronic and electrical components

Control PC: To operate different subsystems in a synchronous way and execute commands sent by the remote user, the calbox requires an in-built microcontroller within its housing arrangement. Raspberry Pi (Model B, 2nd generation), a credit card size pc with USB, ethernet port and a 40 pin GPIO connector, is chosen for this purpose. All the subsystems of calbox are directly or indirectly controlled by this control unit. It requires a power supply of 5 V DC. The Raspberry pi and its different components are shown in figure [5.10].

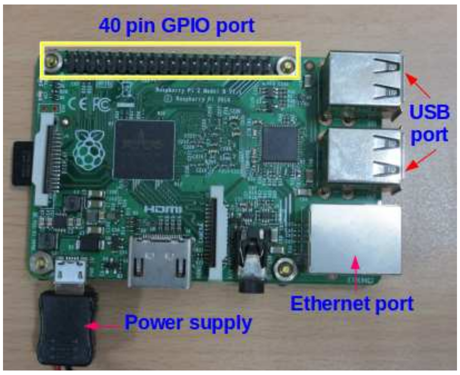

Figure 5.10: The close up view of Raspberry Pi. The labeling shows the USB, ethernet ports and GPIO connector.

Figure 5.11: The 100W heating mat which helps to maintain inner temperature of calibration system.

Temperature and Humidity sensor: A temperature sensor has been installed to monitor the inside temperature at regular intervals of time. If the inside temperature goes beyond the safety limit of laser controller, temperature sensor informs the Raspberry pi which will automatically switch off the laser controller. Temperature sensor also records the variation of temperature through out the operation time in a text file format.

Heating Matt: In winter season, the night time temperature at the site of CTA northern array goes below 0^0 centigrade. To operate in this weather condition, cal-box requires an in-built heating element which maintains inside temperature within the safety limit of the laser. One heating mat with 100W rating has been installed for this purpose. To keep the exit window free from vapour condensation, other four small heating mats, each of 12W rating, are placed inside the mounting arrangement of exit window [figure (5.9)].

AC to DC converter: The majority of the components like filter wheels, micro-controller, photo diode etc requires DC power supply. To fulfill this requirement, two AC to DC converters (TRACO power supply) with 6V, 12V and 24V DC output have been installed which convert part of input AC supply into DC supply.

Electrical to optical converter: To avoid attenuation of electrical signal (pedestal and calibration trigger) in transmission process from calbox to counting house ($\sim$ 100 m), the electrical signals are converted into optical signal and transmitted via optical cables which provide comparatively low attenuation. Two transducers has been installed to convert signal from electrical to optical and vice-versa.

Assembly of calibration system

The assembly of the calbox requires an efficient planning to place all these components inside a cuboid metal box of size 0.44 m $\times$ 0.34 m $\times$ 0.25 m. The final sitting arrangement of components is an optimized state between the compactness and the accessibility of different components without disintegrating them.

Housing system: The structure of housing system is divided in two segments, an upper side open hollow cuboid box and a rectangular plate which can fit exactly in size with the open side of cuboid box. The hollow cuboid box acts as the container of calibration system whereas the rectangular plate as the lid to close the system. The hollow cuboid structure has been build with 14 rectangular aluminium bar of 10 mm thickness and finally wrapped with 1 mm thick aluminium sheet [figure (5.12)]. The lid part also follows the same structure. The size of the cuboid structure is 0.44 m $\times$ 0.34 m $\times$ 0.25 m. In the aluminium sheet, one circular region of diameter 30 mm in the front side and one rectangular region on right side, are left open for exit window and I/O panel respectively [figure (5.13)]. To make the system water proof, the whole contact region between lid and the cuboid structure has been covered with rubber gasket arrangement. For the easy accessibility of inner components and uniform distribution of load, all components are arranged on a common base plate, made of 5 mm thick aluminium sheet. This base plate with all components is fixed at the bottom of housing system. Both the inner and outer surfaces of hollow cuboid structure, both the surfaces of lid and base plate are coated with black color to reduce reflection from metal surfaces.

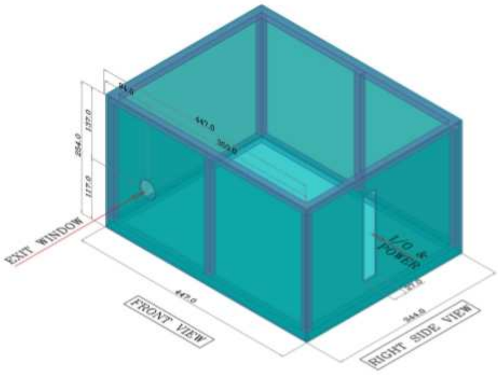

Figure 5.12: The structure diagram of housing arrangement of calibration system. Designed by B. B. Singh.

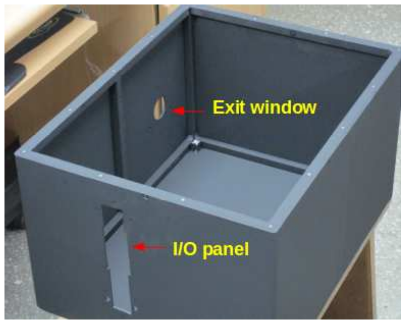

Figure 5.13: The picture of housing arrangement of calibration system.

The I/O panel contains 220V, 50Hz AC input supply port, ethernet port, two VNC ports and four optical cable connector grouped in two. The two VNC ports provide photo diode signal and laser trigger. The optical connectors are used to send triggers and receive their acknowledgement signal from DAQ.

The assembly of all the components over base plate is shown in figure [5.14]. The inside and outside view of completely assembled calibration system is shown in figure [5.15],[5.16].

Control software

Trigger system

The calibration system is equipped with two different triggering arrangements; pedestal and calibration trigger. All electronic devices including the readout chain have an intrinsic electronic noise which forms the electronic background to IAC data. To estimate the electronic and NSB background, pedestal run (in first case, HV is kept off & in other HV kept on) has been taken without a pulsed light impinging onto the camera. To inform DAQ system about pedestal run, calbox sends a trigger,

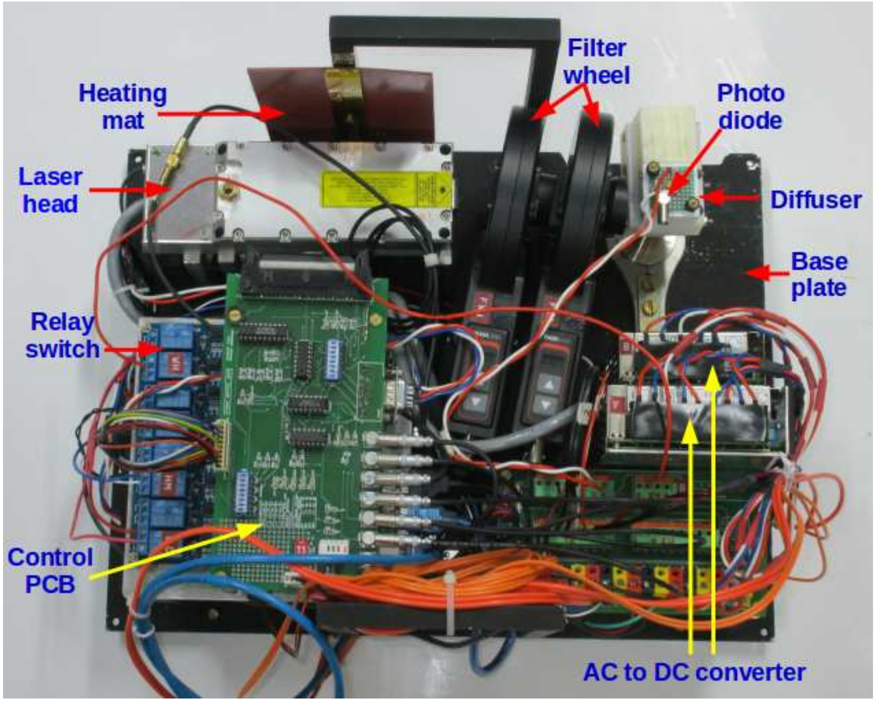

Figure 5.14: Assembly of calibration system components.

called pedestal trigger, and to ensure the receiving of pedestal trigger, DAQ system issues also a signal, called pedestal trigger acknowledgement. The Raspberry pi generates a TTL pulse which has been sent to DAQ system as pedestal trigger. It also receives the acknowledgement from DAQ.

During calibration run, calbox sends a trigger signal to DAQ system whenever it fires. This is known as calibration trigger. In-built PIN diode of laser head module generates a signal in perfect synchronization with laser firing (a fixed delay of 33 ns). The part of this PIN diode signal can be used as the calibration trigger. Similar to pedestal trigger, DAQ system sends an acknowledgement signal to calbx after receiving the calibration trigger.

Remote access

The requirement of remote access capability of calibration system has been implemented with the application of a commercially available software, known as OPC

Figure 5.15: Inside view of assembled calibration system.

Figure 5.16: Outside view of complete calibration system.

Unified Architecture (OPC UA) and developed by OPC foundation. OPC UA provides an interface for machine to machine communication protocol. The OPC UA server program has been installed in raspberry pi of calibration system and the remote user has been directed to logged in the server as a OPC UA client. For detailed information, please refer to [12] and [https://opcfoundation.org/license/gpl.html].

Characterization: Test and Results

The development of a reliable & robust calibration system requires a complete description of the optical and mechanical behaviour of the system. The characterization process mainly involves:

1. Study of temperature and humidity variation over long term operation.
2. Determination of PMT gain and photon to charge conversion factor using single photo electron (SPE) pulse analysis
3. Calibration of the optical filters
4. Study of output pulse properties i.e. measure of pulse amplitude, rise time and FWHM.

5. Study of variation of pulse properties with different filter combinations and laser repetition rate.

6. Study of pulse stability over long term operation.

7. Study of uniformity of diffuse light over wide solid angle.

8. Study of mechanical stability

The measurement of all these optical properties requires a reliable photo detector. Since the values of measured properties partly depend on the response of photo detector, a specific PMT i.e. $HAMAMATSU\ R11920-100-20$, used in LST camera, has been chosen. This is a fast response low gain PMT having 8 dynodes with built-in Cockcroft-Walton voltage multiplier circuit [figure (5.17)]. The normal operating high voltage (HV) is 1000V.

In this experiment, we have used a special seating arrangement for PMT which helps to measure the light intensities over a wide solid angle. A hollow cuboid wooden platform has been designed which contains 121 circular holes of diameter 3.5 cm. These circular holes are distributed in a uniform 2D array pattern (11×11 array) where center to center distances between two nearby holes are kept fixed along both X and Y directions [figure (5.18)]. All these circular holes are capable of holding PMT in a stable configuration and by placing PMT at different positions, one can measure intensity profile over this plane.

Experimental setup: The experiment with PMT requires some special safety precautions. Due to high sensitivity and huge gain factor, the presence of excess ambient light can affect the experimental results and simultaneously can be harmful to PMT dynodes. To minimize ambient photon density, experimental setup requires a dark room arrangement.

In LST camera system, the distance between the calbox and the camera module is 28 m. Since it is difficult to manage such a space in the laboratory, it has been decided

Figure 5.17: The HAMAMATSU R11920 − 100 − 20 PMT used as detector in characterization of calibration system

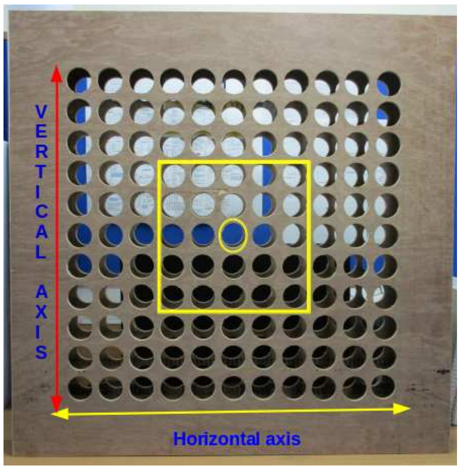

Figure 5.18: The special PMT holding arrangement. The yellow circle and rectangle represent the central PMT position and the $2^0 \times 2^0$ region respectively when calibration system is at 4 m away.

to perform all tests with a separation distance of 4 m and then extrapolate the results to 28 m distance using inverse square law method. To construct a temporary dark room, a cuboid aluminium frame structure of length 4 m and cross section 75×75 cm^2, has been designed [figure (5.19)]. The PMT holding arrangement is attached at one long end and calibration box is placed at opposite end of the cuboid structure. The center of calibration box exit window has been aligned perfectly in line with the center of central PMT position. The whole setup with PMT holding arrangement and calibration system is completely wrapped with black cloth which forms a temporary dark room.

Variation of inside temperature over time

Calibration system contains large number of electronic and electrical components. Temperature dependence of these components would effect the output optical properties of calibration system. Since it is very difficult to estimate this behaviour properly, measurement of system characteristics at stable temperature condition will be more convenient. Variations of inner temperature over time have been studied.

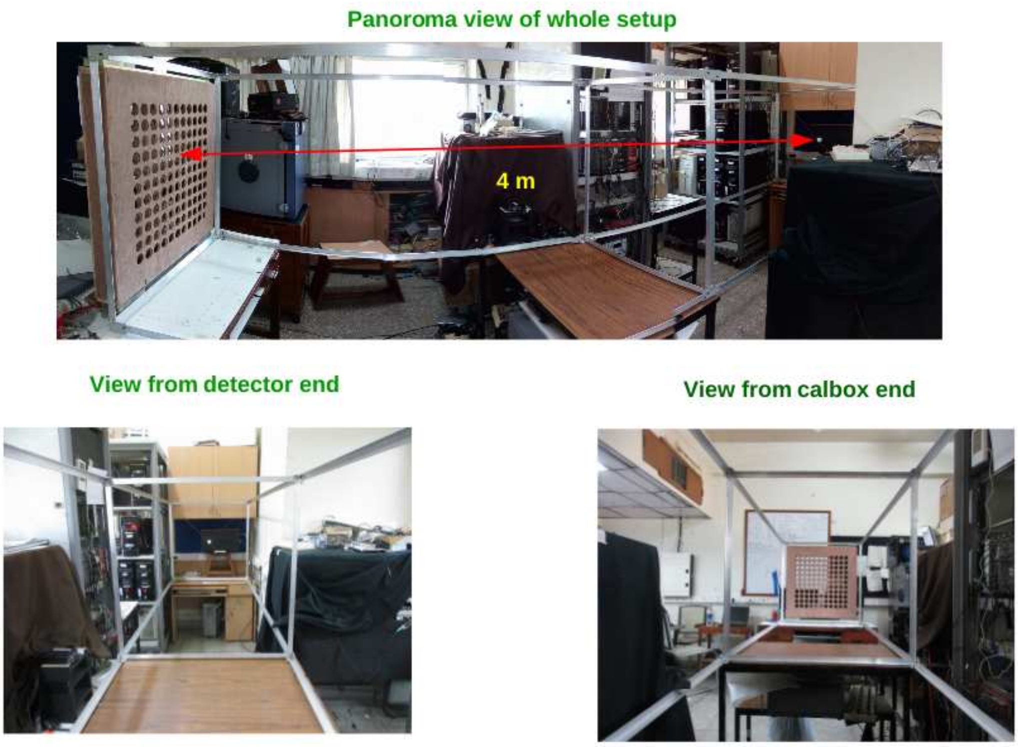

Figure 5.19: The whole experimental setup for the testing of calibration system: Upper panel: panoroma view; Lower left: as viewed from detector end; Lower right: as viewed from detector end.

Data are taken with two different environments; inside and outside the laboratory. Inside the laboratory, data has been taken with three different configurations i.e. laser off with lid open, laser off with lid close and laser on with lid close conditions. Since any small change in temperature due to laser operation will be suppressed by environmental fluctuation, outside data is taken only with off laser condition. In case of outside data, lid is kept closed. The temperature variation with lid open condition is shown in figure [5.20]. All other temperature variations are shown in figure [5.21]. The plot taken with lid open condition shows that it takes $\sim$ 1 hr to stabilize its temperature. The two plots taken inside laboratory with lid close condition shows similar behaviour i.e. firing of laser does not have any effect. It also shows that calibration system takes nearly 3.5 hrs to stabilize its inner temperature when lid is closed and maintains a difference of $\sim 8^0$C from ambient one. Thus the comparatively long thermal stabilization time of calbox system is entirely due to heat trap inside closed system. Probably the inner and outer black coating over aluminium elongates the thermal stabilization by affecting its heat emission. All the data represent hereafter are taken with stable temperature condition.

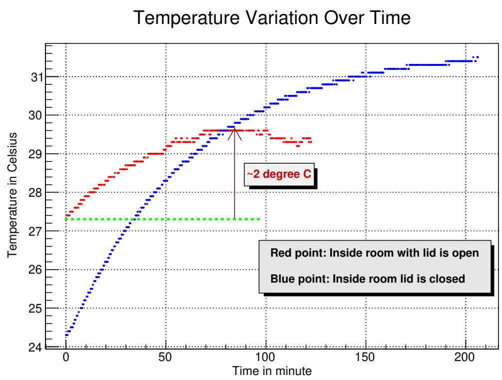

Figure 5.20: Variation of inner temperature with time. Data point color code; Red: inside laboratory with laser off and lid is open, Blue: inside laboratory with laser off and lid is closed.

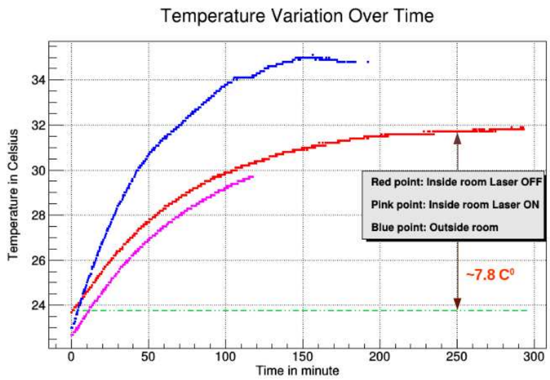

Figure 5.21: Variation of inner temperature with time. Data point color code; Red: inside laboratory with laser off, Pink: inside laboratory with laser on, Blue: outside laboratory with laser off.

Measurement of single pulse properties

Study of pulse properties involves precise measurement of pulse amplitude, rise time and FWHM. Analytical measurement of pulse properties require a functional form which describes pulse profile with sufficient accuracy. This is known as pulse profile fitting algorithm.

Single pulse fitting algorithm: In this analysis, we have used a simple but robust algorithm, known as multi Gauss fitting algorithm. In case of non symmetrical pulse profile, multi Gauss algorithm provide better fitting accuracy than any other single functional form. In this algorithm, the given pulse profile is divided in multiple small regions which are then individually fitted with separate Gauss functions. The division of pulse profile into large number of region increases the fitting accuracy in expense of mathematical complexity of handling large number of parameters and loss of physical information.

The Gauss function is defined as

$$f(x) \;=\; [\mathrm{p0}] * \exp(-0.5 * ((x - [\mathrm{p1}])/[\mathrm{p2}])^2) \tag{5.2}$$

where the free parameters p0, p1 and p2 are amplitude, mean and sigma of the distribution respectively. The amplitude and rise time has been obtained by three and two Gauss fitting algorithm.

Estimation of pulse amplitude: For the estimation of pulse amplitude, pulse profile i.e 50 ns time window is divided into three regions. The boundaries between 1st-2nd and 2nd-3rd regions are chosen symmetrically with respect to the peak pulse position to place it at the center of the middle region. The algorithm first finds the time bin (jth bin) corresponding to the peak position and then (j-10)th to (j+11)th bin region is chosen as middle region [figure (5.22)]. The fitted value of p0 of second Gauss function provides the corresponding pulse amplitude.

Estimation of pulse rise time: Pulse rise time has been estimated via two Gauss fitting algorithm i.e. 50 ns time window is divided into two regions. The whole rising part of pulse is considered in a single region. The algorithm again finds the bin (jth) corresponding to peak position and chosen (j+2)th bin as the boundary of two regions [figure (5.23)]. The fitted parameter values of first Gauss function are used to calculate the rise time of pulse. This is typically of the order of 2 ns.

Single photo-electron (SPE) spectrum analysis

Since calibration system is designed to characterize and monitor the behaviour of IAC camera, it is most convenient to express output light intensities in terms of average number of emitted photo-electrons (phe) per pixel when kept at a distance of 28 m. This requires a precise knowledge of PMT mean pulse amplitude corresponding to the event of single phe emission from the photo-cathode.

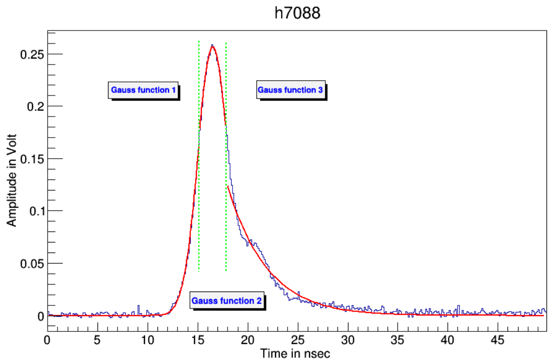

Figure 5.22: Representation of three Gauss fitting algorithm. Pulse profile is divided in three region and middle region is chosen symmetrically with peak position. The amplitude of 2nd Gauss function is used to estimate pulse amplitude. For 2nd Gauss function, typical value of χ^2/d.o.f. is 1.2.

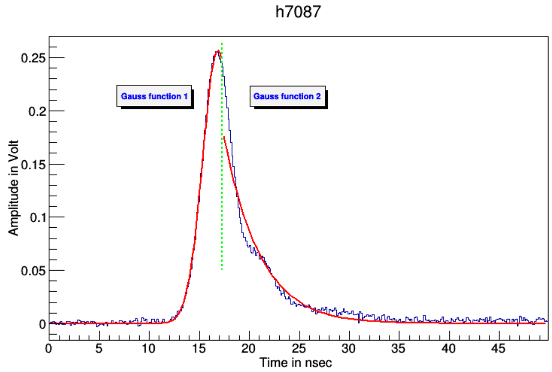

Figure 5.23: Representation of two Gauss fitting algorithm. Pulse profile is divided in two region and first region is chosen to cover complete rising part of pulse. The fitted parameters of 1st Gauss function is used to estimate pulse rise time. For first Gauss function, the typical value of χ^2/d.o.f. is 1.26.

A SPE spectrum analysis requires very weak pulsed light source which is implemented by attenuating a collimated laser beam with higher OD filter combination (OD: 6.0). Due to absence of fine tuning of filter combination in higher OD range, a pre amplifier of gain 10 is applied to data before storing in DAQ which enhance both signal and noise simultaneously. The presence of high attenuating filter lowers PMT pulse amplitude near about to the electronic noise level which requires to be measured separately. To estimate the average noise level of circuit elements and DAQ system, a set of data has been recorded without applying HV to PMT. The DAQ system stored data over a time window of 50 ns with a sampling speed of 4 GSample/sec. This is referred as a single event of the corresponding data. A distribution of average noise level of single events has been produced with a sample space of 20000 events. The Gaussian fitting of the distribution provides the average DC noise level of $\sim$ 3 mV.

The application of higher OD filter decreases PMT pulse amplitude near about to noise level. Thus distinguishing PMT pulse from the background noise is very important in SPE pulse analysis. To identify PMT pulse, a data has been recorded with lower OD filter combination (OD: 4.0). The prominent PMT pulse provides a clear estimation of narrow time window within which signal pulse can only arise (20 to 35 ns). In SPE spectrum analysis, we have analyzed data only from this region. The SPE data has been recorded with 5 different HV settings i.e. 1100V, 1150V, 1200V, 1250V and 1300V. The first part of analysis is mainly focused into fitting of the pulse profile, bounded by the predefined time window. The multi-Gauss fitting algorithm, described previously,has been used to fit the pulses of individual events [figure (5.24)].

SPE amplitude distribution: The amplitude of second Gauss function provides the peak pulse value within signal time window. A distribution of peak pulse value is plotted using a sample space of 20000 events. The distribution is characterized with typical double hump structure; one is sharp peak with higher weight factor and other is broad peak with comparatively lower weight factor [figure (5.25)]. The sharp one, called pedestal peak, represents the effect of DC noise and noise due to HV supply. The second peak with lower weight factor is the combined effect of single phe emission from photo-cathode and electronic noise. The broadening represents the fluctuation in amplification process of PMT dynodes. The second peak is fitted with single Gauss function. The actual pulse due to single phe can be obtained by subtracting pedestal value from the mean pulse amplitude of fitted Gauss function [equation:5.3]. The pedestal values are estimated by finding the amplitude corresponding to the local minima between pedestal and SPE peak [figure (5.25)].

$$\text{SPE pulse amplitude} = \frac{\text{mean pulse amplitude} - \text{pedestal}}{\text{pre amplifier gain}} \tag{5.3}$$

The plot of SPE mean pulse amplitude against different HV settings shows a linear trends and well fitted with a function of form $F(x) = 10^{(mx+c)}$ [figure (5.26)]. The SPE mean pulse amplitude of CTA PMT at nominal HV (i.e 1 KV) can be obtained by extrapolating the function $F(x)$ at $x = 1000$ and this is estimated as 0.17 mV.

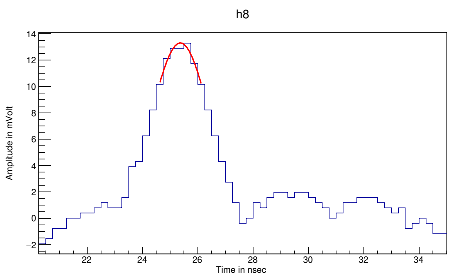

Figure 5.24: The SPE pulse profile within the pre defined time window. The peak amplitude is estimated from fitting algorithm.

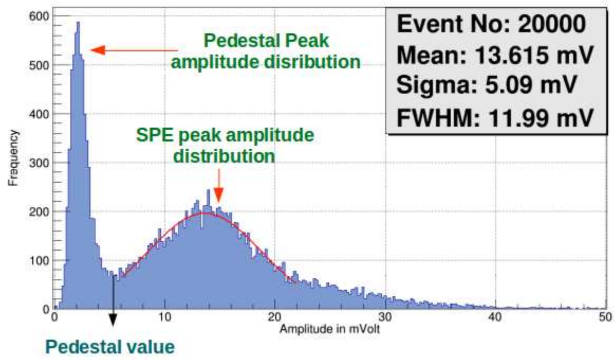

Figure 5.25: The SPE amplitude distribution for HV setting of 1.2 KV. The pedestal and SPE peak are labeled and the estimation of pedestal value is also shown which is used in equation [5.3].

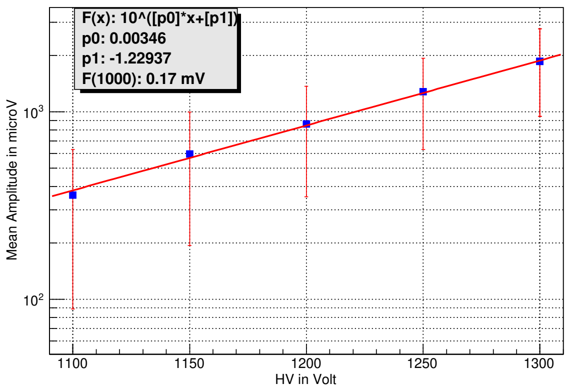

Figure 5.26: The variation of SPE pulse amplitude with HV settings. The fitted parameters values are; p0: 0.00346 and p1: -1.22937. Error bars are the sigma of SPE amplitude distribution divided by pre amplifier gain factor.

Calibration of the optical filters

The combination of two filter wheels provides a wide range of attenuation. To check the linearity of filter characteristics when two or more filters act as a combined unit, proper calibration of different filter combinations is required. It also provides the linearity of attenuation throughout the range of optical densities. To cover the whole range of optical densities, combination of different photo detectors is used. For lower OD filter combinations, pulse amplitudes are measured with photo diode

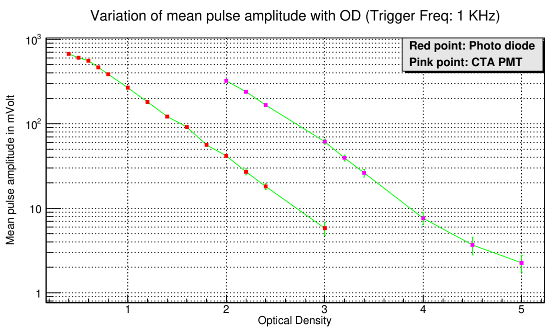

Figure 5.27: The OD vs pulse amplitude data taken with PMT and ph diode data are plotted simultaneously. The red and pink data points represent photo diode and PMT data respectively.

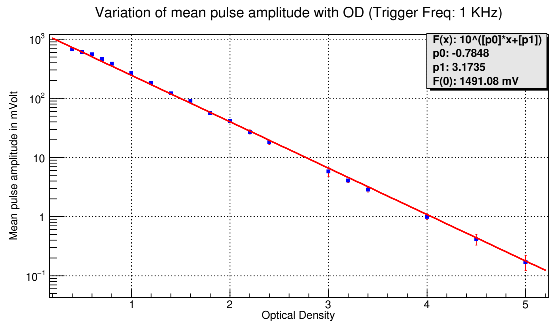

Figure 5.28: The normalized OD vs pulse amplitude data fitted with $F(x) = 10^{([p0]x+[p1])}$. The fitted free parameters values are p0: -0.7848 and p1: 3.1735. From extrapolation, the unattenuated pulse amplitude is estimated as 1491.08 mV.

and HAMAMATSU PMT is used for higher OD filter combinations. These two sets of data are shown in figure [5.27]. Since the data points are nearly parallel to each other, except in the saturation region at very low OD value ($<$ 0.5 OD), they can be merge into one set of normalized data which covers the whole range of OD. In normalization process, the average slope of these plots are used to obtain the plot shown in figure [5.28].

To estimate the unattenuated pulse amplitude (i.e. at OD: 0.0), the normalized data set is fitted with function of form $F(x) = 10^{(mx+c)}$. To calibrate the optical filters, the observed attenuation of filter combination is estimated in terms of effective OD values. The effective OD values are calculated using equation [5.1], where I_0 and I are replaced by unattenuated pulse amplitude $F(0)$ and mean amplitude from normalized data set corresponding to that OD respectively. This observed attenuation shows a deviation from expected attenuation (i.e OD) as mentioned by manufacturer. This deviation is plotted in figure [5.29].

This observed deviation is probably due to the effect of multiple reflections of photons between filter combination. At lower OD, this effect is small due to large number of transmitted photon over the reflected photons from second filter, But at higher where the number of transmitted photon is less, the effect is more prominent.

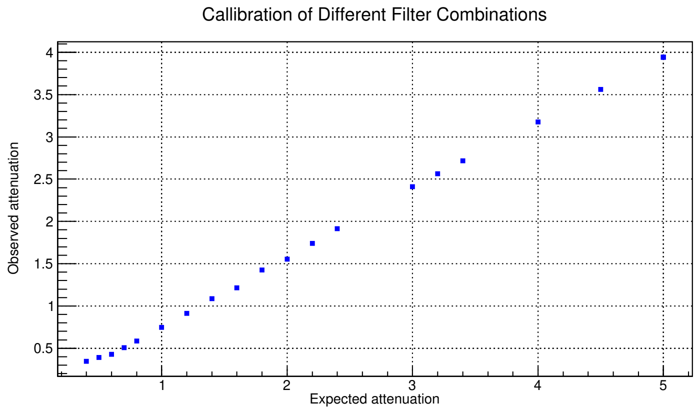

Figure 5.29: Calibration of different filter combinations

Calculation of pulse properties for single filter combination

For events recorded in identical conditions (i.e. fixed filter combination and fixed laser repetition rate), single pulse analysis shows a fluctuation of pulse properties between consecutive events. This arises from purely statistical fluctuations of different physical processes involved in the emission and detection mechanism. This fluctuation is random and oscillates around a base value. To determine the base value, a distribution of corresponding pulse property have been made with 10000 events and fitted with Gaussian function. The mean and sigma of fitted function represent the average value of corresponding quantity and its error respectively. The determination of pulse amplitude and rise time corresponding to a filter combination of 3.4 OD and trigger frequency of 1 KHz is shown in figure [5.30,5.31].

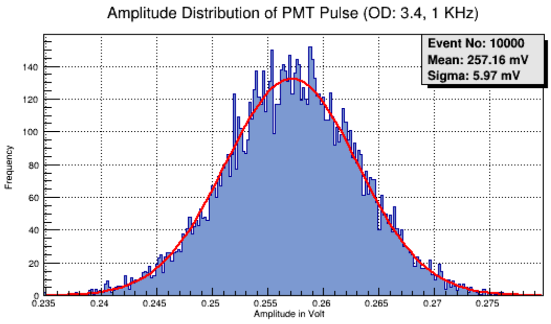

Figure 5.30: PMT pulse amplitude distribution for filter combination 3.4 OD. The mean pulse amplitude is 257.16 mV and the corresponding error is 5.97 mV. The percentage fluctuation in terms of RMS/Mean is obtained as 2.7%.

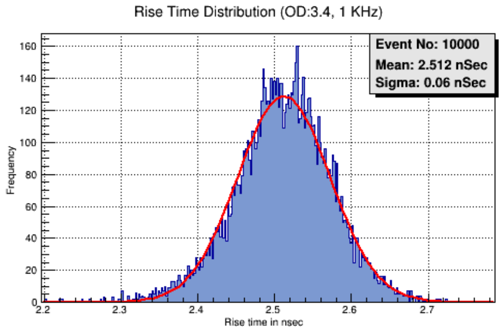

Figure 5.31: PMT pulse rise time distribution for filter combination 3.4 OD. The mean rise time is 2.5 nS and its error is 0.06 nS. The percentage fluctuation in terms of RMS/Mean is obtained as 2.9%.

Variation of pulse properties with different filter combinations and laser trigger frequency

The output pulse properties mainly depend on two quantities, attenuation power of filter combination and laser repetition rate. The characterization of the calibration system requires detailed knowledge about the dependencies and nature of variation of pulse properties with these two quantities. The effect of each quantities has been studied separately by keeping other quantity constant.

Variation of pulse amplitude: Pulse amplitudes have been measured over whole range of available optical densities, but only data taken with CTA PMT, covers the higher OD part of the spectrum, are presented here. Figure [5.32] shows the dependencies of pulse amplitude on filter attenuation as a function of laser trigger frequency. The spectrum shows a linear dependence over the attenuation range of 3.2 to 6.0 OD. This spectrum is also fitted with log scale linear function [figure: (5.43)].

The figure [5.33] shows the dependencies of pulse amplitude on laser repetition rate with filter attenuation power as the parameter. It is clearly shown that the change in laser trigger frequency have no effect on output pulse amplitude.

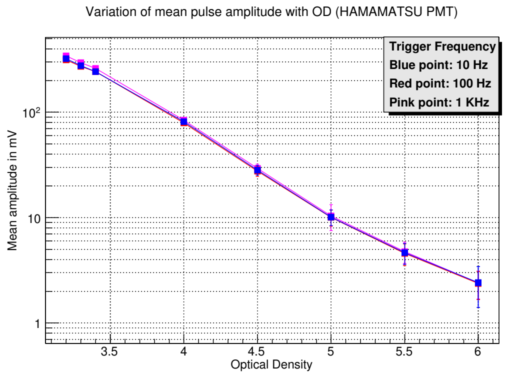

Figure 5.32: The variation of pulse amplitude with filter attenuation. The data are taken with three different laser trigger frequencies which are used as parameter. Data point color code: pink: 10 Hz, red: 100 Hz, blue: 1 KHz.

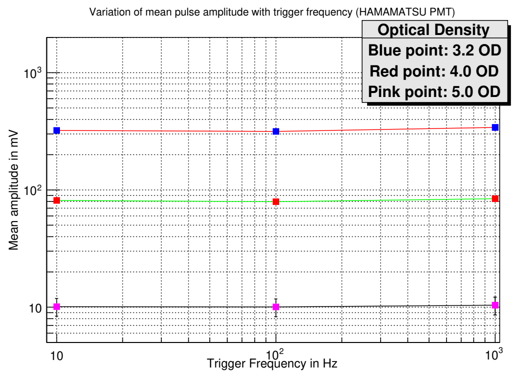

Figure 5.33: The variation of pulse amplitude with laser trigger frequency. The data are taken with three different filter combinations which are used as parameter. Data point color code: blue: 3.2 OD, red: 4.0 OD, pink: 5.0 OD.

Variation of rise time: The PMT pulse rise time has been calculated for 6 different filter configurations and 3 different trigger frequencies. In ideal situation, rise time should be independent of the variation of other factors. The figure [5.34] shows the dependencies of pulse rise time on filter attenuation as a function of laser trigger frequency. The plot shows that the rise time is stable within fluctuation over the attenuation range of 3.2 to 5.0 OD.

The figure [5.35] shows the dependencies of rise time on laser repetition rate with filter attenuation power as the parameter and shows that pulse rise time does not depends on trigger frequency.

Stability of pulse amplitude over long term operation

In order to perform continuous observations over long time period, calibration of the data requires stability of pulse amplitude of calibration system through out the observation period. In this part, we have studied the variation of the pulse amplitude over a long time ($\sim$ 2hrs) when both laser repetition rate and filter attenuation are kept constant. The pulsed output of calibration system, taken with

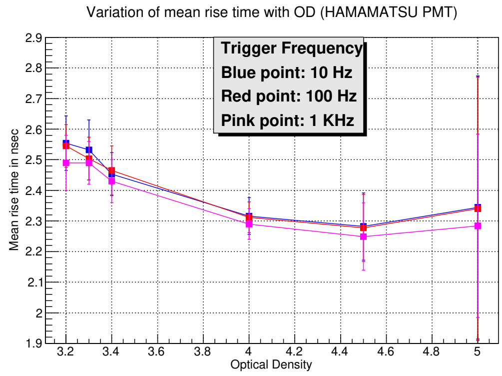

Figure 5.34: The variation of rise time with filter attenuation. The data are taken with three different laser trigger frequencies which are used as parameter. Data point color code: blue: 10 Hz, red: 100 Hz, pink: 1 KHz.

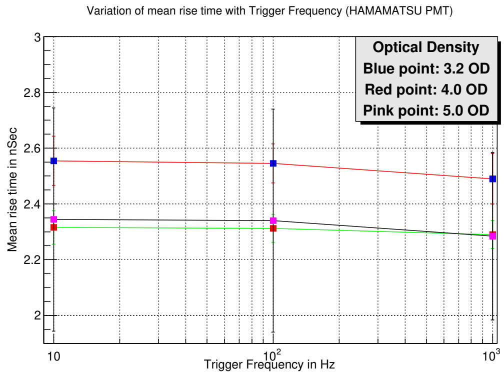

Figure 5.35: The variation of rise time with laser trigger frequency. The data are taken with three different filter combinations which are used as parameter. Data point color code: blue: 3.2 OD, red: 4.0 OD, pink: 5.0 OD.

filter combination of 3.4 OD and trigger frequency of 10 Hz, has been recorded continuously over a time period of 2 hours. Comparatively low attenuation is chosen to ensure prominent pulse with less fluctuation and to avoid handling of large sized data file, laser repetition rate is set at 10 Hz.

The amplitude of each event has been calculated by multi-Gauss fitting algorithm. For analysis purpose, the average amplitude over second has been chosen and calculated by averaging the amplitudes of 10 consecutive events. The time evolution is plotted by placing average amplitudes at their corresponding time bin, measured in seconds [figure: (5.36)]. This shows that, except at beginning part, average amplitude over second is stable within fluctuation. The decreasing trends at the initial part is probably due to the lack of thermal stabilization.

To quantify the pulse stability, certain specific requirements need to be fulfilled. For interleaved calibration, taken in the interval of 20 mins, the pulse amplitude should not change by more than 5% in 20 min. For analysis purpose, a 20 min time window, from 100 to 120 min, is chosen and produce an amplitude distribution of all 12000 events in this interval [figure: (5.37)]. After fitted with Gauss function, percentage fluctuation is obtained by multiplying the ratio of RMS and its mean with 100,

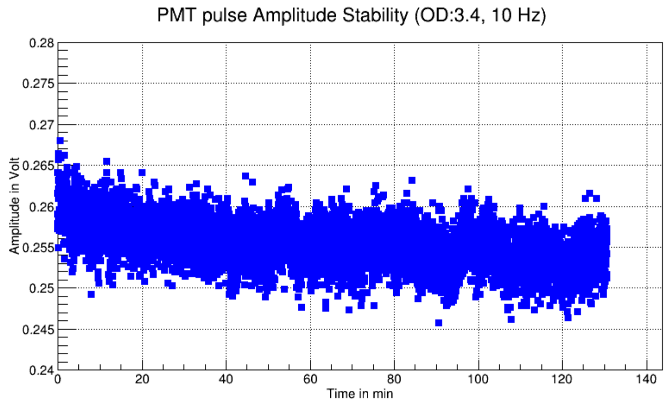

Figure 5.36: Variation of average pulse amplitude in long term operation. The data taken with filter of 3.4 OD and laser trigger frequency of 10 Hz.

which is 2.8%. Similarly for dedicated calibration run, taken at the beginning of night, pulse amplitude should not change by more than 3% in 1 min. Thus a 1 min time window, from 120 to 121 min, is chosen. Similar Gaussian fitting of amplitude distribution of 600 events provides a percentage fluctuation of 2.7% [figure: (5.38)].

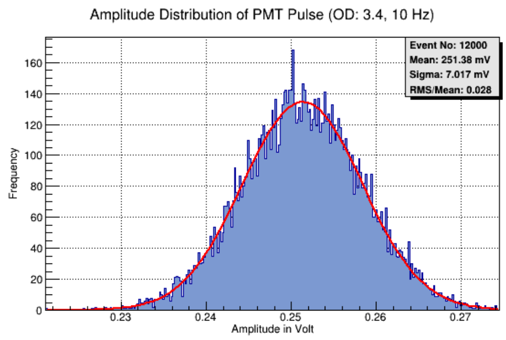

Figure 5.37: Amplitude distribution of 12K events, taken in 20 min with OD: 3.4 and laser frequency of 10 Hz. The percentage fluctuation in terms of RMS/Mean is obtained as 2.8%.

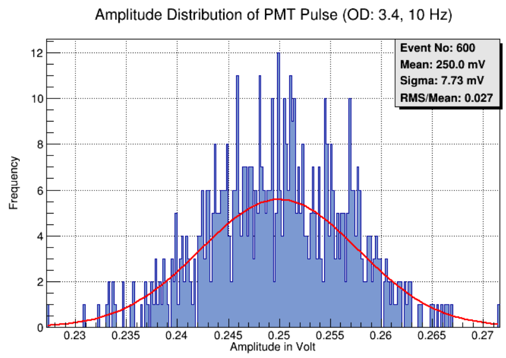

Figure 5.38: Amplitude distribution of 600 events, taken in 1 min with OD: 3.4 and laser frequency of 10 Hz. The percentage fluctuation in terms of RMS/Mean is obtained as 2.7%.

Uniformity of diffuse light

As mentioned earlier, uniformity of diffuse light over wide solid angle is one of the important requirement of calibration system. The uniformity of pulse amplitude is measured over a plane, at a distance of 4 m away, which is parallel to the exit window plane of calibration system. A special experiment setup has been designed [figure: (5.18)] to measure pulse amplitude over an area of 58×58 cm^2. This area subtends a solid angle of 0.015 sr at the center of calbox exit window which is identical to a cone of semi vertical angle of 4^0. By placing CTA PMT at every positions, pulse amplitude has been measured and produced a 2D pulse intensity profile over this plane [figure: (5.39)]. The data taken with OD: 3.4 and laser frequency of 100 Hz. The profile revels some rapid fluctuation at the edges of the plane and overall percentage fluctuation is $\sim 7\%$. The extrapolation of light properties from 4 to 28 m suggests that light from a central $2^0 \times 2^0$ region would be enough to cover the LST camera region. This region is depicted in above figure. The homogeneity of pulse amplitude has been calculated over this region and estimated as 3.5%. This belongs within the tolerance level of the CTA consortium criteria.

Mechanical stability

As a part of camera system which is a moving part of IAC telescope [figure: 5.2], calibration system suffers rotation and vibration through out the observation. The term mechanical stability refers to the stability of optical properties against the mechanical movements. To avoid the effects of mechanical vibration, all components of the calibration system are placed in stable configuration and firmly attached with a base plate. To check the mechanical stability, photo diode pulse amplitude with fix filter combination (OD: 1.0) has been measured for four different orientations of calibration system. Since photo diode is attached to diffuser, its pulse amplitude is very much sensitive particularly to diffuser orientation. The different orientations

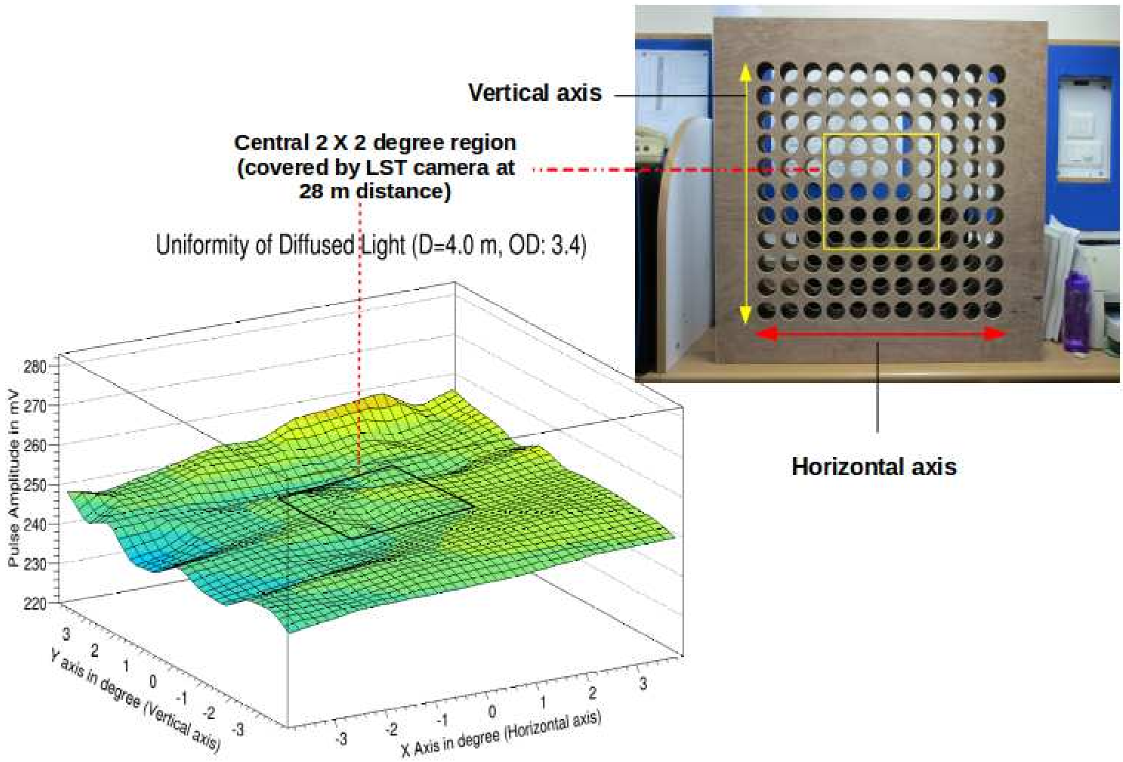

Figure 5.39: The homogeneity of pulse amplitude over a vertical plane at 4.0 m away. The central black parallelogram represents $2^0 \times 2^0$ region which corresponds to the LST camera size at 28 m away.

i.e. nominal position, exit window on bottom side and exit window on right side positions are shown in figure: [5.40]. The measured pulse amplitudes are given below:

Orientation	Mean pulse amplitude
Nominal position	304.83 ± 7.8 mV
Exit window on bottom	303.52 ± 8.1 mV
Exit window on top	302.98 ± 7.3 mV
Exit window on right	302.46 ± 9.5 mV

The close proximity of pulse amplitude reveals the stability of diffuser and other optical components against mechanical movement.

Figure 5.40: Measurement of mechanical stability of calibration system with respect to different orientations. The position of exit window and the diffuser are marked with arrow and red circle

Study of pulse amplitude in non uniform temperature

Due to temperature dependence of electronic components, all the previous data are taken after the temperature & humidity have stabilized. According to the temperature stabilization data [fig. 5.21], calibration system takes almost 3.5 hrs to reach thermal equilibrium with surroundings which is comparatively long time to stabilize the electronics before observation. To reduce this time span before observation, variation of pulse amplitude has been studied during temperature stabilization. In this experiment, recording of photo diode data has been started just after laser starts firing. The data are taken with filter of 0.5 OD and laser trigger frequency of 1KHz. The amplitude data, average of 1000 consecutive pulse, has been recorded in a fixed interval of 10 min and repeat for two ambient temperatures (18 and 29C^0). The variation of pulse amplitude with temperature are shown in figure [5.41,5.42]. Since the variation of data points belongs within its own error bar, both plots are fitted with constant functions and percentage fluctuations lies below 2%. These results are not completely conclusive because photo diode itself has a inherent temperature dependencies. But one can safely conclude that temperature dependency of mean pulse amplitude is less dominant compared to temperature dependence of photo diode.

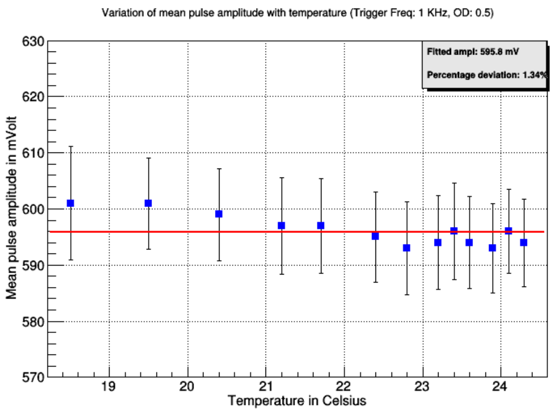

Figure 5.41: Measurement of photo diode pulse amplitude in non uniform temperature range with ambient temperature of 18C^0.

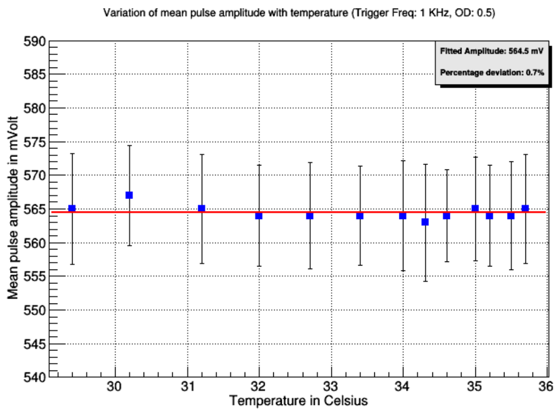

Figure 5.42: Measurement of photo diode pulse amplitude in non uniform temperature range with ambient temperature of 29C^0.

Conversion of pulse amplitude in terms of phe

According to the requirement of CTA consortium, the linearity of PMT pulse amplitude, measured at 4m distance, should be extrapolated to 28 m and expressed in terms of phe. As mentioned earlier, the inverse square law is used in extrapolation and finally divided with measured SPE amplitudeto obtain the average phe number. The fitting of OD vs PMT pulse amplitude helps to estimate phe number for optical densities beyond the PMT range (i.e. lower OD filter combinations). Only CTA PMT data are used in this extrapolation. Since PMT data only cover the higher OD range, the OD vs PMT pulse amplitude data has been fitted with function of form $F(x) = 10^{(mx+c)}$ [figure: (5.43)] and fitted parameters are used to estimate pulse amplitude at lower OD. The variation of average number of detected phes per

CTA PMT, kept at 28 m away, with different filter combinations are shown in figure [5.44].

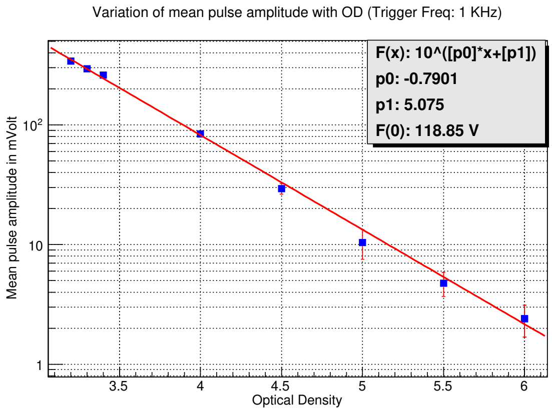

Figure 5.43: The OD vs CTA PMT pulse amplitude data fitted with $F(x) = 10^{([p0]x+[p1])}$. The fitted free parameters values are p0: -0.7901 and p1: 5.075. From extrapolation, the unattenuated pulse amplitude is estimated as 11885.0 mV.

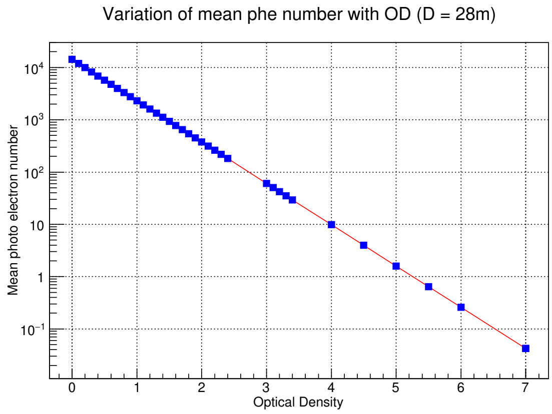

Figure 5.44: Estimation of detected phe per PMT at 28 m distance from calibration system. Lower OD values are obtained from extrapolation of higher OD data.

At present the system successfully meets all the proposed criteria of CTA collaboration. This system will shortly be installed on the prototype LST at northern hemisphere array of CTA.

CHAPTER 6

Summary and Outlook

In spite of being the one of the newest branch of astronomy, the importance of gamma-ray astronomy increases rapidly in recent few years and has been established as a potential branch of astronomy and astrophysics. This is because gamma-ray astronomy provides an effective way to study fundamental physics interactions by observing energetic events of the outer universe whose energy range lies well above the accessible range of man made accelerators. Following this trend of modern physics, the first part of this thesis is mainly devoted to study of different kind of HE and VHE gamma-ray sources of galactic origin. Since γ-rays comprise of the highest energy radiation of electromagnetic spectrum, only extreme astrophysical phenomena, both from inside and outside our galaxy, are studied in this field. This includes radiation from SNRs, pulsar wind nebula, active galactic nuclei and some unassociated sources which have no counterpart in any other wavelengths.

The goal of studying gamma-ray astronomy and basic informations regarding this has been presented in *chapter 1*.The primary motivation behind this thesis work is to explore different type of galactic gamma-ray sources and to justify them as the possible source of galactic cosmic rays. The chapter also deals with the histori-cal development of observational gamma-ray astronomy and description of possible gamma-ray production mechanisms.

In *chapter 2*, we have described different detection techniques of present day gamma-ray astronomy with the detailed description of corresponding gamma-ray observatories. The data from all these telescopes, described in this chapter, are extensively used in this thesis work. The description of MAGIC telescope includes details of MAGIC data analysis chain.

In *chapter 3*, we have analyzed GeV gamma rays from a mixed morphology middle-aged SNR 3C 391 which is reported to be interacting with dense molecular cloud. The molecular cloud interaction is confirmed by OH maser detection. The spectrum and morphology study revealed GeV emission as the consequence of hadronic gamma emission from neutral π^0 decay. This suggests, in general, that a SNR interacting with MC can be considered as the site of proton acceleration and can be considered as the possible source of galactic cosmic ray. Consideration of other factors like rate of occurring (1 in $\sim$ 30 years) and number of GeV detected SNR (occupy $\sim$ 15% of all galactic gamma ray sources) suggest that SNR, alone, can not be account for observed galactic cosmic ray spectrum. Considering other factors like rate of occurring (1 in $\sim$ 30 years) and number of GeV detected SNR (occupy $\sim$ 15% of all galactic gamma ray sources), it can be shown that SNR, alone, can not be account for observed galactic cosmic ray spectrum. This opens the possibility of presence of other source types in galactic regime.

The *chapter 4* is focused on the observations and characterization of some unassociated galactic sources. The HAWC observatory, build to detect highest energy gamma photons, published a TeV source catalog of 39 sources, out of these 19 sources have no association with known HE or VHE sources. To explore the characteristics of these dark sources over broad energy range, a multi-telescope collaborative campaign between Fermi-LAT, MAGIC and HAWC had been initiated. In spite of rigorous effort, sources still remain undetected in GeV and tens of GeV regime. We have tried to find out any possible correlation with nearby Fermi-LAT pulsar using leptonic emission model. This non detection can be explained with larger source extension. In future, observations with more sensitive instruments can provide valuable information about the nature of these sources.

In *chapter 3* and *chapter 4*, GeV-TeV data from both SNR and pulsar wind nebulae has been analyzed. It clear from the discussions that SNRs with pulsar wind nebulae can form potential particle acceleration center in galactic regime. In explaining the high energy photon emission, both hadronic and leptonic scenarios has been discussed. Due to high energetics, proton acceleration is possible in SNRs whereas in case of PWNe only leptonic model is applicable.

The sensitivity of present IACT system can be improved in future by deploying more telescopes of different shapes & sizes to cover a very wide energy range. In this context, the last part of this thesis is mainly focused into the description of a future IAC telescope. In chapter 5 ,we have described the basics of the Cherenkov Telescope Array (CTA) and development of calibration system for prototype Large Size Telescope of CTA.

Bibliography

[1] W. B. Atwood, et al. (Fermi-LAT collaboration), *Astrophys. J.* **697**, 1071 (2009).

[2] W. B. Atwood, et al., *Astrophys. J.* **697**, 1071 (2009).

[3] J. Aleksic, et al. (for MAGIC collaboration), *Astropart. Phys.* **72**, 61 (2016).

[4] J. Aleksic, et al. (for MAGIC collaboration), *Astropart. Phys.* **72**, 76 (2016).

[5] J. Aleksic, et al., *Astroparticle Physics* **72**, 76 (2016).

[6] A. Tepe, et al. (HAWC Collaboration), *Jour. Phys.: Conf. Ser.* **375**, 5 (2012).

[7] A. U. Abeysekara, et al. (HAWC Collaboration), *Astropart. Phys.* **50**, 26 (2013).

[8] A. J. Smith, (for Milagro Collaboration), 29*th Int. Cosmic Ray Conf.* **10**, 227 (2005).

[9] F. Aharonian, et al. (H.E.S.S. Collaboration), *Astrophys. J.* **636**, 777 (2006).

[10] H. Abdalla, et al. (HESS Collaboration), *Astron. Astrophys.* **612**, 61 (2018).

[11] B. S. Acharya, et al., *Astropart. Phys.* **43**, 3 (2013).

[12] S. Leitner, W. Mahnke, *ABB Corporate Research Center* (2006).

[13] D. J. Thompson, *C. R. Physique* **16**, 600 (2015).

[14] D. Paneque, *Thesis submitted for the degree of Doctor of Philosophy to the Max-Planck Institute for Physics* (2004).

[15] J. A. Barrio, et al., *MPI-PhE* **98**, 05 (1998).

[16] D. J. Fegan, *J. Phys. G: Nucl. Part. Phys.* **23**, 1013 (1997).

[17] R. Ong, *Physics Reports* **305**, 93 (1998).

[18] J. Aleksic, *Thesis submitted for the degree of Doctor of Philosophy to the University Autonoma de Barcelona* **72**, 61 (2013).

[19] A. M. Hillas, *Space Science Reviews* **75**, 17 (1996).

[20] J. Heinrich, K. Bernlohr, *Exp. Astron.* **25**, 173 (2009).

[21] R. L. Coto, *Thesis submitted for the degree of Doctor of Philosophy to the Universitat Autonoma de Barcelona* (2015).

[22] A. F. Barral, *Thesis submitted for the degree of Doctor of Philosophy to the University Autonoma de Barcelona* (2017).

[23] V. Joshi, *Thesis submitted to Ruperto-Carola University of Heidelberg, Germany* (2019).

[24] Hampel-Arias, *Thesis submitted to The University of Wisconsin-Madison* (2017).

[25] S. Westerhoff, (for HAWC collaboration), *Adv. in Space Research* **53**, 1492 (2014).

[26] D. A. Frail, et al., *AJ* **111**, 1651 (1996).

[27] N. E. Kassim, *Astrophys. J. Suppl. Ser.* **71**, 799 (1989).

[28] A. U. Abeysekara, et al. (HAWC Collaboration), *Astrophys. J.* **843**, 39 (2017).

[29] V. F. Hess, *Z. Phys.* **13**, 1084 (1912).

[30] W. Bothe, et al., *Zeitschrift fur Physik* **56**, 751 (1929).

[31] P. Morrison, *Il Nuovo Cimento* **7**, 858 (1958).

[32] G. Cocconi, *Proc. 2nd Int. Cosmic ray Conf. (Moscow)* **2**, 309 (1959).

[33] W. Galbraith, J. V. Jelly, *Nature* **171**, 349 (1953).

[34] P. M. S. Blackett, *The Physical Society (London)* p. 34 (1948).

[35] W. L. Kraushaar, G. W. Clark, *Phys. Rev. Lett.* **8**, 106 (1962).

[36] K. Pinkau, *Exp. Astron.* **25**, 157 (2009).

[37] W. L. Kraushaar, G. W. Clark, G. P. Garmire, et al., *Astrophys. J.* **177**, 341 (1972).

[38] D. A. Kniffen, C. E. Fichtel, *Astrophys. J.* **250**, 389 (1981).

[39] K. Pinkau, *Astron. Astrophys. Suppl. Ser.* **120**, 43 (1996).

[40] Mayer-Hasselwander, et al., *Astron. Astrophys.* **105**, 164 (1982).

[41] D. J. Thompson, et al., *Astrophysical Journal Supplement Series* **86**, 629 (1993).

[42] G. Kanbach, D. J. Bertsch, A. Favale, et al., *Space Sci. Rev.* **49**, 69 (1988).

[43] V. Schonfelder, H. Aarts, K. Bennett, et al., *Ap. J. Suppl. Ser.* **86**, 657 (1993).

[44] G. J. Fishman, D. H. Perkins, *NASA Conf. Publ.* **3137**, 26 (1992).

[45] R. Carli, et al., *Astrophysical Letters and Communications* **39**, 317 (2000).

[46] B. J. Teegarden, et al., *Astrophys. J.* **621**, 296 (2005).

[47] G. G. Fazio, et al., *Canadian Jour. of Phys.* **46**, S451 (1968).

[48] G. G. Fazio, et al., *Astrophys. J.* **175**, L117 (1972).

[49] T. C. Weekes, et al. (Whipple Collaboration), *Aerosp. Power J.* **342**, 379 (1989).

[50] F. Aharonian, A. G. Akhperjanian, et al., *Proc. 22nd Int. Cosmic ray Conf. (Dublin)* **2**, 615 (1991).

[51] R. Mirzoyan, et al., *New Astronomy Reviews* **42**, 547 (1998).

[52] W. Benbow, et al. (H.E.S.S. collaboration), *High Energy Gamma-Ray Astronomy, AIP proc.* **745**, 611 (2005).

[53] T. C. Weekes, et al., *Astropart. Phys.* **17**, 221 (2003).

[54] M. S. Longair, *High Energy Astrophysics* (Cambridge University Press, 1992).

[55] F. Aharonian, *Very high energy cosmic gamma radiation: a crucial window on the extreme Universe* (World Scientific, 2004).

[56] J. D. Jackson, *Classical Electrodynamics* (John Wiley & Sons, New York (3rd edition), 2003).

[57] E. Fermi, *Phys. Rev.* **75**, 1169 (1949).

[58] L. O. Drury, F. A. Aharonian, H. J. Voelk, *Astron. Astrophys.* **287**, 959 (1994).

[59] L. O. Drury, *Space Sci. Rev.* **36**, 57 (1983).

[60] D. Meyer, D. Horns, H. S. Zechlin, *Astron. Astrophys.* **523**, 2 (2010).

[61] A. A. Abdo, et al. (Fermi-LAT Collaboration), *Science* **331**, 739 (2011).

[62] M. Tavani, et al., *Science* **331**, 736 (2011).

[63] R. Buehler, et al., *The Astrophysical Journal* **749**, 26 (2012).

[64] F. Aharonian, A. M. Atoyan, T. Kifune, *MNRAS* **291**, 162 (1997).

[65] C. F. Kennel, F. V. Coroniti, *Astrophys. J.* **283**, 694 (1984).

[66] B. M. Gaensler, P. O. Salne, *Annu. Rev. Astro. Astrophys.* **44**, 17 (2006).

[67] A. M. Atoyan, F. Aharonian, *MNRAS* **291**, 162 (1997).

[68] A. Archer, et al. (for VERITUS collaboration), *Astrophys.J.* **821**, 129 (2016).

[69] T. M. Tauris, E. P. J. Heuvel, *Formation and Evolution of Compact Steller X-ray Sources*, vol. 39 (Cambridge Astrophysics Series, 2006).

[70] J. Albert, et al., *Science* **312**, 1771 (2006).

[71] J. A. Hinton, et al., *Astrophys. J. Lett.* **690**, 101 (2009).

[72] A. Abramowski, et al. (H.E.S.S. collaboration), *Astron. Astrophys.* **541**, 9 (2012).

[73] F. Aharonian, et al., *Astron. Astrophys.* **442**, 1 (2005).

[74] J. Marti, et al., *Astron. Astrophys.* **338**, 71 (1998).

[75] F. Aharonian, et al., *Astron. Astrophys.* **425**, 13 (2004).

[76] J. Albert, et al., *Astrophys. J.* **638**, 101 (2004).

[77] H. Falcke, F. Melia, E. Agol, *Astrophys. J. Lett.* **528**, L13 (2000).

[78] W. Goss, L. B. Robert, K. Y. Lo, *Astron. Nachr.* **324**, 1 (2003).

[79] F. Aharonian, et al., *Nature* **440**, 1018 (2006).

[80] D. Mazin, M. Raue, *Astron. Astrophys.* **471**, 439 (2007).

[81] J. Albert, et al., *Nucl. Instr. Meth. Phys. Res. A* **588**, 424 (2008).

[82] G. A. Shields, *Publications of the Astronomical Society of the Pacific* **111**, 661 (1999).

[83] C. Urry, P. Padovani, *Publications of the Astronomical Society of the Pacific* **107**, 803 (1995).

[84] D. Lynden-Bell, *Nature* **223**, 690 (1969).

[85] D. Kazanas, et al., *Astronomical Review* **7**, 92 (2012).

[86] F. Nicastro, *Astrophys. J.* **530**, 101 (2000).

[87] H. Olsen, *Phys. Rev.* **131**, 406 (1963).

[88] G. R. Lynch, O. I. Dahl, *Nucl. Instrum. Methods B* **58**, 6 (1991).

[89] W. B. Atwood, et al., *Nucl. Instrum. Methods A* **342**, 302 (1994).

[90] C. Meegan, et al., *The Astrophysical Journal* **702**, 791 (2009).

[91] W. B. Atwood, et al., *Astropart. Phys.* **28**, 422 (2007).

[92] A. A. Moiseev, et al., *Astropart. Phys.* **27**, 339 (2007).

[93] W. N. Johnson, et al., *IEEE Trans. Nucl. Sci.* **48**, 1182 (2001).

[94] O. Ferreira, et al., *Nucl. Instr. Meth. Phys. Res. A* **530**, 323 (2004).

[95] F. Acero, et al. (Fermi-LAT collaboration), *Astrophys. J. Suppl. Series* **218**, 23 (2015).

[96] P. A. Cherenkov, *Phys. Rev.* **52**, 378 (1937).

[97] I. E. Tavani, I. M. Frank, *Dokl. Akad. Nauk. SSSR* (1937).

[98] C. Hofmann, et al., *Reviews of Modern Physics* **71**, 897 (1999).

[99] J. V. Jelly, *PERGAMON PRESS, London* (1958).

[100] H. Anderhub, et al., *Journal of Instrumentation* **8**, 197 (2013).

[101] A. M. Hillas, *Proc. 19th Int. Cosmic ray Conf. (La Jolla)* **3**, 445 (1985).

[102] T. C. Weekes, K. E. Turver, *Proc. 12th ESLAB symp.* **SP124**, 279 (1997).

[103] B. Wiebel, *Technical report, Universitat Wuppertal* **WUB 94**, 08 (1994).

[104] P. Sreekumar, et al., *Astrophys. J.* **494**, 523 (1998).

[105] S. Hunter, et al., *Astrophys. J.* **481**, 205 (1997).

[106] K. Mase, et al., *Proceedings of 28th Int. Consmic Ray Conf.* (2003), vol. 5.

[107] S. Funk, et al., *Astropart. Phys.* **22**, 285 (2004).

[108] J. Cortina, *MAGIC internal note, Max-Planck-Institute for Physics* (2001).

[109] J. Aleksic, et al., *Astroparticle Physics* **72**, 61 (2016).

[110] T. Bretz, et al., *Astroparticle Physics* **31**, 92 (2009).

[111] D. Nakajima, et al., *Proceedings of the ICRC 2013* **id 787** (2013).

[112] R. Paoletti, et al., *IEEE Transactions on Nuclear Science* **54**, 404 (2007).

[113] J. Sitarek, et al., *Nucl. Instr. Meth. Phys. Res. A* **723**, 109 (2013).

[114] V. P. Fomin, et al., *Astroparticle Physics* **2**, 137 (1994).

[115] R. Zanin, et al., *Proc. of 33st Int. Cosmic Ray Conf., Rio de Janerio, Brazil* (2013).

[116] P. Majumdar, et al., *Int. Cosmic Ray Conf.* **5**, 203 (2005).

[117] R. Mirzoyan, *Int. Cosmic Ray Conf.* **7**, 265 (1997).

[118] E. Aliu, et al., *Astroparticle Physics* **30**, 293 (2009).

[119] S. Lombardi, *International Cosmic Ray Conference* **3**, 266 (2011).

[120] F. Aharonian, et al., *Astroparticle Physics* **6**, 343 (1997).

[121] W. Hofmann, et al., *Astroparticle Physics* **12**, 135 (1999).

[122] C. Gini, *Economic Journal* **31**, 22 (1921).

[123] R. W. Lessard, et al., *Astroparticle Physics* **15**, 1 (2001).

[124] T. P. Li, et al., *Astrophys. J.* **272**, 317 (1983).

[125] W. A. Rolke, et al., *Nucl. Instr. Meth. Phys. Res. A* **551**, 493 (2005).

[126] T. Ergin, et al., *Astrophys. J.* **790**, 65 (2014).

[127] J. Rho, R. Petre, *Astrophys. J. Lett.* **503**, L167 (1998).

[128] A. A. Abdo, et al., *Astrophys. J.* **712**, 459 (2010).

[129] A. A. Abdo, et al., *Astrophys. J.* **718**, 348 (2010).

[130] A. A. Abdo, et al., *Astrophys. J. Lett.* **706**, L1 (2009).

[131] A. A. Abdo, et al., *Science* **327**, 1103 (2010).

[132] A. A. Abdo, et al., *Astrophys. J.* **722**, 1303 (2010).

[133] D. Castro, P. Slane, *Astrophys. J.* **717**, 372 (2010).

[134] M. Ackermann, et al., *Science* **339**, 807 (2013).

[135] R. D. Blandford, J. P. Ostriker, *Astrophys. J. Lett.* **221**, L29 (1978).

[136] T. Shimizu, et al., *PASJ* **64**, 24 (2012).

[137] Y. Chen, P. O. Slane, *Astrophys. J.* **563**, 202 (2001).

[138] M. Kawasaki, et al., *Astrophys. J.* **631**, 935 (2005).

[139] M. Kawasaki, et al., *Astrophys. J.* **572**, 897 (2002).

[140] H. Yamaguchi, et al., *Astrophys. J. Lett.* **705**, L6 (2009).

[141] H. Uchida, et al., *PASJ* **64**, 141 (2012).

[142] D. Cox, et al., *Astrophys. J.* **524**, 179 (1999).

[143] R. L. Shelton, *Astrophys. J.* **524**, 192 (1999).

[144] S. Orlando, et al., *Astrophys. J.* **678**, 274 (2008).

[145] H. Itoh, K. Masai, *MNRAS* **236**, 885 (1989).

[146] T. J. Moriya, *Astrophys. J. Lett.* **750**, L13 (2012).

[147] Y. Su, Y. Chen, *chJAA* **5**, 412 (2005).

[148] V. Radhakrishnan, et al., *Astrophys. J. Suppl. Ser.* **24**, 49 (1972).

[149] S. P. Reynolds, D. A. Moffett, *AJ* **105**, 2226 (1993).

[150] D. J. Wilner, et al., *AJ* **115**, 247 (1998).

[151] Z. R. Wang, F. D. Seward, *Astrophys. J.* **279**, 705 (1984).

[152] J. Rho, R. Petre, *Astrophys. J.* **467**, 698 (1996).

[153] Y. Chen, et al., *Astrophys. J.* **616**, 885 (2004).

[154] W. T. Reach, J. Rho, *Astrophys. J.* **511**, 836 (1999).

[155] W. T. Reach, J. Rho, *Astron. Astrophys.* **315**, L277 (1996).

[156] J. Hewitt, et al., *Astrophys. J.* **683**, 189 (2008).

[157] P. L. Nolan, et al., *Astrophys. J. Suppl. Ser.* **199**, 31 (2012).

[158] A. Bocho, *Proc. in Int. Cosmic ray Conf.* **7**, 110 (2011).

[159] M. Kerr, *arXiv:1101.6072* (2011).

[160] J. Lande, et al., *Astrophys. J.* **756**, 5 (2012).

[161] A. A. Abdo, et al., *Astrophys. J. Suppl. Ser.* **183**, 46 (2009).

[162] D. Castro, et al., *Astrophys. J.* **774**, 36 (2013).

[163] A. A. Abdo, et al., *Astrophys. J. Suppl. Ser.* **187**, 460 (2010).

[164] T. M. Dame, et al., *Astrophys. J.* **322**, 706 (1987).

[165] T. M. Dame, et al., *Astrophys. J.* **547**, 792 (2001).

[166] S. R. Kelner, et al., *PhRvD* **74**, 034018 (2006).

[167] G. R. Blumenthal, R. J. Gould, *RvMP* **42**, 237 (1970).

[168] T. A. Porter, et al., *Astrophys. J.* **682**, 400 (2008).

[169] K. Mitsuda, et al., *PASJ* **59**, 1 (2007).

[170] K. Koyama, et al., *PASJ* **59**, 23 (2007).

[171] P. J. Serlemitsos, et al., *PASJ* **59**, 9 (2007).

[172] K. A. Arnaud, *ASP conf. ser. 101* p. 17 (1996).

[173] Y. Ishisaki, et al., *PASJ* **59**, 113 (2007).

[174] K. Koyama, et al., *PASJ* **38**, 121 (1986).

[175] N. Tawa, et al., *PASJ* **60**, S11 (2008).

[176] P. Morrison, McCammon, *Astrophys. J.* **270**, 119 (1983).

[177] K. J. Borkowski, et al., *Astrophys. J.* **548**, 820 (2001).

[178] E. Anders, et al. **53**, 197 (1989).

[179] H. Yamaguchi, et al., *Astrophys. J.* **749**, 137 (2012).

[180] M. Yasumi, et al., *arXiv:1403.6898* (2014).

[181] M. Ozawa, et al., *Astrophys. J. Lett.* **706**, L71 (2009).

[182] R. D. Blandford, L. L. Cowie, *Astrophys. J.* **260**, 625 (1982).

[183] Y. Uchiyama, et al., *Astrophys. J. Lett.* **723**, L122 (2010).

[184] S. Gabici, et al., *MNRAS* **396**, 1629 (2009).

[185] Y. Ohira, *MNRAS* **410**, 1577 (2011).

[186] L. A. Lopez, et al., *Astrophys. J.* **777**, 145 (2013).

[187] M. L. Ahnen, et al. (MAGIC collaboration), *MNRAS* **485**, 356 (2019).

[188] A. U. Abeysekara, et al. (HAWC Collaboration), *Astrophys. J.* **817**, 3 (2016).

[189] A. U. Abeysekara, et al. (HAWC Collaboration), *Astrophys. J.* **843**, 40 (2017).

[190] P. W. Younk, et al. (HAWC Collaboration), *Proc. 34th Int. Cosmic ray Conf.* **34**, 948 (2015).

[191] L. A. Lopez, et al., *International Cosmic Ray Conference* **301**, 732 (2017).

[192] A. U. Abeysekara, et al., *Astrophys. J.* **866**, 24 (2018).

[193] W. B. Atwood, et al., *Preprint(arXiv:1303.3514)* (2013).

[194] M. Ajello, et al. (Fermi-LAT collaboration) .

[195] M. Ackermann, et al., *Astrophys. J.* **843**, 139 (2017).

[196] M. Wood, et al. (Fermi-LAT collaboration) .

[197] M. L. Ahnen, et al. (MAGIC collaboration), *Astropart. Phys.* **94**, 29 (2017).

[198] C. J. Clark, *Astrophys. J.* **834**, 106 (2017).

[199] M. collaboration, et al., *Astron. Astrophys.* **571**, A96 (2014).

[200] P. M. S. Parkinson, et al., *Astrophys. J.* **820**, 8 (2016).

[201] H. collaboration et al., *Astron. Astrophys.* **612**, A1 (2018).

[202] R. N. Manchester, et al., *AJ* **129**, 1993 (2005).

[203] H. collaboration et al., *Astron. Astrophys.* **612**, A2 (2018).

[204] G. Hobbs, et al., *MNRAS* **360**, 974 (2005).

[205] T. Linden, et al., *Phys. Rev. D* **96**, 103016 (2017).

[206] A. A. Abdo, et al., *Astrophys. J.* **700**, L127 (2009).

[207] A. U. Abeysekara, et al. (HAWC Collaboration), *Science* **358**, 911 (2017).

[208] J. M. Yao, et al., *Astrophys. J.* **835**, 29 (2017).

[209] V. Zabalza, *Proc. of 34st Int. Cosmic Ray Conf., Hague Netherlands* p. 922 (2015).

[210] T. C. Consortium, *Exp. Astron.* **32**, 193 (2011).

[211] K. Bernlohr, et al. (CTA collaboration), *Astropart. Phys.* **43**, 171 (2013).

[212] G. Ambrosi, et al., *Proc. 33rd Int. Cosmic ray Conf. (Rio De Janeiro)* **2**, 776 (2013).

[213] M. Garczarczyk, *Proceeding of Science* p. 959 (2015).

[214] J. L. Dournaux, *Proceeding of Science* p. 945 (2015).

[215] J. Niemiec, J. Michalowski, *Proceeding of Science* p. 962 (2015).

[216] M. Doro, M. Mariotti, M. Martinez, M. Gaug, *The Commissioning and Characterization of the Calibration System of the MAGIC Telescope* (2004).

[217] P. Prabhat, T. Erdogan, *Semrock Inc. A Unit of IDEX Corporation* .